**The Dissertation Committee for Hyeong Jun Kim Certifies that this is the approved version of the following dissertation:**

# Thermal Effects on Modular Maglev Steel Guideways

Committee:

Karl H. Frank, Supervisor

Joseph A. Yura

Michael D. Engelhardt

John L. Tassoulas

Eric B. Becker

# Thermal Effects on Modular Maglev Steel Guideways

**by**

**Hyeong Jun Kim, B.S.; M.S.**

**Dissertation**
Presented to the Faculty of the Graduate School of
the University of Texas at Austin
in Partial Fulfillment
of the Requirements
for the Degree of

**Doctor of Philosophy**

**The University of Texas at Austin**
**August 2007**

To My Parents

# Acknowledgements

The dissertation was prepared under the guidance of Dr. Frank. The author would like to thank Dr. Frank for his advice and support on this research. If it were not for his encouragement and patience, this research would not have been possible.

The author would like to express gratitude to Dr. Yura and Dr. Engelhardt for their expertise on steel structures, which gave the author inspiration on the study of steel structures. The author would like to express appreciation to Dr. Tassoulas and Dr. Becker for answers and suggestions to numerous questions the author had on numerical methods.

The author would like to acknowledge contributions from Travis Richards and Megan Warpinski on this research, and express appreciation for comments from David Hirschfeld, Wendall Hirschfeld, and Harry Jolly from Hirschfeld Steel Company, John Quincy and Mark Reno from Quincy Engineering, Billy Lannom from Lannom and Associates, and other AMG Guideway Team members at the Guideway Specifications Seminar on August 2004, which was a part of the U.S.M.C. Guideway Development Program.

# Thermal Effects on Modular Maglev Steel Guideways

Publication No. __________

Hyeong Jun Kim, Ph.D.
The University of Texas at Austin, 2007

Supervisor: Karl H. Frank

Current research on thermal effects on guideways has addressed many aspects of the behavior of guideways using two-dimensional models. The two-dimensional models are acceptable for existing guideway designs, in which cross sectional shapes are uniform along the length of the guideway. However, three-dimensional models are necessary for a modular design, in which the track structures that interact with Maglev vehicles are made separately and are assembled into the support structure, and in which the cross sectional shapes are not uniform. A three-dimensional numerical model of the thermal environment, in which the effect of partial shading is taken into account, is implemented for the study of guideway behavior under various thermal environments. The numerical model of the thermal environment is calibrated to the experimental results under the thermal environment at Austin, Texas, and is extrapolated to predict the behaviors of guideways under the thermal environment in Las Vegas, Nevada, which is one of the candidate sites for the implementation and deployment of the high speed Maglev transportation system. This study addresses the suitability of a modular steel guideway design under such a thermal environment. Characteristics of the behavior of guideways under various thermal environments are identified, and the behavior of guideways under the effect of partial shading is summarized.

# Table of Contents

# List of Figures

# CHAPTER 1
# INTRODUCTION

## 1.1 Research Background

Since the development of steam locomotives by British engineers, many efforts have been made to improve speed and safety of wheel-on-rail systems, leading to diesel-electric and electric propulsion systems [4]. Currently, conventional low-speed wheel-on-rail systems and relatively new high-speed wheel-on-rail systems such as TGV and ICE are competing against as well as complementing other transportation systems employing automobiles and airplanes. Recently, a new technology called Maglev utilizing magnetic forces for propulsion has been developed for public transportation. A high-speed system, shown in Figure 1.01, has been developed by a German company called Transrapid and is in place for revenue service in China. This high-speed Maglev system has been considered as competitive with the short-distance air travel market, and is believed to be able to deliver the benefits of energy efficiency, low noise levels, and a cleaner environment [1, 5]. Low-speed Maglev systems are also competing against light rail systems.

The United States has been planning to adopt this technology and is also developing a system utilizing forces generated by permanent magnets [7]. The deployment of this Maglev technology for public transportation has been considered for a few corridors in the United States, including a corridor between Las Vegas, Nevada and Anaheim, California [1]. However, the system has not yet been constructed due to the high initial investment of capital. It is generally thought that the initial construction cost of the Maglev system is higher than wheel-on-rail systems due to the high cost of the Maglev guideways and equipment. However, the frictional wear due to the contact between wheel and rail does not occur in the Maglev system, and the loads transferred from the vehicle to the guideway are less concentrated, which reduces the maintenance cost for the Maglev system and lowers the operating cost relative to wheel-on-rail systems. Regarding the cost of guideway construction, it is estimated to be more than 60 percent of initial capital investment [2, 3]. Therefore, successful commercial implementation of the Maglev technology depends greatly on the effectiveness and the cost of guideway systems, and the savings on the total cost lies in the proper consideration of guideway designs.

Figure 1.01 Maglev System by Transrapid (Courtesy of Transrapid)

### 1.1.1 Maglev Systems

Since the first concepts about transportation using magnetically levitated vehicles appeared, two major methods of magnetic suspension systems have been proposed; one using the attractive forces between the magnets, and the other using their repulsive forces along with superconductivity.

The first of these systems is the Electro-Magnetic Suspension (EMS) system, which utilizes attractive forces between the magnet and the armature. Since 1970, this system has been developed and adopted in Germany. The system uses steel-core electromagnets and stationary slotted armatures called stator packs. For the vehicle to move, the system requires propulsion, levitation, and guidance forces. The propulsion is provided by the interaction between the electromagnets that are attached to the vehicle and the stator packs that are installed with three phase windings on both sides of the T-shaped guideway. The levitation is provided by the attractive forces of the electromagnets which lift the vehicle. The guidance electromagnets and guidance rail provide control in the lateral direction. The magnetic system uses this feedback to maintain a constant air gap between the vehicle and the guideway [5]. Gap sensors and the control units control the attractive forces between the electromagnets on the vehicle and the stator packs on the guideway to maintain contact-free operation [5, 6]. The typical gap between the magnets and the corresponding stator packs is about 10 to 20 mm [2]. This small gap tolerance limit results in stringent deflection requirements for the guideway design to ensure proper operation and ride qualities of the Maglev vehicles at high speed.

The second kind is the Electro-Dynamic Suspension (EDS) system, which is based on both the magnets' repulsive forces and superconductivity, and it utilizes inductive repulsion forces for magnetic levitation. The Japanese high-speed system uses superconducting electromagnets and stationary three phase windings that are distributed along the U-shaped guideway [5]. This provides a traveling magnetic field for propulsion. Short-circuited levitation and guidance coils are also attached to the guideway. The repulsive forces between moving superconducting magnets and the short-circuited coils provide levitation and guidance. The inductive repulsion force depends on vehicle speed and provides stable levitation [2]. Since the repulsive forces do not require the active control for levitation, the system provides larger gap tolerance than the EMS system, which means that less accuracy is required in the guideway designs and fabrication [1, 5]. In addition, since the levitation is stable, the tolerance for vertical irregularity in the guideway is also higher than in the EMS systems [2].

### 1.1.2 Guideways for Transrapid EMS System

A Transrapid Type I steel guideway is shown in Figure 1.02 [39]. The guideway is 2800 mm wide and 2000 mm deep. The length of a span is about 31 m. A two-span continuous guideway is generally preferred because it deflects less under live and thermal loads when compared to single-span guideways. The Type I guideways are elevated from the ground by 2.2 m to 20 m. As shown in Figure 1.02, the cross sectional shape of a trapezoidal box is utilized because of its high lateral and torsional stiffness. The support is wider than the bottom flanges to provide lateral and torsional capacity.

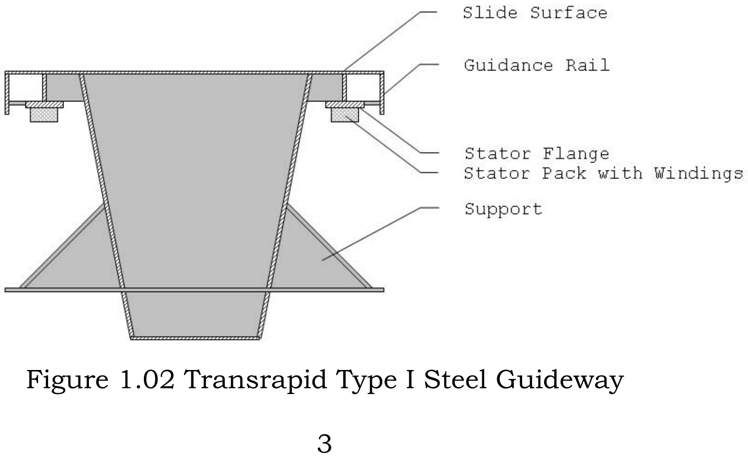

Figure 1.02 Transrapid Type I Steel Guideway

The guideway houses the stator packs with the three phase cable windings, the guidance rails, and the sliding surface for the vehicle skids. Loads on the stator packs due to the interaction with the vehicle are transmitted to the guideway through the fastening points in each stator pack [6]. The functional surfaces of the Type I guideway, which interact with Maglev vehicles, are noted in Figure 1.02. The stator packs with windings, which are attached to the stator flanges, provide propulsion and levitation forces to the vehicle. The guidance rails interact with the guidance magnets installed on the vehicle to provide lateral guidance. Guidance rails and stator flanges are all welded to the guideway, and work as built-in structures of the guideway, resisting the loads transferred from the vehicle. Slide surface is used when the vehicle loses the levitation power and slides on the guideway using the friction on the slide surface for braking. The performance of the guideway has been verified and is currently in use in the test facility in Emsland, Germany along with other guideway types.

The support conditions for two-span guideways that are adopted by Transrapid are shown in Figure 1.03 [38]. It is designed to accommodate the thermal expansions of the guideway. Under uniform expansion of the guideway due to thermal loads, the guideway would not experience any thermal stresses. However, the support conditions do not eliminate the lateral and vertical deflections due to thermal gradients in the guideway, caused by the thermal environment and heat transferred from the stator packs during the operation of Maglev vehicles. There have been various efforts to minimize these thermal deflections, including utilizing high reflective paints on the slide surface of the guideway, which reduces the heat flux on the surface, or adopting temperature compensating shapes within the guideway design [27].

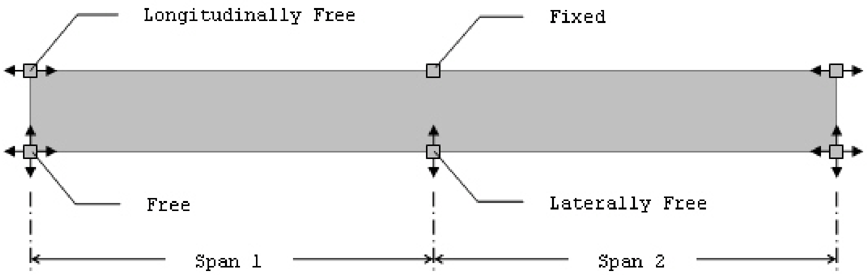

Figure 1.03 Support Conditions for Two-Span Continuous Guideways

### 1.1.3 Bridge Designs and Guideway Designs

There are many similarities between highway bridge designs and guideway designs; however, guideway designs for high-speed applications are more complex than the design of highway bridge structures. While bridge designs are generally governed by strength requirements, guideway designs in high-speed transportation are more influenced by serviceability requirements. These result from the need to control the dynamic behavior of Maglev vehicles during their operation. They are directly related to passengers' comfort during high-speed travel, and they affect the interaction between guideways and vehicles. For low-speed transportation, any irregularities on functional surfaces have minor effects on the design of the guideways. However, these surfaces are one of the major factors in the design of guideways for high-speed transportation. To control the oscillation of the vehicle during operation, it is necessary to minimize the distortion of the guideway and the associated functional surfaces with which Maglev vehicles interact.

Besides the deflections due to loads transferred from the vehicle, the deflections due to temperature changes are a major cause of distortions with the guideways. Samavedam and Purple [25] stated that problems associated with thermal stresses and deflections for the design of the German EMS system and the Japanese EDS system are difficult to resolve because there are no guidelines or design criteria. Even though the specifications for guideway designs are now available, and the Transrapid design specifications [40] provide design criteria, these criteria are not detailed enough to guarantee the performance of guideways within various thermal environments. There are limitations in applying the criteria in the specifications to the design of guideways because of the assumptions embedded within them. For example, the thermal deflection criteria for two-span guideways with equal span lengths in the Transrapid design specifications are $-L/8000$ for upward displacement, $+L/6500$ for downward displacement, and $\pm L/6960$ for lateral displacement, and L equals the length of a span. For two-span guideways with a span length of 31 m, the deflection limits are 3.9 mm, 4.8 mm, and 4.4 mm respectively. The temperature values specified for the calculation of the thermal displacements apply only if cross sections and surfaces are comparable to the existing guideways, and the values are based on the thermal environment of central Europe [40]. If the guideway shape deviates from the conventional shapes of guideways, the assumption of the specifications' validity is unwarranted, and experimental or numerical studies are necessary [40], preferably both.

## 1.2 Research Objective and Scope

### 1.2.1 Objective

The objective of this research is to extend existing research findings on the thermal response of highway bridges onto the thermal response of Maglev guideways to predict temperature distribution in the guideways under various thermal environments that produce expansions and distortions of the guideways, and reducing such thermal effects on the behavior of guideways.

### 1.2.2 Scope and Limitations

This research focuses on the behavior of the guideways for EMS systems under a specific thermal environment. However, since the numerical model could be applied to any civil structures under a variety of thermal environments if meteorological data were available, the methodology and some of the findings regarding such structures can be applied to the guideways for EDS systems as well.

This study compares the suitability of the Transrapid Type I steel guideway design, that has been verified in Emsland, Germany, with a modular design, which is tentatively named a Type IV guideway design. This design prototype is a preliminary design, and as such does not have a fully optimized design and has not undergone a detailed design check. It is intended for performance comparisons to verify if the Type IV guideway design could mitigate thermal problems.

Consideration is limited to the use of weathering steels. Even though the Type I guideway design uses reflective surface coatings on the guideways, the surface properties of weathering steels are used for both Type I and Type IV guideway studies since such steels are regarded as more economical. If weathering steels would prove not to provide appropriate thermal performance, then reflective paint could be applied on surfaces. In addition, the material properties of weathering steels would be close to the condition prevailing once the highly reflective paint on the surface gets degraded and no longer performs as initially intended [26].

## 1.3 Organization

Chapter 1 serves as an introduction to the motivation of this research. The basic knowledge on the Maglev transportation and the roles of guideways are provided to enhance understanding of the reasons for these efforts and the outcomes of the research. Chapter 2 provides the literature reviews on the thermal response of highway bridges and other structures. The issues to be resolved regarding the implementation of guideways for Maglev transportation are also addressed. Chapter 3 summarizes the thermal experimentation conducted in Austin, Texas, and provides the results. These results are used for the calibration of the numerical model presented in the following chapter. Chapter 4 explains the methods for the numerical studies, and presents the numerical model used for the research. The calibration results are also summarized. Chapter 5 lists the results of the studies discussing the behavior of guideways in the single track configuration, and compares the behavior of an existing Type I design with that of a modular design in the perspective of thermal expansions and distortions. Chapter 6 presents the results of the studies on the guideways in the double track configuration. This chapter discusses the effects of shading due to parallel guideways and the effects of partial shading due to nearby structures. Chapter 7 summarizes the research findings and provides conclusions.

# CHAPTER 2
# LITERATURE REVIEW

Guideways are under constant interaction with the surrounding environment, and the thermal environment continuously changes. The source of the changes would be solar radiation, radiation from the earth and other structures, and the heating or cooling effects of surrounding air and wind. Inside the structure of guideways, heat is redistributed flowing from a hot region to a cold one. Guideways undergo deformation because of temperature changes caused by the thermal environment. The increase or decrease of the temperature is related to the expansion of guideways while the gradient of the temperature distribution in the cross section is related to the lateral and vertical displacements. There have been many efforts to estimate and predict the temperature distributions and the deformations of guideways in thermal environments.

## 2.1 Thermal Environment

The solution to the heat transfer equation shown in Equation 2.1 for a given boundary condition is relatively well-established. However, since the solution depends on boundary conditions, accurate estimates of the boundary conditions are required. While the material properties can be found through experimentation in a laboratory, good estimates of the boundary conditions are difficult to obtain for a structure in a natural environment. Therefore, it is necessary to assess the sources of the heat flux and to quantify accurately the surface heat flux that will govern the temperature distribution inside the structure.

$$\rho c \frac{\partial T}{\partial t} = k \nabla \cdot \nabla T \tag{2.1}$$

where $T$ : temperature (K),
$t$ : time (s),
$\rho$ : density (kg/m$^3$),
$c$ : specific heat (J/kg·K), and
$k$ : conductivity (W/m·K).

There are many sources of energy influencing the heat flux on the boundaries of a structure within a natural environment. One of the sources is the shortwave radiation from the sun. Another source is the longwave radiation delivered from the surface of the earth and the surroundings, and the longwave radiation emitted by the structure itself to other surroundings. The convection heat exchange with surrounding air is another source of heat to the structure. The boundary condition shown in Equation 2.2 summarizes the effect of these sources, and each of the sources would be explained in the following sections.

$$q = -k\frac{\partial T}{\partial n} = q_{Solar} + q_{Sur} - q_{Emit} - q_{Wind} \tag{2.2}$$

where $q$ : surface heat flux (W/m$^2$),

$n$ : surface normal,

$q_{Solar}$ : heat flux due to solar radiation (W/m$^2$),

$q_{Sur}$ : heat flux from surroundings in the form of longwave radiation (W/m$^2$),

$q_{Emit}$ : heat flux to surroundings in the form of longwave radiation (W/m$^2$), and

$q_{Wind}$ : heat flux due to convection (W/m$^2$).

### 2.1.1 Heat Flux due to Solar Radiation

The flux due to the solar radiation, generally in the unit of W/m$^2$, is due to the amount of radiation from the sun reaching the surface of the earth. The estimation of the solar radiation outside the atmosphere is around 1400 W/m$^2$ [31]. The radiation from the sun interacts with the atmosphere, and some of the radiation gets reflected, some absorbed, and some scattered. The amount of energy that reaches the surface of the earth depends on the condition of the atmosphere. The daily and seasonal variation of the amount of radiation on earth has been measured or collected by agencies such as the National Climatic Data Center. The energy transfer from the sun onto the surface of the earth is classified into two categories: direct solar radiation and diffuse solar radiation [35]. For a horizontal flat surface, the amount of solar energy is estimated to be

$$G_{Solar} = G_{DNR}\cos\theta + G_{DHR} \tag{2.3}$$

where $G_{Solar}$ : solar radiation on a surface (W/m$^2$),

$G_{DNR}$ : direct normal radiation component of solar radiation (W/m$^2$),

$G_{DHR}$ : diffuse horizontal radiation component of solar radiation (W/m$^2$), and

$\theta$ : angle between the surface normal and the solar ray.

The amount of the energy from direct radiation that is absorbed by a surface is dependent on the angle of incidence [31, 35]. The first term on the right side of

Equation 2.3, $G_{DNR}\cos\theta$, represents the amount of energy on a surface due to the direct radiation considering the angle of incidence. The scattered part of the radiation that gets onto the surface of the earth constitutes the diffuse solar radiation. As a result, the diffuse solar radiation is considered to arrive in all directions from the sky from the perspective of a structure on earth. Therefore, the diffuse horizontal radiation, which is the diffuse radiation on a horizontal surface, is directed from a 180° solid angle of the sky.

When the solar radiation hits the surface of a structure, some is absorbed and the rest is reflected. The amount of energy absorbed on the surface depends on the surface properties of the material [35]. The absorptivity represents the ratio of the energy absorbed in the surface to the energy delivered onto the surface. Therefore, the surface heat flux due to solar radiation is

$$q_{Solar} = \alpha_{Solar} G_{Solar} \tag{2.4}$$

where $q_{Solar}$ : heat flux due to solar radiation (W/m$^2$),

$G_{Solar}$ : solar radiation on a surface (W/m$^2$), and

$\alpha_{Solar}$ : solar absorptivity of a surface.

When there is more than one surface, the energy reflected by one surface can be absorbed by other surfaces or can be reflected back by other surfaces again to be absorbed by the original surface.

### 2.1.2 Heat Flux due to Emission

The amount of heat flux on each surface of an element in the form of longwave radiation is estimated by the following equation:

$$q_i = -\varepsilon_i \sigma T_i^{\,4} + \alpha_i \left( \sum_{j \neq i} \varepsilon_j \sigma T_j^{\,4} F_{ji} + L_{sky} \right) \tag{2.5}$$

where $q_i$ : heat flux on a surface i (W/m$^2$),

$\varepsilon_i$ : emissivity of a surface i,

$\alpha_i$ : absorptivity of a surface i,

$\sigma$ : Stefan-Boltzmann constant,

$T_i$ : temperature of a surface i (K),

$F_{ji}$ : view factor of a surface j to a surface i, and

$L_{Sky}$ : longwave radiation from atmosphere (W/m$^2$).

The term, $-\varepsilon_i \sigma T_i^4$, represents the outgoing energy from a surface i, and the term, $\varepsilon_j \sigma T_j^4 F_{ji}$, represents the energy transfer from other surface j to a surface i in the form of longwave radiation. Even though quantification of $\varepsilon_j \sigma T_j^4 F_{ji}$ is possible, the quantification of $L_{Sky}$, which is an estimate of longwave radiation, such as radiation emitted by water vapor in the atmosphere [35], is difficult. Therefore, approximation of Equation 2.6 is used instead.

$$\alpha_i L_{sky} \approx \varepsilon_i \sigma T_{Sky}^4 \tag{2.6}$$

where $T_{Sky}$ is the effective sky temperature (K).

Heat transfer between surfaces in the form of longwave radiation is often either disregarded or approximated by using a higher value of the effective sky temperature. Therefore, the amount of the energy transfer between a surface and surroundings in the form of longwave radiation [35] is estimated by the following:

$$-q_{Emit} + q_{Sur} = -\varepsilon\sigma\left(T^4 - T_{Sky}^4\right) \tag{2.7}$$

where $q_{Emit}$ : longwave radiation heat flux to surroundings (W/m$^2$),

$q_{Sur}$ : longwave radiation heat flux from surroundings (W/m$^2$),

$\varepsilon$ : emissivity of a surface, and

$T$ : temperature of a surface (K).

The first term, $\varepsilon\sigma T^4$, represents the amount of energy emitted by the surface with a temperature, $T$. The second term, $\varepsilon\sigma T_{Sky}^4$, is an estimate of the energy that is emitted by surroundings onto the surface and absorbed by the surface.

Using $\varepsilon\sigma T_{Sky}^4$ as an estimate of heat flux due to longwave radiation originating from environments to a surface has been used by many other researchers [11, 15, 20]. For the values of the effective sky temperature, the same temperature as the air temperature has been used by some researchers. On the other hand, different values of the effective sky temperature have been used by others. In References 11 and 15, the effective sky temperature was set to the air temperature during the day, and was set to –45°C during the night. In Reference 21, even though the sky temperature was not explicitly specified, sky temperature of –10°C appears to match the specified outgoing longwave radiation during the night in the simulation when the emissivity of 0.4 and the air temperature of around 30°C are considered.

### 2.1.3 Heat Flux due to Convection

Cooling and heating effects due to the flow of air is called convection. When the surface temperature is higher than the air temperature, the surface gets cooled by the air. The surface heat flux due to convection is estimated by

$$-q_{Wind} = -h(T - T_{Air}) \tag{2.8}$$

where $q_{Wind}$ : heat flux due to convection (W/m$^2$),

$h$ : convection coefficient (W/m$^2\cdot$K), and

$T_{Air}$ : air temperature (K).

In Equation 2.9, the convection coefficient contains the terms for both free and forced convection parts. Free convection is the term used to represent the heat exchange due to the buoyancy-driven air flow, and forced convection is due to the wind.

$$h = h_0 + h_1 \cdot \upsilon_{Wind} \tag{2.9}$$

where $h_0$ : free convection coefficient

$h_1$ : forced convection coefficient, and

$\upsilon_{Wind}$ : wind speed (m/s).

For example, the convection coefficient for a smooth painted surface is given as $h = 4.5 + 2.9 \cdot \upsilon_{Wind}$ in the unit of W/m$^2\cdot$K in Reference 31. The convection coefficients are dependent on many factors including surface roughness [35]. It is not easy to determine the convection heat exchange for a structure of a complex shape using numerical methods since the computational cost required to calculate heat transfer in the thermal boundary layer is high and the flow pattern continuously changes within a natural environment. Therefore, experimental calibrations are generally required.

## 2.2 Literature on Thermal Studies of Bridges and Guideways

Researchers on bridge structures under thermal environment have been interested in the estimation of the tensile stresses due to temperature gradients in concrete bridges since the tensile cracks in continuous concrete bridges were of concern. Various numerical models representing bridge structures and thermal environments have been developed to evaluate temperature distributions, stresses, and deformations. Similar methodology has been followed in the study of guideways made of steel and concrete. However, for the guideways in high-speed transportation, considerations are given more to deformations than to stresses.

### 2.2.1 Thermal Studies on Bridge Structures

In general, the analytical and the experimental studies started with one-dimensional models for heat transfer analysis, and have advanced to two-dimensional models for heat transfer analysis coupled with three-dimensional structural analysis.

Priestley [8] studied stresses induced by daily temperature variations in concrete bridges. Since stresses induced by the temperature variation in the transverse direction was considered to be insignificant due to the fact that the overhang provided shading on the exterior surfaces of bridges, it was assumed that the temperature varied only in the vertical direction without any change in the transverse or longitudinal direction. Temperature distribution of a sixth power parabola varying from a maximum at the top surface to 0°C at the bottom was recommended for bridges of approximately 1.2 m to 1.5 m depth. This sixth order curve with a maximum temperature difference of 30°C was used as a design thermal gradient for bridges in New Zealand [9].

Hunt and Cooke [11] developed a linear heat flow model with two layers of different thermal properties using the finite difference method, in which one layer could be used to represent the blacktop on the deck of bridges. The effective sky temperature was assumed to be the same as the air temperature during the day, and was set to –45°C (228 K) during the night. The heat transfer coefficients containing the effect of convection were constant, which suggests that the effect of wind speed variation was not taken into account.

In a later study, Priestley [9, 10] recommended a fifth order curve for temperature distribution in a vertical direction instead of the sixth order curve. The temperature distribution was calculated numerically using a linear heat flow model with multiple layers. In the study, meteorological data were used for the simulation, and days with high solar radiation, low ambient temperature variation, and low wind speed were considered to be critical. This fifth order curve has been adopted in the bridge design specifications in New Zealand [10].

Thepchatri, Johnson, and Matlock [12] developed a two-dimensional model based on the finite element method, and applied it to calculate temperature distributions in the cross section of concrete bridges. The temperature in the longitudinal direction was assumed to be uniform, and thermal stresses were obtained from the structural analysis based on elastic beam theory. Solar radiation data were from the U. S. Weather Bureau, while air temperature and wind speed data were obtained from local newspapers. The analysis using such a two-dimensional model made it possible to account for transverse heat flow. In the verification of the model, the discrepancy between analysis results and the measured data on the bottom surface of the bridge was noted, and was considered to result from the solar radiation that was reflected on the roadway under the bridge. It was corrected by assuming that 10 percent of the measured solar radiation intensity was reflected by the roadway and absorbed by the bridge's bottom surface.

Will, Johnson, and Matlock [13], and Yargicoglu and Johnson [14] also used the same model developed in Reference 12 for the thermal analysis. However, the structural analysis was based on a three-dimensional model, in which concrete structures were represented by shell elements.

Potgieter [15] developed a vertical heat flow program which is similar to the program developed by Hunt and Cooke [11] to evaluate temperature distributions and thermal stresses of concrete bridges. Maximum temperature gradients in concrete bridges were estimated with meteorological data from 26 SOLMET (SOLar METeorological) stations. The same values of the effective sky temperature that Hunt and Cooke used were adopted. It was noted that the radiation on the vertical surfaces facing east and west was high in the early morning and the late afternoon, and that the overhang prevented most of the solar radiation on the vertical surfaces when the overhang was larger than 1 m, limiting the temperature increase due to direct solar radiation on the vertical surfaces to less than 3 or 4°C.

Elbadry and Ghali [19] developed a finite element program, FETAB, which considered heat flow in two-dimensional cross sections. One-dimensional fictitious elements were used to represent boundaries. The solar radiation was calculated by considering the attenuation that results from the atmosphere, and the solar radiation on the boundary was calculated by considering the incident angles of the solar rays on the surfaces. The effect of shading due to the overhang was considered by calculating the size of the shadow on the web, and the solar radiation in the shaded region was assumed to be zero, which appears to imply that the solar radiation was considered as direct radiation. The air temperature was interpolated as a sine curve using both the maximum and the minimum temperatures for the day, and the uniform change of the air temperature inside box sections was taken into account. The ambient air temperature appears to have been used as the effective sky temperature.

Moorty and Roeder [17] did one-dimensional heat transfer analysis based on the finite difference method and two-dimensional structural analysis using ANSYS to assess the thermal movements of bridges. In a similar manner to that described in Reference 15 and 19, the solar radiation was obtained analytically, and the incidence angles were considered. For a curved girder, the level of solar radiation on the sides was calculated using the solar angles, the depth of the girder, and the length of the overhang. Heat transfer coefficients were used with the average daily wind speed.

Fu, Ng, and Cheung [20] considered the shading due to overhang and the heating in an enclosed box of composite bridges. A two-dimensional analysis using ADINAT determined temperature distributions in the cross section, and the results from the thermal analysis were used in SAP-IV to perform a three-dimensional structural analysis. It was noted that the steel girder showed a rapid increase in temperature when exposed to direct solar radiation. Regarding the effect of uniform temperature change of the enclosed air, it was mentioned that the enclosed air raised the temperature of the steel plates that were not under direct radiation. Solar absorptivity values of 0.8 for rusted steel and 0.65 for concrete, and emissivity of 0.84 for both steel and concrete were used in the simulation.

Tong, et al. [21] developed a two-dimensional program and applied it for the calculation of temperature distributions in steel bridges. Direct and diffuse radiations were separated from the global solar radiation, and were summed by considering the incident angle of direct solar radiation on the surfaces. The effect of shading was considered by a three-dimensional projection of solar rays. For exterior bottom surfaces and interior enclosed surfaces, the solar radiation was taken to be zero. Heat transfer coefficients were assumed to be constant in the model, and outgoing radiation due to the difference between the air temperature and the effective sky temperature during the night was set to be constant at around 85 $W/m^2$.

Ho and Liu [22] emphasized that the difficulties lie in the uncertainties of the boundary conditions as well as input parameters since weather conditions change in a random manner, and they showed a method for determining the thermal loadings on highway bridges with a 50 year return period using a one-dimensional model.

Tong, et al. [23] presented design thermal loadings for a 50 year return period based on meteorological data in Hong Kong using the numerical model in Reference 21.

For the design of bridge structures, current AASHTO specifications [28] provide guidance on the values of effective bridge temperature and thermal gradients. The effective bridge temperature is used to calculate thermal expansion of a bridge to determine the required capacity of the expansion joints and the seats. The effective bridge temperature is based on the work done by Roeder [18]. Contour maps, which are similar to those made by Emerson in England, provide maximum and minimum effective bridge temperatures based on the correlation between bridge temperature and climatic conditions. The temperature gradient is represented by a multi-linear curve, which is similar to a simplified form of the New Zealand fifth order curve. Design values in the multi-linear curve are determined depending on the solar radiation zone, which is classified into four separate zones [15]. The classification was based on the average daily global solar radiation on a horizontal surface obtained from 26 SOLMET stations in July [16].

### 2.2.2 Thermal Studies on Maglev Guideways

The specifications for highway bridge structures may not be adequate to calculate stresses and deformations of Maglev guideways. No guidance is given on the deformation in the lateral direction in such specifications. In addition, the Transrapid guideway specifications do not address the thermal effects in detail. The system is only verified in Emsland, Germany, and Shanghai, China, where the weather is temperate. Therefore, various numerical studies have been undertaken to assess the validity of the performance of guideways under other environments.

Campbell and Siu [24] worked on guideways proposed for the southern California to Las Vegas corridor. A program, FETAB, described in Reference 19, was used to simulate 25 m single-span concrete and steel guideways in that thermal environment. The guideways had shapes similar to those in Emsland, Germany, with 2800 mm width and 2150 mm depth. The air temperature varied in a sinusoidal curve between 38°C and 18°C for the summer, and between 15°C and –3°C for the winter. It was discovered that significant curvatures and deflections were induced due to the thermal gradients, and that these effects could be mitigated by utilizing surface coatings on the guideways. When the steel guideways were assumed to be oxidized, the maximum vertical deflection was 14.8 mm during the summer, while for the guideways with white coatings, the maximum vertical deflection was 6.7 mm. Horizontal deflection was reduced from 6.9 mm to 1.7 mm with the use of white coatings on the sides as well as on the top surface of the guideways.

Samavedam and Purple [25] conducted research on thermal effects on continuous sheet guideways with aluminum sheet, with which the significance of eddy current heating had been identified. These types of guideways are generally used for EDS systems. The New Zealand specifications were used to compare the thermal responses. Parametric studies were carried out to assess the thermal effects, and the methods for mitigating the effects such as buckling and tensile fracture in the sheets due to thermal expansion and contraction were discussed, including the use of expansion gap in continuous sheet guideways. It was stated that two-span guideways were better than single-span guideways, and the benefits of the white surface coatings in reducing the thermal deflections were addressed.

Kokkins, Purple, and Samavedam [26] studied the behaviors of EMS guideways under the typical thermal environment of Orlando, Florida using FETAB [19]. The guideway was 2930 mm wide and 1950 mm deep, and was in proposal for deployment in Florida. It was identified that the ratio of solar absorptivity to emissivity was the most influential index of thermal deflection, and it was not considered reasonable to design the structure using the thermal properties of new coatings since thermal properties of aged coatings are close to those of oxidized steel. Survey results indicated that the solar absorptivity of new white coatings was 0.26, and that it could increase higher than 0.6 as the coatings deteriorated and became contaminated with dirt and pollution. Therefore, behaviors of guideways with the surface properties of an oxidized surface, which might be caused by a loss of coatings for a variety of reasons including poor maintenance, were considered as well. For 25 m single-span guideways with the surface properties of oxidized steel, assuming solar absorptivity of 0.8 and emissivity of 0.8, the maximum vertical deflection was 10.4 mm during the summer with the guideway oriented in the north-south direction, and the maximum lateral deflection was 7.5 mm during the winter with the guideway in the east-west direction. Untreated steel with solar absorptivity of 0.6 and emissivity of 0.2 showed slightly larger deflections. It was stated that the single-span guideways might not be feasible due to large deflections, and two-span guideways, with which the deflection was about 30% of the deflection of a single-span guideway, were recommended.

Mangerig, at al. [27] developed software for thermal analysis, applied it to various existing or planned guideways in Emsland, Germany, and demonstrated that the deflection criteria were violated for all guideways for a couple of days per year. The effect of shadow coverage on one span of a two-span Transrapid Type III steel guideway was demonstrated, and the necessity to consider the effects of partial shading on guideways such as the effect due to other parallel guideways was noted. Some of the design changes to reduce the thermal effects on the guideways were discussed, and mitigating efforts such as adding temperature compensating shapes to the bottom part of the guideways to induce equal temperature in the top and bottom parts of the guideways, implementing partial column integrated guideway types, and making ends of guideways continuous by connecting ends were discussed.

The research on guideways has been dependent mostly on two-dimensional numerical models. The numerical models assume that the heat transfer in the longitudinal direction is negligible and the effect of partial shading is not significant. For the type of guideways with which the longitudinal heat transfer is to be taken into account or with which the effect of partial shading affects the performance, three-dimensional models are needed for proper consideration of the performance and the design of guideways in various thermal environments. Therefore, a three-dimensional numerical model of the thermal environment is implemented to provide a general purpose tool to determine the thermal behavior of guideway structures given the presence of conditions under which either the heat transfer in the longitudinal direction or the effect of partial shading exist. This model makes it possible to compare existing guideway designs with a new design and to assess the suitability of a new design to various thermal environments.

# CHAPTER 3
# EXPERIMENTAL DATA

Experimentation was conducted to study the temperature distribution within a girder under various thermal environments. To evaluate the thermal environment, meteorological data influencing the surface heat flux were either measured or obtained from weather data records. Under this environment, the temperatures of a trapezoidal girder were measured. The girder was significantly corroded on the surface with similar thermal properties to the oxide film on weathering steel. In this chapter, the data contained in Reference 29 are summarized and reinterpreted for the calibration of the numerical model. More detailed information on the configuration of the experimentation and the measured data can be found in Reference 29.

## 3.1 Instrumentation

### 3.1.1 Girder Temperature Data Collection

A trapezoidal box girder, which is approximately 16.5 m long and 1.4 m deep, is shown in Figure 3.01 along with its surroundings. The girder was positioned on the west side of the Ferguson Structural Engineering Laboratory, which cast partial shading or full shading on the girder for a few hours during the day. As shown in Figure 3.02, thermocouples were installed at various locations in the cross section of the girder.

Figure 3.01 Configuration for Girder Temperature Measurement

(a) Instrumentation (Courtesy of Richards [29])

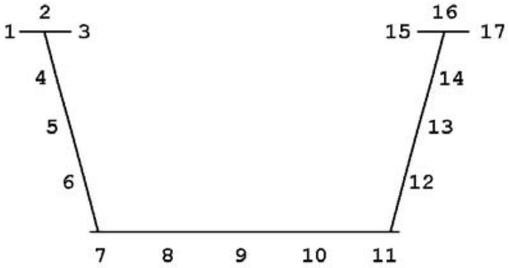

(b) Position of Thermocouples

Figure 3.02 Instrumentation for Girder Temperature Measurement

### 3.1.2 Solar Radiation Data Collection

Solar radiation data were obtained from two locations. These locations are named FSEL and UTME. FSEL is where the trapezoidal girder was set up next to the Ferguson Structural Engineering Laboratory in order to measure the girder temperature as shown previously in Figure 3.01. In addition to the girder temperatures, global horizontal radiation and air temperature were measured at the location. Since the direct normal radiation component and the diffuse horizontal radiation component, which are necessary for the numerical simulation, were not available at FSEL, solar radiation sensor readings from another location, UTME, were obtained. UTME is located about 11 km south of FSEL and is on a roof of a ten story building. Sensor readings include global horizontal radiation, direct normal radiation, and diffuse horizontal radiation. The equipment used for the measurement of solar radiation were an Eppley PSP

(Precision Spectral Pyranometer) for global radiation, an Eppley NIP (Normal Incidence Pyrheliometer) for direct normal radiation, and an Eppley PSP on a SCI-TEC Tracker with a shadow ball for diffuse radiation.

On clear days, a strong correlation exists between the solar radiation at FSEL and at UTME. In the case of cloudy days, such correlation is not possible between the solar radiation measured at one location and that measured at another because of the difference in the amount of cloud coverage between the two sites; clouds may cast shade on the radiation sensor on one location while not casting any shade on the sensor at the other. Clear days were selected based on the solar radiation data obtained from UTME. There are only a few clear days on which temperature data were measured on the girder. The following dates represent the selected days during 2004: August 4, November 25, November 27, and December 11 through 14. The meteorological data and the girder temperature data on these days are used for the simulation and the calibration of the numerical model.

Solar radiation components on August 4, 2004, which was a clear day judging from the sensor readings, are plotted in Figure 3.03. In the figure, GHR is the global horizontal radiation, DNR is the direct normal radiation, and DHR is the diffuse horizontal radiation.

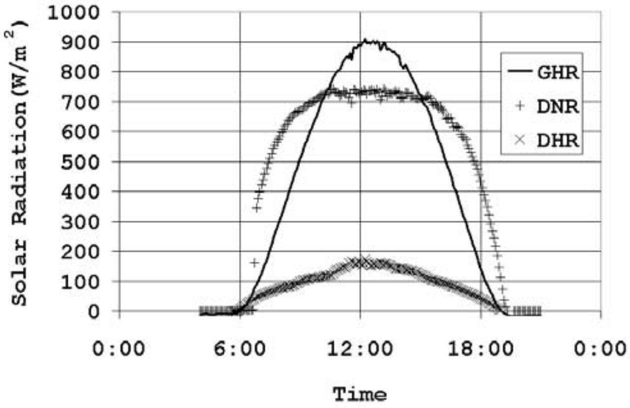

Figure 3.03 Solar Radiation Sensor Readings at UTME on August 4, 2004

A comparison of the plots of solar radiation components on a day in summer shown in Figure 3.03 and another day in winter shown in Figure 3.04 makes the differences apparent. As noted in Equation 2.3, the angle of incidence plays a role on the conversion of direct normal radiation component to global horizontal radiation. In the summer data readings shown in Figure 3.03, the global horizontal radiation at noon is close to the sum of direct normal radiation and diffuse horizontal radiation component since the angle between the solar rays and the surface normal is close to zero. Even though direct normal radiation in winter is higher than in summer, the global horizontal radiation in winter is much less as shown in Figure 3.04 because of the angle of incidence.

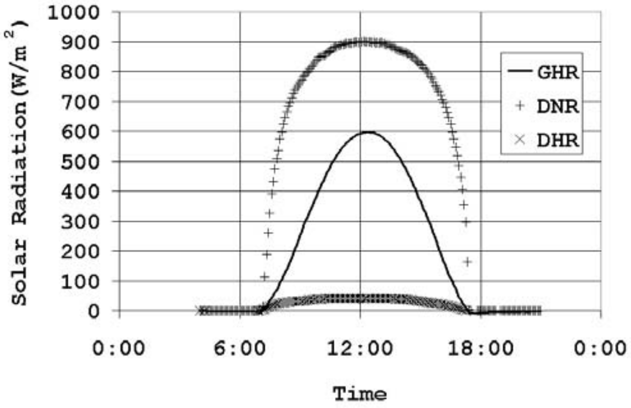

Figure 3.04 Solar Radiation Sensor Readings at UTME on November 25, 2004

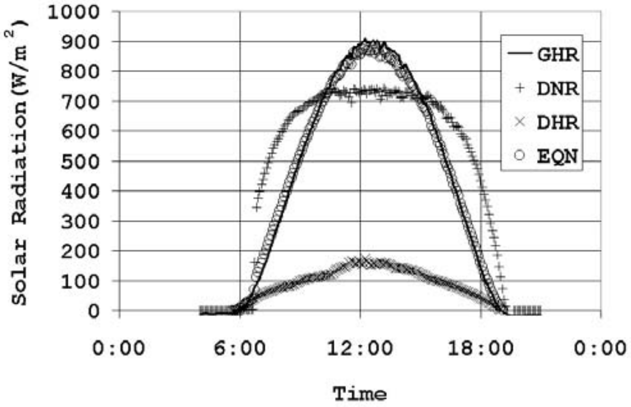

Figure 3.05 Predictions of Solar Radiation at UTME on August 4, 2004

The validity of equation 2.3 is shown in Figure 3.05, where EQN represents the predictions based on the equation. The equation predicting the global horizontal radiation from the direct normal radiation component and the diffuse horizontal radiation component works well for the solar radiation on August 04, and is expected to be valid for other clear days. However, on this day there may have been a partial cloud in the sky. Daily records from a local weather station indicate partial cloudiness around noon for a short duration of time even though the data plots of the radiation sensor readings do not appear to indicate such conditions. This may imply that the cloud over the weather station was not present at UTME during the sensor readings.

As a means of comparison, solar radiation readings on a cloudy day are shown in Figure 3.06. The radiation readings fluctuate in the afternoon as the clouds shield the sun's radiation. The daily records from a local weather station also indicate cloudiness in the afternoon. For cloudy days, it is not likely to be acceptable to use the solar radiation data obtained from a location far away from the location where the radiation data are required because the solar radiation flux may be different from one measurement site to another due to the clouds. Therefore, radiation data should either be obtained at the location where the data are required or radiation data on clear days should be used.

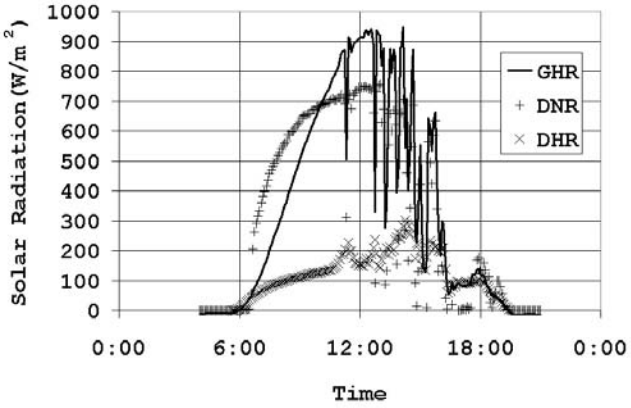

Figure 3.06 Solar Radiation Sensor Readings at UTME on a Cloudy Day

Another set of solar radiation data on November 25 is plotted in Figure 3.07. In the figure, GHR (FSEL) is the global horizontal radiation measured at FSEL. A comparison of the global horizontal radiation sensor readings from UTME with those from FSEL can be made. The global horizontal radiation data at FSEL contains a blackout region in the direct normal radiation component from the shade of a nearby building. The global horizontal radiation measured at FSEL is slightly higher than that from UTME. This is considered to be due to the reflection by the building and surroundings as well as measurement errors. When the sensor was under the shade, the radiation readings were close to the diffuse horizontal radiation.

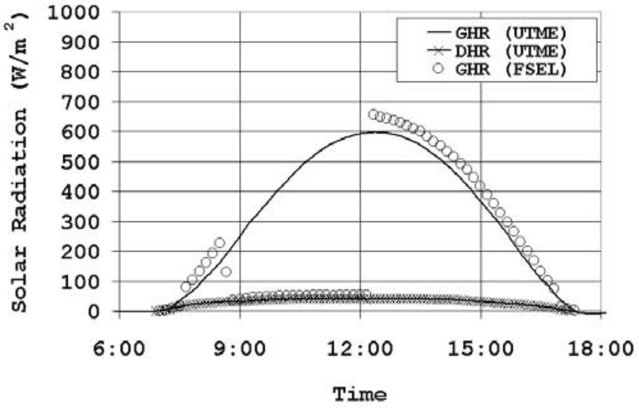

Figure 3.07 Solar Radiation Sensor Readings on November 25, 2004

### 3.1.3 Other Meteorological Data Collection

Other meteorological data such as wind speed were obtained from a local weather station, which is about 8 km southwest from FSEL. The wind data obtained from the local weather station is not expected to have a strong correlation to the wind speed at FSEL since the trapezoidal girder that was used for the temperature measurement was positioned close to a building which blocks the flow of wind in certain directions. The localized flow pattern of the wind around the building and around the girder is complex at the site, and thus the wind speed was not measured.

## 3.2 Summary of Girder Temperature Distribution Data

Temperature distribution of a girder on November 25 is plotted in Figure A.01 and Figure A.02. In Figure 3.08 and Figure 3.09, temperatures at each measurement point identified in Figure 3.02-(b) are plotted. As shown in Figure 3.08 and Figure 3.09, the redistribution of heat inside the steel structure occurs quickly. When there is not much solar radiation flux, the temperature of the girder quickly becomes uniform. The temperatures do not differ much until the solar radiation reaches the surfaces of the girder. Therefore, it can be assumed that the temperature in the girder is uniform during the hours before the sun rises. The decrease of the temperatures between 09:00 and 10:00 corresponds to the decrease of solar radiation because the direct solar radiation is completely blocked by the building. In the shade, the temperature in the girder became close to the air temperature again. When the girder was exposed to direct solar radiation again at noon, the temperature within it rose. When the girder was not under direct solar radiation, the air temperature was close to the lower limit of the girder temperatures.

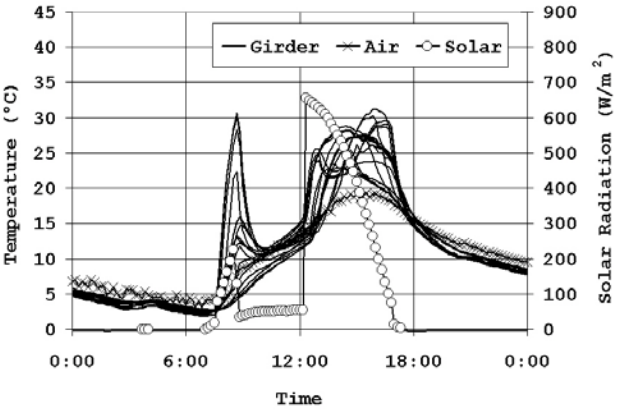

Figure 3.08 Girder Temperature at FSEL on November 25, 2004

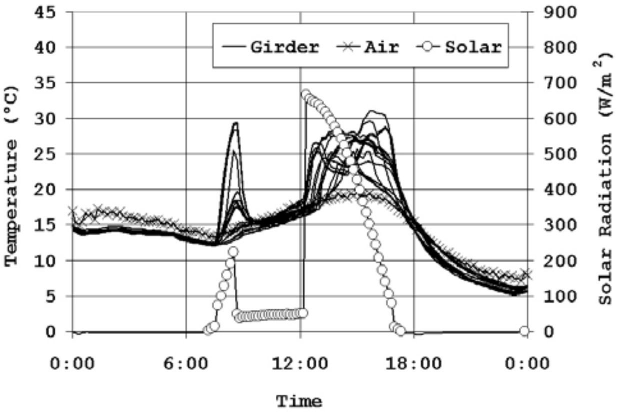

Figure 3.09 Girder Temperature at FSEL on November 27, 2004

A comparison of the thermal environment in Figure 3.08 and Figure 3.09 at around 09:00 shows that the solar radiation readings at FSEL on November 25 are almost the same as those on November 27. The different thermal environments are air temperatures as shown in Figure 3.10, wind speeds as shown in Figure 3.11, as well as the initial girder temperatures. The air temperature around 09:00 on November 27 is higher than that on November 25. Under such conditions, the maximum temperature around 09:00 on November 27 is expected to be higher. However, the maximum temperatures were close to each other. The wind speed around 09:00 on November 27 was higher than that on November 25, which may be the cause of the lower temperature on November 27. Therefore, compared to the thermal environment around 09:00 on November 25, the thermal environment around 09:00 on November 27 imposed more heating due to the higher air temperature and more cooling due to the higher wind speed. While the heating effect due to the solar radiation increases the temperature gradients, the effect of wind reduces the gradients.

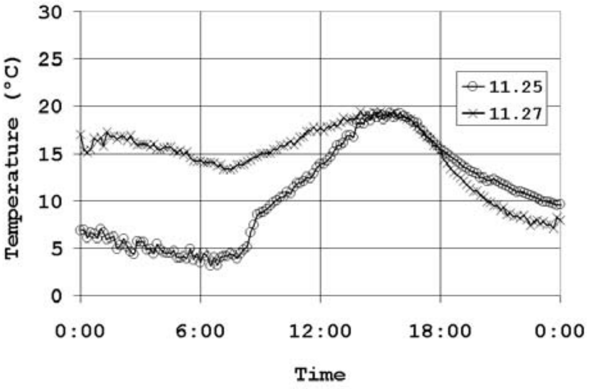

Figure 3.10 Air Temperature at FSEL on November 25 and November 27, 2004

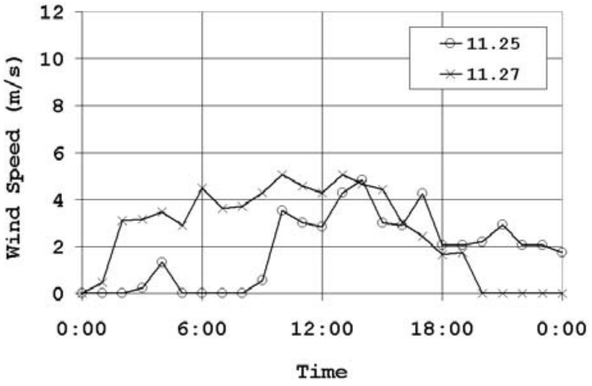

Figure 3.11 Wind Speed from Local Weather Station on Nov. 25 and Nov. 27, 2004

A comparison of the thermal environment at the time between 15:00 and 16:00 shows that the thermal environments are almost identical even though the thermal environments prior to that time were different. During the time between 15:00 and 16:00, the air temperatures were almost identical, as shown in Figure 3.10, and the wind speeds were similar, as shown in Figure 3.11. During the time, the temperatures in the girder show mostly similar patterns and magnitudes when compared with the data from November 25 and November 27 as shown in Figure 3.12 and Figure 3.13. The maximum temperatures, which occurred around 16:00, were the same even though the initial temperatures and the history of the thermal environments were different. Therefore, the initial thermal environmental state is not as important as the current thermal environment for the temperature profiles since the steel plates rapidly adapt to changes in the thermal environment.

In summary, the temperature in the girder is close to the air temperature provided there is no solar radiation. The solar radiation increases the gradients in the temperature profile while the wind flow reduces them. Even though initial conditions may be different, the temperatures converge rapidly to a state which is imposed by the transient thermal environment.

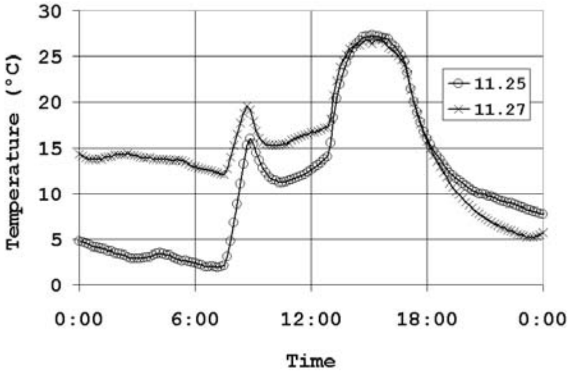

Figure 3.12 Girder Temperature at FSEL on Nov. 25 and Nov. 27: East Top Flange

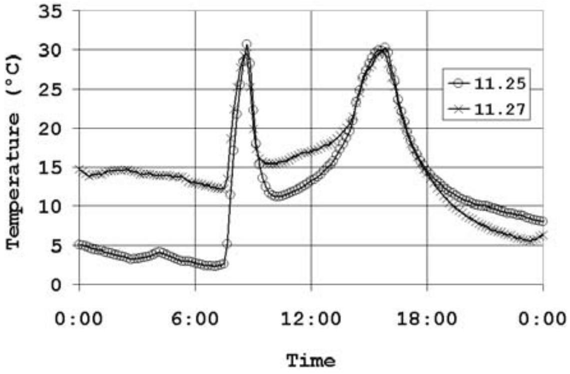

Figure 3.13 Girder Temperature at FSEL on Nov. 25 and Nov. 27: East Web

# CHAPTER 4
# NUMERICAL MODEL AND CALIBRATION

## 4.1 Development of Numerical Models

The overall simulation procedure for the calculation of deformations of a structure under thermal environments is shown in Figure 4.01. A finite element model of a structure and other surroundings, which could interact with the structure in thermal perspective, is created first. The finite element mesh information containing nodal coordinates and element connectivity is extracted, and is used as geometry data to the thermal environment simulation program. This extracted data also contains information on sets that are used for the identification of regions with specified surface properties. Data such as weather information, surface material properties, and parameters for the thermal environment simulation are fed into the program as well. The program determines surface heat flux for each element, which is used as an input to the finite element heat transfer analysis. The program also generates files that can be used for visualization, and this program was developed to help users visualize the state of the surface heat flux due to solar radiation for each increment of time.

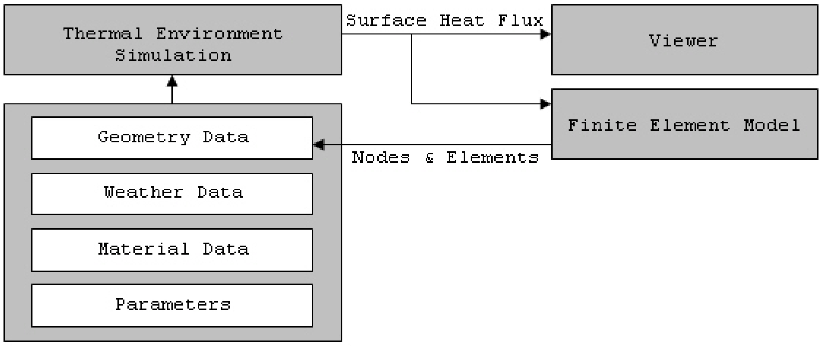

Figure 4.01 Overall Data Flow in Thermal Simulation

### 4.1.1 General Architecture of Numerical Models

The general architecture of the numerical model appears in more detail in Figure 4.02. The program consists of several modules: one reads the finite element mesh data and set information and also reconstructs the geometry model from the mesh data; another calculates the position of the sun; another reads the solar radiation; another reads surface properties and relates these to the element surface properties; another reads other meteorological data such as air temperature; another processes the information on analysis parameters; and the other calculates the surface heat flux. The program for thermal environment simulation determines heat flux on the surfaces of each element for each time increment with the solar position, meteorological data, surface properties, and geometries. The surface heat flux on each element is fed into the finite element software for the transient heat transfer analysis, and the temperature distribution under the specified heat flux is determined. The temperature distribution obtained from the heat transfer analysis is again fed into the finite element software for the structural analysis which calculates the stresses and deformations.

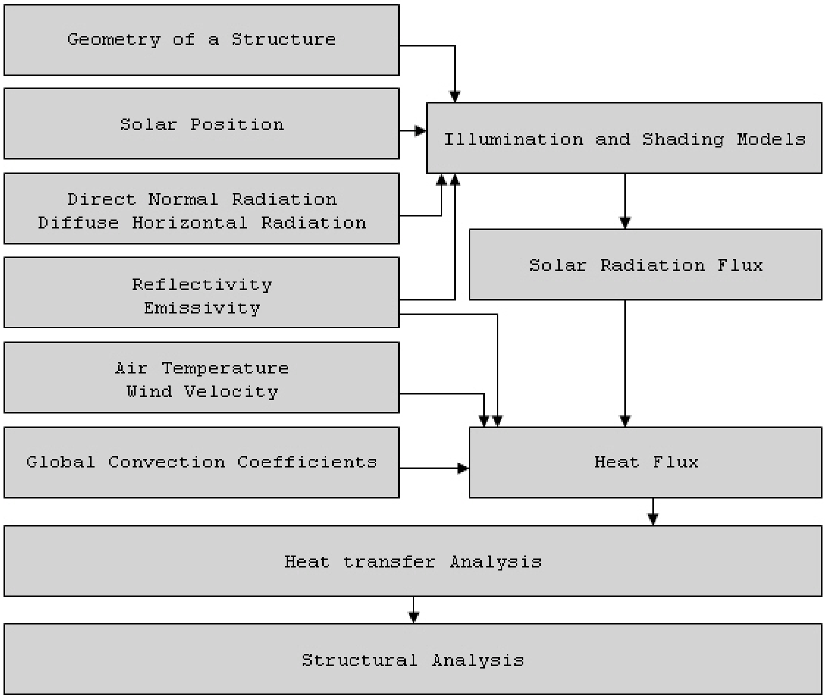

Figure 4.02 Scheme for Thermal Deformation Simulation

### 4.1.2 Data Collection and Data Processing

The numerical model of the thermal environment is discussed in this section as well as assumptions made in the model.

#### 4.1.2.1 Solar Position

The position of the sun at each increment of time is determined by SPA (Solar Position Algorithm) [33]. The SPA is available from the National Renewable Energy

Laboratory, and the outputs from the SPA include the solar zenith and azimuth angles. The solar position is necessary to determine the angle between the solar ray and the surface normal direction and to determine which surfaces are shaded.

#### 4.1.2.2 Solar Radiation

Solar radiation data can be measured using pyranometers or can be obtained from local weather stations [31]. Solar radiation data available from common weather stations are global horizontal radiation. The simulation requires direct normal radiation and diffuse horizontal radiation components to determine the solar radiation on inclined surfaces. In Reference 20, direct normal radiation and diffuse horizontal radiation components were separated from global horizontal radiation. However, it is considered to be more accurate to use components that are obtained from sensor readings than to use those that are decomposed from global horizontal radiation analytically. Therefore, the radiation components that are collected from UTME are used for the calibration of the numerical model. For the simulations under the thermal environment of other locations, TMY2 (Typical Meteorological Year) data set [30], which contains typical values of the weather conditions for various locations in the United States, can be read and used as an input to the numerical model. The meteorological data in the TMY2 data set include both direct normal radiation and diffuse horizontal radiation components. This data set is generally used in simulations on solar energy conversion and on the heating and cooling needs of buildings [30]. As the name implies, this data set does not represent extreme conditions. Therefore, results obtained from the simulations with the TMY2 data would represent typical thermal behavior.

The Radiation on a horizontal surface due to solar radiation can be calculated by Equation 2.3. The equation assumes that the surface is not blocked by any other surfaces and that the surface is on a flat horizontal plane. When a surface is under the influence of other surfaces or when a surface is inclined, Equation 4.1 describes the amount of radiation on the surface:

$$G_{Solar} = G_{DNR} \cdot \cos\theta + G_{DHR} F_{Sky} + G_R \tag{4.1}$$

where $F_{Sky}$ : ratio of the sky view factor of a surface to that of a horizontal surface,

$G_{DNR}$ : direct normal radiation component (W/m$^2$),

$G_{DHR}$ : diffuse horizontal radiation component (W/m$^2$), and

$G_R$ : solar radiation that is reflected by other surfaces to a surface (W/m$^2$).

The second term, $G_{DHR}F_{Sky}$, which is the fraction of the diffuse horizontal radiation on a surface, represents the diffuse radiation on a surface that may not be on a horizontal plane. A method similar to the method described in Reference 32 is used for the calculation of the diffuse radiation on the surface. It is assumed that the diffuse solar radiation is emitted by discretized surfaces of the half sphere that represents the sky. The ratio between the heat flux on a unit area on the surface and the heat flux on a unit area on a horizontal plane is determined using view factors, and the diffuse horizontal radiation component is multiplied by the ratio to obtain the diffuse radiation on the surface. The effect of shading on the heat flux due to diffuse radiation is also accounted for in the numerical model.

#### 4.1.2.3 Reflection

Radiation that is reflected on a surface is assumed to originate diffusively from the surface. Under this assumption, the amount of radiation energy that originates from one surface to another surface can be determined by view factors [35]. In the implementation of this assumption in the reflection model, the view factor formula used in ABAQUS [37], which was derived from the one described in Reference 36, is implemented with a slightly different format. The energy that is reflected by one surface to another surface can be reflected back again to the original surface. Therefore, this reciprocal situation generally requires the setting up of a system of equations describing the relationship of all element surfaces to allow for an estimate of the amount of additional radiation due to reflection. In the implementation of the reflection model, calculation is done iteratively instead of through setting up a system of equations. Solving such a system of equations is time-consuming because the number of elements is large. Using this method, the absorbed radiation is subtracted from the radiation on each surface, and the remaining energy is redistributed to other surfaces according to the view factor. The term for the number of times this calculation is done for each surface is reflection depth. In the simulation, a reflection depth of 2 was used since most of the surfaces involved in the simulation have low solar reflectivity values.

#### 4.1.2.4 Reflectivity and Emissivity

Reflectivity and emissivity describe the surface properties of a material. The set information in the geometry data relates the name of the set to the element numbers. The material property data relate the name of the set to the solar reflectivity and emissivity of the front and back surfaces of the elements in the set. Therefore, the relation of the solar reflectivity and emissivity to the surfaces on each element can be determined.

#### 4.1.2.5 Air Temperature and Wind Velocity

These meteorological data are commonly available from the weather stations and are also available in TMY2 data sets. Data on the direction of the wind flow are not accounted for in the numerical model. The data are arranged in increments of time and the values in between them are interpolated linearly.

#### 4.1.2.6 Global Convection Coefficients

Convection coefficients $h_0$ and $h_1$ in Equation 2.9 were obtained by calibration. Since the heat flux is calculated for the surfaces of each element, accurate calculation may require the convection coefficients for each surface of the elements. However, the calibration process cannot provide enough information for such an evaluation. Aside from that, different geometric shapes would require different convection coefficients. Since the effect of convection on the differential temperature distribution is considered to be less than that of solar radiation, and since the steel distributes heat quickly, the convection coefficients are determined only on a global scale. A distinction is only made between the surfaces exposed to wind flow and the surfaces enclosed inside a structure. After determining if a surface is enclosed inside a structure or not, the surfaces inside enclosed space are assumed to be under free convection represented by $h_0$ only, and the other surfaces are assumed to be influenced by both $h_0$ and $h_1$. A more accurate numerical model would require the evaluation of wind speed on each surface of the elements.

#### 4.1.2.7 Illumination and Shading Models

To determine if a surface on an element is shaded, each ray originating from the center of the element in the direction of the solar position is tested to determine if it is blocked by other elements. Since this calculation takes a lot of time, a simple space partitioning scheme has been devised to reduce the time for computation of hit testing. This scheme is explained in Appendix B. Another way to reduce the computational time is to use the original geometry from which the finite elements are generated. Each ray originating from the center of the element could be tested against the surfaces of the original geometry instead of elements in the finite element mesh. If the original geometry were composed of simple geometric shapes, the computational time would be less. This method of using original geometry has not been implemented, and the numerical model uses the finite element mesh as geometry for the shading calculation.

## 4.2 Calibration of Numerical Models

The numerical model was verified to see if it could represent the thermal environment measured at FSEL. First, the solar radiation was verified to see if it could correctly represent the measured sensor readings. Then, the temperatures from the trapezoidal girder were compared with the results from the numerical model in order to determine global convection coefficients.

### 4.2.1 Solar Radiation Model

The solar radiation reading from FSEL is the global horizontal radiation measured by a pyranometer. The pyranometer was installed close to the girder. Due to its location, the sensor could be under the shade cast by a nearby building. The direct normal radiation and diffuse horizontal radiation component obtained from the sensor reading at UTME were used to predict the global horizontal radiation at the sensor location at FSEL. Figure 4.03 plots the sensor readings at FSEL and the results obtained from the numerical model. This radiation on the horizontal plane is the sum of both the direct normal radiation and the diffuse horizontal radiation. During the time when the sensor was under shade between 09:00 and 12:00, the sensor read the diffuse horizontal radiation only. The simulation closely matches with the sensor readings at FSEL:

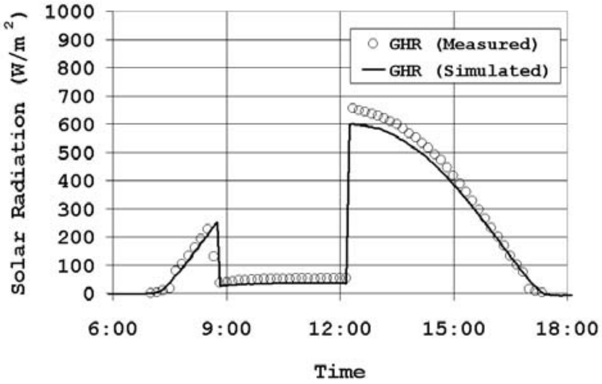

Figure 4.03 Solar Radiation Sensor Simulation on November 25, 2004

The solar radiation on the surfaces of a cube was simulated to demonstrate the dependency of the radiation flux on the surface normal direction. Figure 4.04 shows the solar radiation flux on the surfaces of a cube on a summer day. The top surface gets most of the radiation, absorbing the maximum around noon. The east surface receives most of the radiation in the morning while the west surface gets most in the afternoon. The radiation on the south surface is not large when compared to the east and west surfaces because of the angle of incidence.

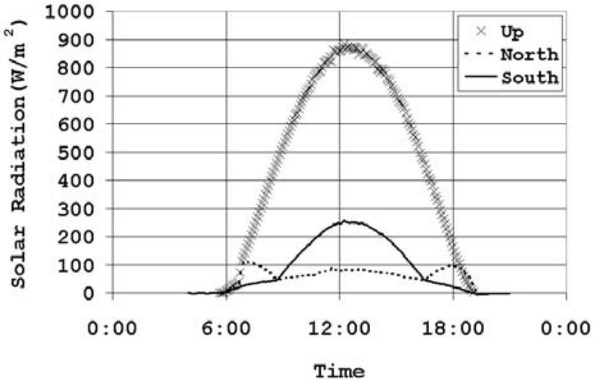

(a) Radiation on North and South Surfaces

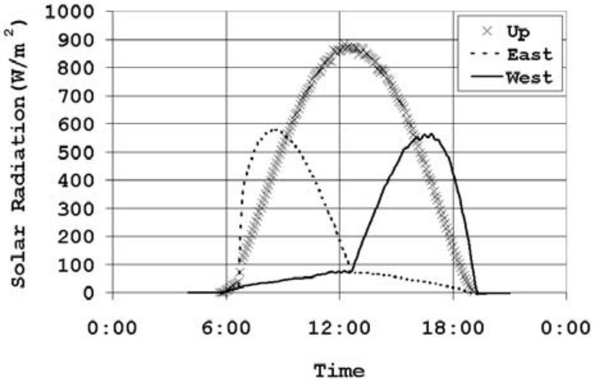

(b) Radiation on East and West Surfaces

Figure 4.04 Solar Radiation on a Cube on August 4, 2004

The radiation flux is always greater than or equal to the diffuse horizontal radiation component for the surface facing upward. The radiation on the other four surfaces is greater than or equal to half of the diffuse horizontal radiation component since the surfaces are only exposed to half of the sky. This phenomenon is shown in greater detail in Figure 4.05. The diffuse radiation on the top surface facing upward is the same as the diffuse horizontal radiation component. The diffuse radiation on the other surfaces is half the diffuse horizontal radiation component.

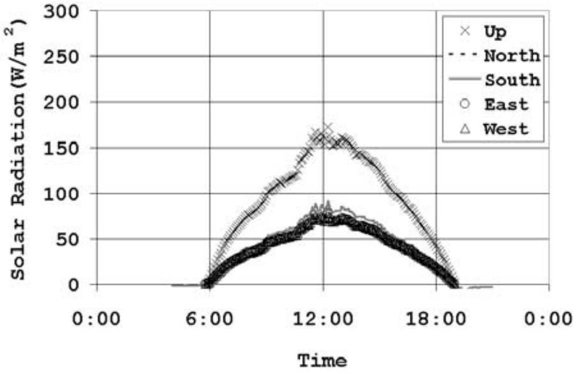

Figure 4.05 Diffuse Radiation on a Cube on August 4, 2004

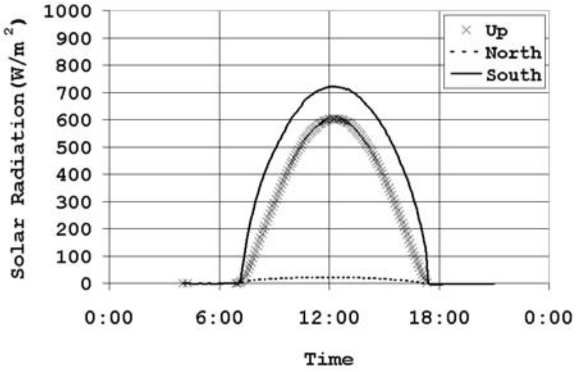

(a) Radiation on North and South Surfaces

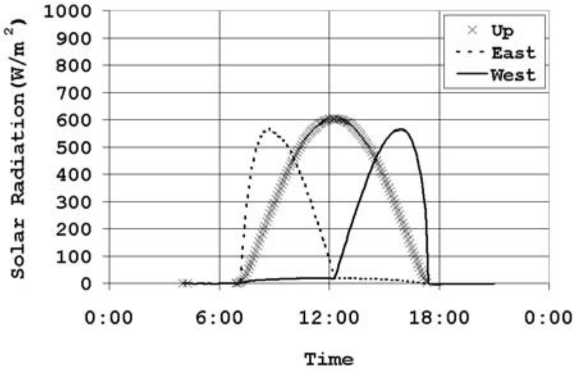

(b) Radiation on East and West Surfaces

Figure 4.06 Solar Radiation on a Cube on November 25, 2004

While Figure 4.04 represents the radiation on the surfaces on a typical summer day, the data shown in Figure 4.06 represent the radiation on a winter day. Since the position of the sun influences the incidence angle between the solar ray and the surface normal, the characteristics of solar radiation are different. Since the position of the sun in winter is lower than it is in the summer, the effect of direct solar radiation component on the south surface becomes more pronounced. Since the difference in solar radiation flux produces the temperature gradients, it can be inferred from the results in Figure 4.04 and Figure 4.06 that the gradient in the vertical direction would be dominant during the summer due to the large radiation on the top surface, and that the gradient in the north-south direction would be dominant during the winter due to the large difference in the radiation flux between the north surface and the south surface.

### 4.2.2 Shading Model

The shading calculation was verified using the data from the trapezoidal girder at FSEL. The environment was shown in Figure 3.01. The results from the shading calculation on December 22, 2005 are shown in Figure 4.07 through Figure 4.09. The viewer program generated the plots, and they include the position of the sun. The model includes the part of the exterior walls that cast shade on the girder. In Figure 4.07, the girder is mostly shaded except for a small region on the east side at the north end of the girder. In Figure 4.08 and Figure 4.09, the walls do not block the direct solar radiation on the girder. However, some parts of the girder are shaded by other parts of the girder.

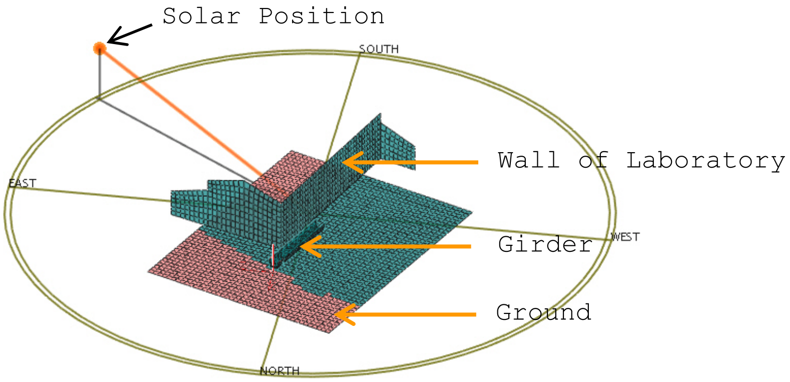

Figure 4.07 Overall Shading at 08:30, December 22, 2005

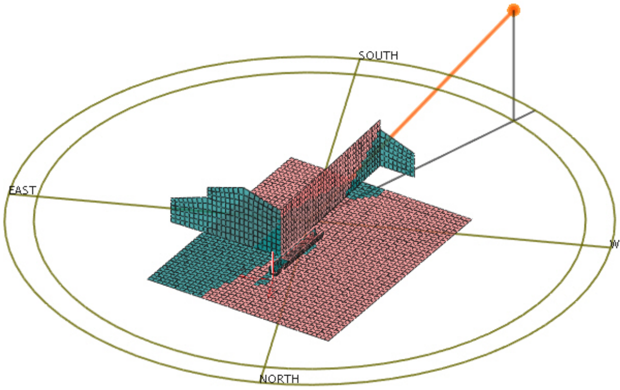

Figure 4.08 Overall Shading at 15:00, December 22, 2005

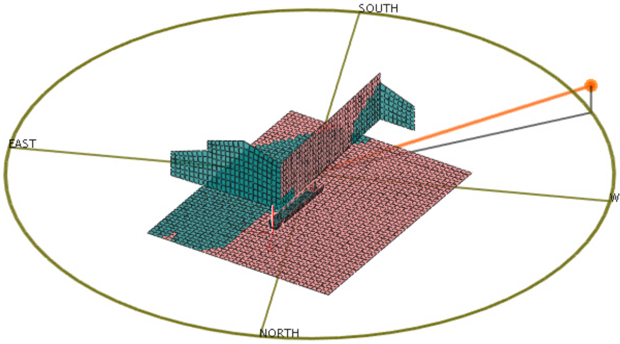

Figure 4.09 Overall Shading at 17:00, December 22, 2005

Figure 4.10 Shading Details at 08:30, December 22, 2005

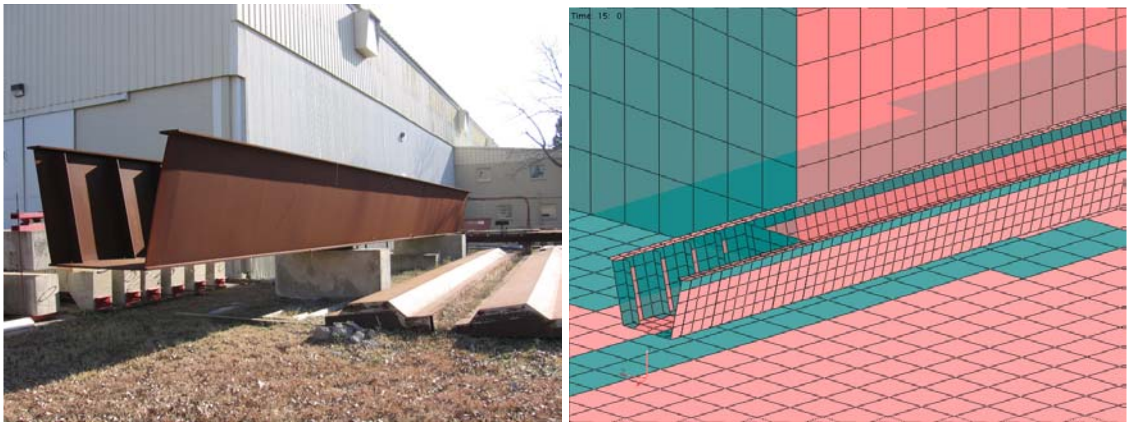

Figure 4.11 Shading Details at 15:00, December 22, 2005

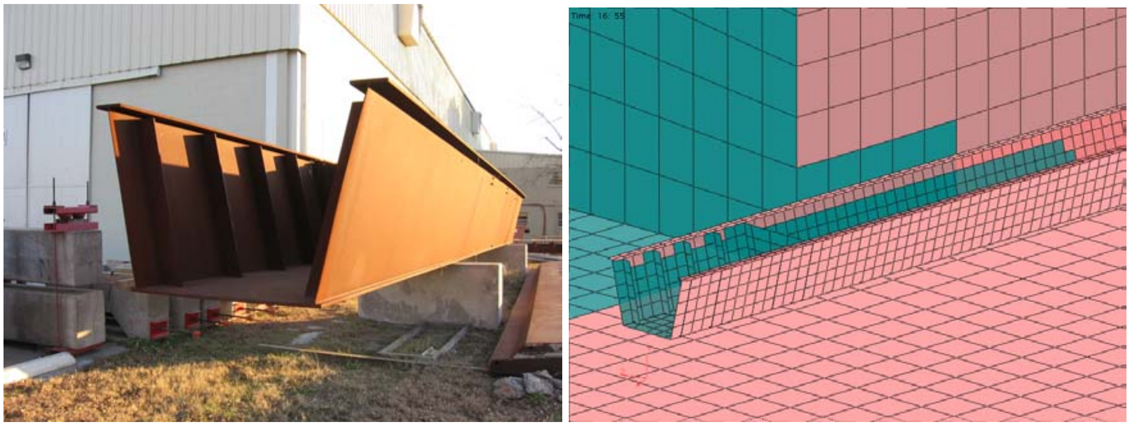

Figure 4.12 Shading Details at 16:55, December 22, 2005

The results from the numerical model are compared to the actual shade conditions in Figure 4.10 through Figure 4.12. The figures on the left are the actual conditions while the figures on the right are the results from the numerical model. In Figure 4.10, small regions on webs facing east receive direct radiation. In Figure 4.11, the shade on the webs is cast by the stiffeners, the diaphragm, and the top flanges. In Figure 4.12, the web on the right and the stiffeners cast shade on the web on the left. Nevertheless, even though a surface may be shaded, it still may receive diffuse radiation or reflected radiation. On the other hand, surfaces that are enclosed inside a structure are free from any solar radiation.

### 4.2.3 Reflection Model

The effect of reflection is demonstrated by the radiation flux comparison between the cases with and without such reflections. In the configuration shown in Figure 4.13, the surface solar reflectivity is set to be 0.12 for the girder, and is assumed to be 0.15 for the ground, and 0.25 for the walls. The solar radiation heat flux on surfaces at the top end of the left web marked in Figure 4.13 is plotted in Figure 4.14 and Figure 4.15. In these figures, the plot of global horizontal radiation is at the solar radiation sensor position. The maximum flux on the interior surface of the web corner occurs around 16:00 when the solar ray is close to parallel with the normal of the surface. The effect of the reflection on the surface is minor since there are few other surfaces that would reflect the radiation to the surface.

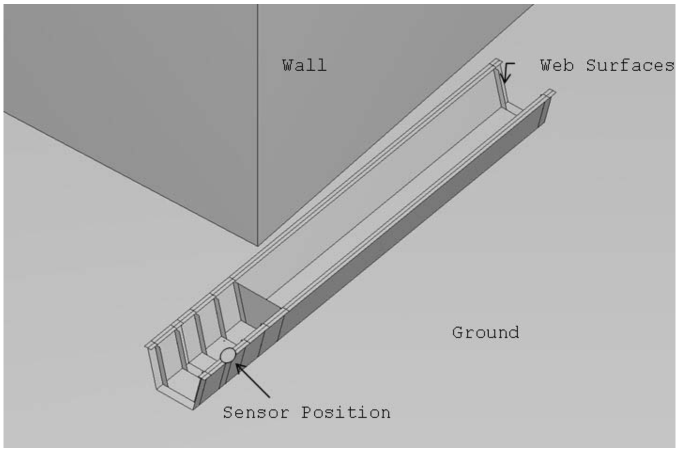

Figure 4.13 Configuration for Surface Reflection

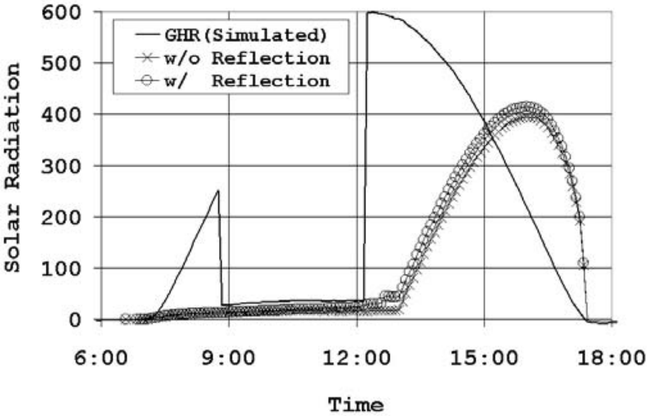

Figure 4.14 Reflection on Interior Surface of East Web on November 25, 2004

However, there are walls and ground that could reflect the radiation on the exterior surfaces. In Figure 4.15, if the reflection is disregarded, the exterior surface of the web gets little radiation flux since the surface is not directly exposed to any solar radiation except for during a short period of time. What is more, most of the diffuse radiation cannot reach the surface without reflection. Therefore, if the reflection is not taken into account, solar radiation flux on the surface does not exist for most of the time. When reflection is taken into account, some of the radiation flux on the walls and the ground after 13:00 is reflected to the surface. Under the assumed solar reflectivity of the materials, the radiation flux could reach 140 W/m$^2$. The reflected amount comes mainly from the wall in this case because more radiation reaches the wall due to the angle of the sun in the late afternoon and because the wall has higher solar reflectivity than the ground.

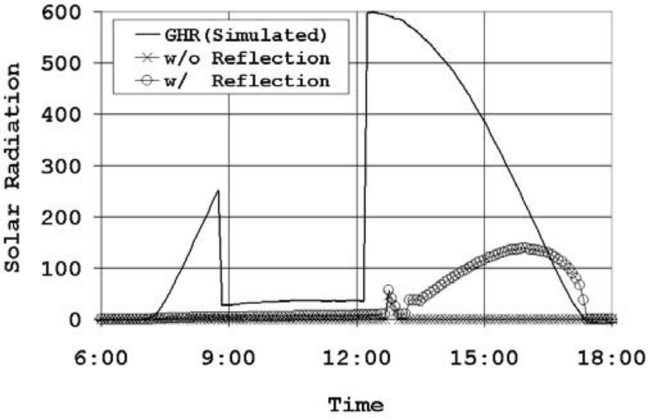

Figure 4.15 Reflection on Exterior Surface of East Web on November 25, 2004

### 4.2.4 Girder Temperature Calibration

Global convection coefficients are determined by comparing the numerical results and the experimental results. For the thermal environment simulation, a solar reflectivity of 0.12 and emissivity of 0.88 for steel, which were obtained from Reference 29, were used. On the other hand, solar reflectivity of 0.15 for the ground, and solar reflectivity of 0.25 for walls were assumed for the simulation. For transient heat transfer analysis, ABAQUS is used with four node heat transfer quadrilateral shell elements (DS4). The initial temperature is set to the average of the temperatures measured at 04:00, and the time increment is set to 600 seconds for the calculation.

#### 4.2.4.1 Effective Sky Temperature

The temperatures of the girder in the early morning before the sunrise were below the air temperature by about 1°C to 2°C. This phenomenon was shown previously in Figure 3.08 and Figure 3.09, which revealed that the average girder temperature before the sunrise was lower than the air temperature by 1.2°C and 1.4°C respectively. If the effective sky temperature is set to the air temperature in the numerical model, the heat flux is zero when the girder temperature is the same as the air temperature. As a result, the simulated girder temperature would not be below the air temperature. Therefore, the effective sky temperature which is lower than the measured air temperature should be used.

When the lower sky temperature is considered, the girder would tend to cool down to the effective sky temperature. At the same time, convection due to wind would increase the girder's temperature to reach the level of the air temperature. What follows is that if the effect of convection is significant, the girder temperatures should be close to the air temperature. The higher wind speed on November 27, which is shown in Figure 3.11, should have produced more convection than the wind on November 25, and the resulting girder temperature should have been closer to the air temperature on November 27 than on November 25. However, the average girder temperature showed temperatures 1°C to 2°C lower than the air temperature regardless of wind speed. It is possible that the localized wind flow around the girder on those days was similar even though the wind speeds from the weather station were different. Since the numerical model does not account for the localized wind flow patterns, it is assumed that the girder temperature is lower than the air temperature by 1 to 2°C regardless of the wind speed. Attempts to calibrate these differences using various effective sky temperatures did not give consistent results. The problem could be due to oversimplification of complex phenomena using a single value. Because of this likely complexity, the quantification of the effective sky temperature needs further study. Since the effective sky temperature itself is an approximate value, a simpler approach is taken as shown in Equation 4.2:

$$q = -\varepsilon\sigma\left(T^4 - \left(T_{Air} - 1.5\right)^4\right) - h\left(T - \left(T_{Air} - 1.5\right)\right) \tag{4.2}$$

In this equation, air temperature used in the numerical model is set to 1.5°C lower than the measured air temperature, and the effective sky temperature is set to this air temperature. When the temperature of the girder cools to 1.5°C below the actual air temperature, the heat flux becomes zero, and this represents the lowest temperature the girder can experience.

#### 4.2.4.2 Convection Coefficients

A higher convection coefficient reduces the maximum temperature and temperature gradients. The effects of convection are shown in Figure 4.16, in which the global convection coefficient, $h$ , varies from 5 $\mathrm{W/m^2 \cdot K}$ to 20 $\mathrm{W/m^2 \cdot K}$ by an increment of 5 $\mathrm{W/m^2 \cdot K}$. Given the results in Figure 4.16, a convection coefficient between 5 $\mathrm{W/m^2 \cdot K}$ and 10 $\mathrm{W/m^2 \cdot K}$ can be expected to give the temperature distribution that would match the maximum temperature at that point. However, instead of adjusting the convection coefficient until the maximum temperature from the simulation outputs matches the maximum temperature from the measured temperatures, a different approach is taken. Since the convection coefficient influences heat flux, the slope of the temperature variation is related to the convection coefficient. The convection coefficients were calibrated so that the increase of temperature at 14:00 on the simulation data matches the increase of temperature at 14:00 on the experimental data on December 11, 12, 13, and 14. The selected time was when the solar radiation and other environmental variables were stable. For the calibration on December 11 through 14, solar radiation readings on November 27 were used because solar radiation readings from UTME were not available for that month. Since the experiment was conducted close to a building, the flow pattern of the wind could change depending on the direction of the wind, and the calibrated convection coefficients could be slightly different from the convection coefficients to be used in a location where no other structures influence the flow pattern of the wind.

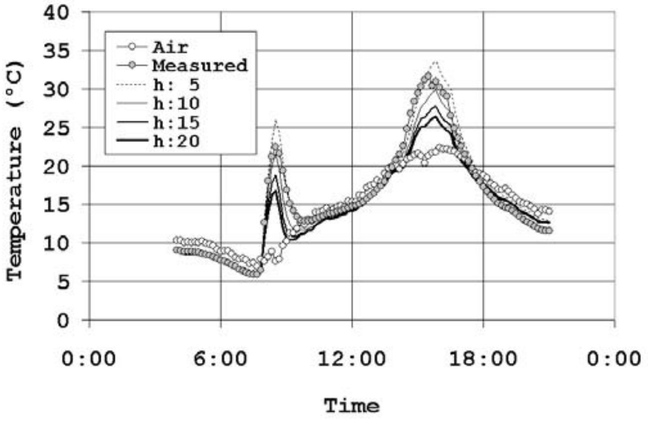

Figure 4.16 Effect of Convection at East Web on December 11, 2005

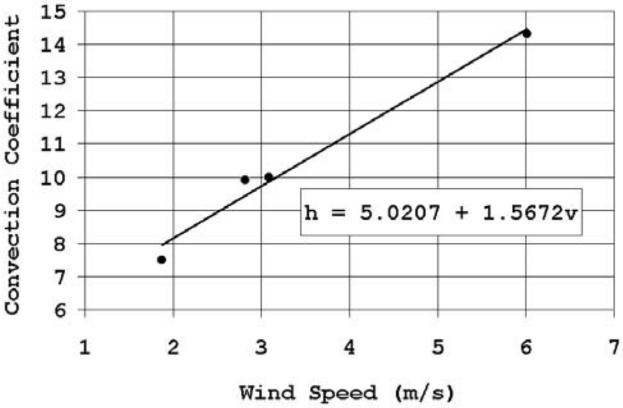

Figure 4.17 Calibration of Convection Coefficients at 14:00

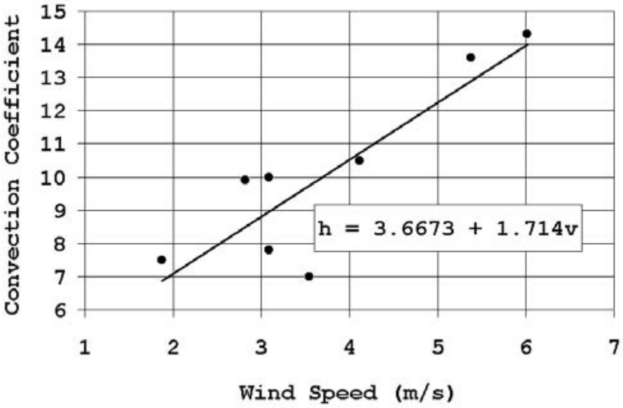

Figure 4.18 Calibration of Convection Coefficients at 14:00 and 15:00

For each measurement point in the cross section of the girder, the local convection coefficient is calculated. This coefficient represents the convection coefficient at that particular point. The global convection coefficient, which is to be applied uniformly on all points along the girder, is determined after averaging the local convection coefficients at each measurement point in the cross section. Figure 4.17 shows the correlation between the wind speed and the averaged convection coefficient. Calibration using additional data at 15:00 resulted in a slightly different result as shown in Figure 4.18. However, the point at which the wind speed was 3.54 m/s and the convection coefficient was 7 $W/m^2 \cdot K$ in Figure 4.18 occurred when the wind was from the SSE (South South East) direction. This implies that the wind was probably blocked by the building, and further that the girder would have experienced lower wind speed since the building is positioned on the south and east side of the girder. For other points in the figure, the direction of the wind was either variable or northerly. Therefore, calibration using data at 14:00 seems more reliable, and $h_0$ of 5.02 and $h_1$ of 1.57 are selected.

When these global convection coefficients are used, the actual convection values at each point of the girder are either under- or overestimated. Figure 4.19 compares the local convection coefficients required to match the heat flux at each point to the global convection values. The numerical model underestimates the convection on the bottom flanges and overestimates the convection for the rest of the sections. However, this comparison assumes that the error is only due to convection, disregarding the possibility for error in other environmental factors of the numerical model.

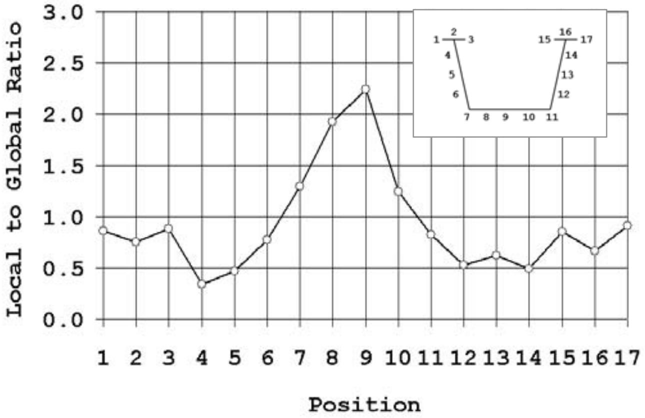

Figure 4.19 Local to Global Convection Coefficient Ratio at 14:00

### 4.2.5 Conclusions

A numerical model of a thermal environment that determines heat flux on each surface of finite elements was presented. This presentation emphasized the determination of solar radiation flux on a surface. Since shading influences the solar radiation flux, accurate estimation of a shade region is necessary. The shade region changes as the position of the sun changes and slight differences in the shading pattern can influence temperature variation in materials that are sensitive to solar radiation. Since one point on each finite element is used to determine if the surface is shaded or not, the element's size can affect the results' accuracy as well. Determination of the element's size and the magnitude of the time increment are dependent not only on temperature gradients but also on shading conditions. Difficulty still exists concerning estimating the local convection coefficients because of the difficulty in determining the local flow pattern of wind around the structure. This difficulty necessitated using global convection coefficients in the numerical model. This model was calibrated against experimental data on a trapezoidal girder that was partially shaded by a nearby building. Based on this calibration with the experimental data, in the following analysis of the guideway, solar reflectivity of 0.12 and emissivity of 0.88 for steel, solar reflectivity of 0.15 for the ground, and convection coefficients of 5.02 and 1.57 will be used.

# CHAPTER 5
# GUIDEWAY STUDY: PART I

The behavior of guideways under the thermal environment in Las Vegas, Nevada was studied using the numerical model. The original Type I steel guideway design by Transrapid was used to compare it with a modular design, which is named the Type IV steel guideway. The guideways were assumed to be made of weathering steels, which are more responsive to solar radiation than conventional steels with reflective coatings, as was indicated by the experimental results in Reference 29. Temperature distributions and thermal deformations of the Type I and Type IV guideways were compared under the single track configuration and characteristic behaviors were identified.

## 5.1 Modular Guideways

Guideways have been shown to have problems regarding their thermal environments [27]. Since violation of deflection criteria of the guideway within many thermal environments can limit the proper operation of Maglev vehicles, there have been a few studies that seek to mitigate thermal problems with new design concepts of guideways [25, 27].

### 5.1.1 Designs for Modular Guideways

Type I guideways are usually fabricated in the shop in a controlled environment to minimize distortions. All units are fabricated with a high level of precision, which makes the guideway expensive. In modular guideway design, the parts that require high precision are separated from the parts that do not require the same precision. The parts that interact with Maglev vehicles are separated since those parts generally require high precision. The track structure in Figure 5.01 needs to be built in such a manner in shops in a controlled environment by automated processes. The remaining parts are called the support structure. The support structure in Figure 5.01 can be built using conventional construction processes for bridges and guideways. The design shown in Figure 5.01 through Figure 5.04 is the adaptation and extension of the design which separates the two components and assembles the components in the field. The length of a track structure is about 6 m while a support structure is a two-span continuous box girder with a span length of 31 m. Ten units of the track structures in Figure 5.02 are installed on a support structure. These structures are installed and adjusted on support structures in the field. Since the size of a track structure is manageable compared to the size of a support structure, it is possible to use automated equipment that moves along the support structure, installs, and fine-positions track structures on the support structures.

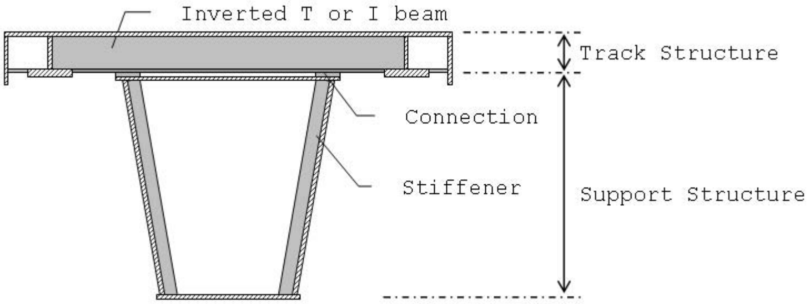

Figure 5.01 Type IV Modular Guideways

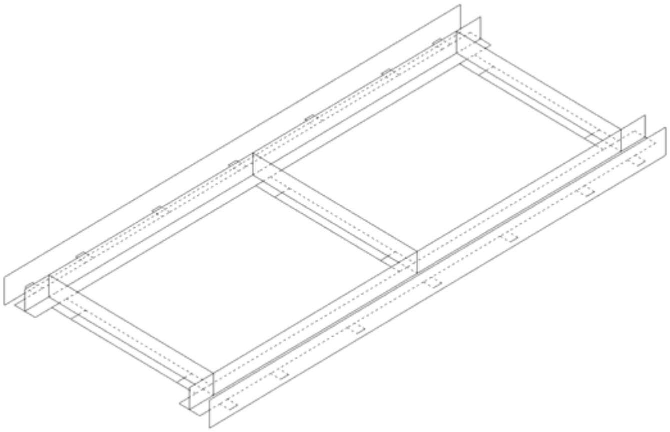

Figure 5.02 Track Structure for Type IV Modular Guideways without Slide Surface

As shown in Figure 5.03 and Figure 5.04, bolted connections with oversize holes and shims between the track structure and the support structure allow final adjustment of the position of the track structure. In addition, if necessary, possible thermal insulation can be achieved by inserting materials with low thermal conductivity to limit the heat transfer from the track structure to the support structure. Thermal expansion can be accommodated by an expansion gap between each track structure. The connection of a track structure to a support structure could be seated above the stiffeners. Stiffeners can be positioned outside of the support structure. However, the acoustic noise produced during the passage of a vehicle may limit the position of stiffeners to the inside of a support structure.

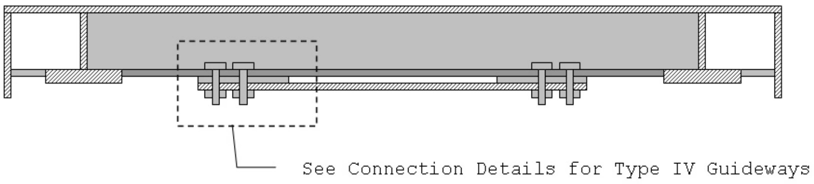

Figure 5.03 Track Structure for Type IV Modular Guideways

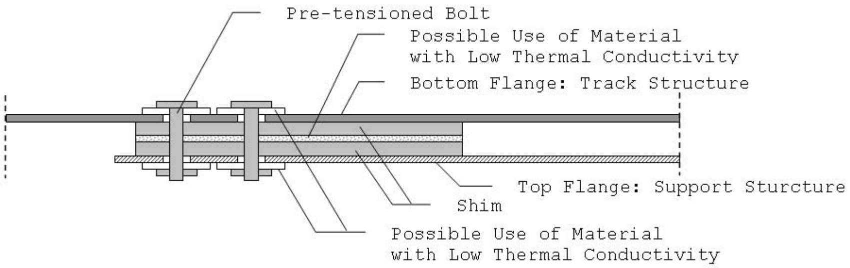

Figure 5.04 Connection Details for Type IV Modular Guideways

The modular design allows for the adjustment of the track structure to accommodate the movement of the foundation or supports after a certain period of time. The design also allows for replacement of a track structure in the case that it needs to be repaired or in the event that a revised Maglev technology is introduced. When a new magnetic suspension system is adopted in the lifespan of the guideway, it is more economical to upgrade the track structure without replacing the whole guideway.

### 5.1.2 Type I and Type IV Guideways

Numerical models of Type I and Type IV guideways are created for simulations under thermal environments. Figure 5.05 shows the shape of a Type I guideway. The slide surface was not drawn so that other parts of the guideway are visible. Figure 5.06 shows the trapezoidal shape of a Type IV guideway support girder with the track structures on top. While surfaces such as the slide surface, guidance rails and stator flanges in the Type I guideway participate in the overall structural response and resist the loads transferred onto them from the vehicle, the track structure in the Type IV guideway primarily acts to transfer the load from the vehicle to the support structure and is not designed to participate in the overall structural response. Since the track structures are discrete from the expansion gaps, they were not relied upon to participate with the support structure in the preliminary design of the structure. As a result, the Type IV guideways require more material to match the required vertical and horizontal stiffness compared to the integral guideways used in the Type I.

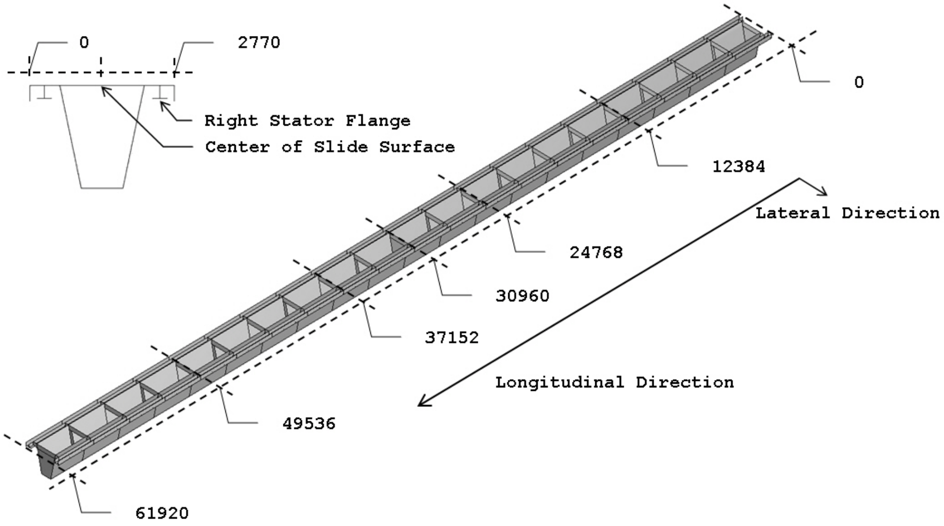

Figure 5.05 Model of Type I Guideway without Slide Surface

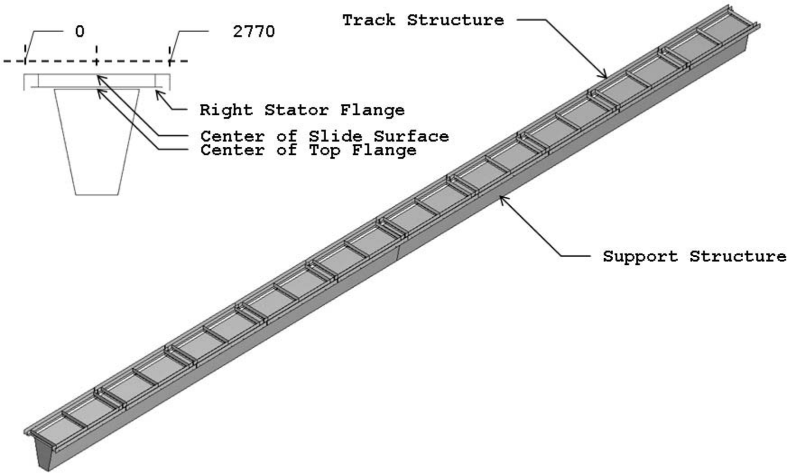

Figure 5.06 Model of Type IV Guideway without Slide Surface

Before the simulation, the Type IV guideway was sized to have similar stiffness in the vertical direction as the Type I guideway. The Type I guideway has a vertical displacement of 7.5 mm under the distributed load of 27.55 kN/m. The Type IV guideway is designed to have a displacement of comparable magnitude in the vertical direction. In order to provide this stiffness, the depth of the support structure was increased to the depth of the Type I guideway. The depth of the Type IV guideway is larger than the Type I guideway by the depth of the track structure. The design criteria other than the vertical deflection have not been verified since the objective is to determine the performance of the Type IV guideways under thermal environments compared to the Type I guideways and to determine if the modular design could mitigate thermal problems.

In the finite element model for Type I guideways, eight node heat transfer quadrilateral shell elements (DS8) are used for heat transfer analysis, and eight node shell elements with reduced integration (S8R) and three node quadratic beam elements (B32) are used for structural analysis. The guideways are represented mainly by the shell elements. The beam elements represented small pieces of steel connecting the guidance rails and the stator flanges at discrete points along the length of the guideway. Since the beam elements were not included in the heat transfer analysis, the temperature field in the beam elements was interpolated in the structural analysis from the temperatures at the nodes on the shell elements, where the beam elements were connected. For Type IV guideways, four node heat transfer quadrilateral shell elements (DS4) and gap conductance comparable to 1 mm thick steel plate between the track structure and the support structure are used for heat transfer analysis, and eight node shell elements with reduced integration (S8R) and three node quadratic beam elements (B32) are used with the temperature field at the mid-side nodes of each element interpolated in the structural analysis. The connection between the track structure and the girder was modeled as fixed by constraining the translational and rotational degrees of freedom in the structural analysis. Material properties of steels that are used in the model are modulus of elasticity of $200 \times 10^9$ N/m$^2$ ($29 \times 10^6$ psi), density of 7850 kg/m$^3$ (490 lb/ft$^3$), Poisson's ratio of 0.30, conductivity of 46.6 W/m·K (26.9 BTU/hr·ft·°F), heat capacity of 475 J/kg·K (0.113 BTU/lb·°F), and expansion coefficient of $11.7 \times 10^{-6}$ m/m·K ($6.5 \times 10^{-6}$ in/in·°F).

## 5.2 Thermal Environment for the Guideway Study

From the TMY2 data set of Las Vegas, Nevada, four days were selected to represent characteristics of the four seasons. These days were March 26, June 25, September 17, and December 17. Those are clear days close to the spring equinox, the summer solstice, the fall equinox, and the winter solstice. The selection of a spring day was done by considering the days a week before and after the spring equinox from the TMY2 data set. The days range from March 15 to March 29. The clear day that had the maximum global horizontal radiation and that is closest to the spring equinox was March 26.

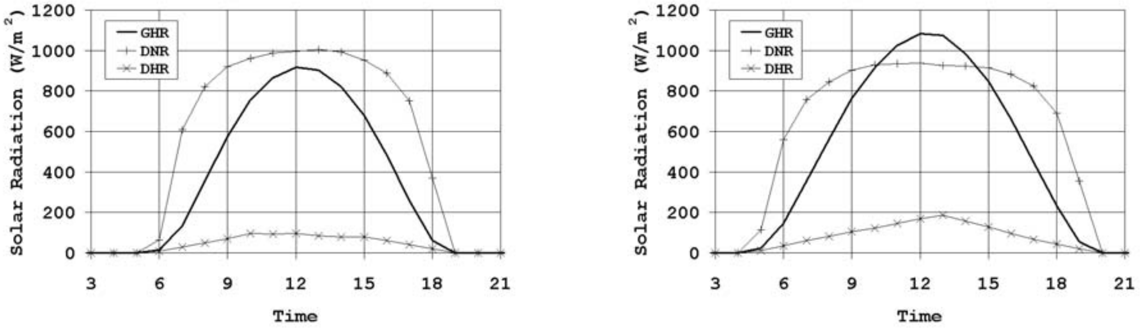

(a) Radiation on March 26

(b) Radiation on June 25

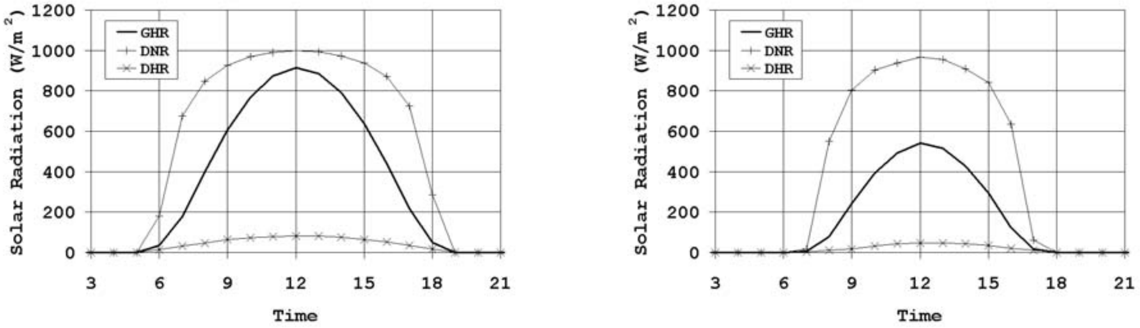

(c) Radiation on September 17

(d) Radiation on December 17

Figure 5.07 Solar Radiation on Selected Days

Solar radiation data of the days are drawn in Figure 5.07, and GHR represents the global horizontal radiation, DNR the direct normal radiation component, and DHR the diffuse horizontal radiation component. The seasons of the year do not make much difference to the direct normal radiation component. The direct normal radiation component on December 17 is just a little higher than that on June 25. The diffuse horizontal radiation is a little higher on June 25 than on December 17. The global horizontal radiation is influenced by the solar position. The global horizontal radiation is higher on June 25 than on the other three days due to the incidence angle of solar rays on the horizontal plane. The radiation components on March 26 are similar to those on September 17 since the solar positions are similar, which results in similar global horizontal radiations. However, as shown in Figure 5.08, the air temperatures were quite different on March 26 and September 17 even though the solar radiation data are similar. Therefore, the four days represent four different boundary conditions.

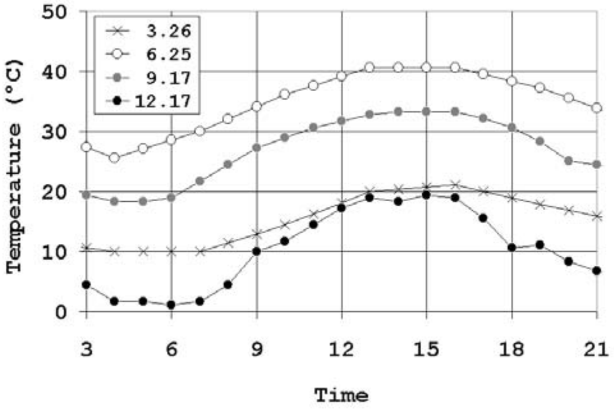

Figure 5.08 Air Temperature on Selected Days

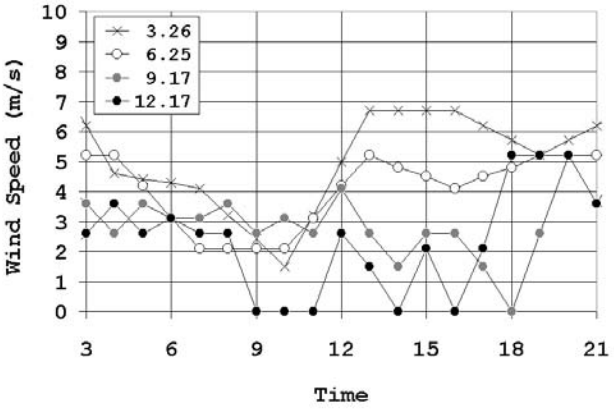

Figure 5.09 Wind Speed on Selected Days

Wind speed data are plotted in Figure 5.09. The high wind speed in the afternoon on March 26 does not generally influence the maximum vertical displacement much since the maximum vertical temperature gradient is more influenced by the conditions before 13:00. However, it is likely that lateral displacement in the afternoon is less than that in the morning because of higher wind speed in the afternoon. It may be necessary to use a lower wind speed for the simulation to produce a more severe thermal environment for the guideways. However, real data from TMY2 are used without assuming any artificial conditions. Even though the lowest wind speeds have been used, the results would not have represented the behavior under extreme conditions since the TMY2 contains, as the name suggests, typical data sets. Therefore, the simulation results are similar to typical behaviors rather than behaviors under extreme conditions, and the results are not intended for use under extreme conditions [30]. The results are used to identify characteristic behaviors and to compare different designs under typical thermal environment, for which the TMY2 data set is generally used.

## 5.3 Analysis with Single Track Guideway: Solo

Single track guideways were analyzed under four thermal environments. The guideway was elevated so that the position of the slide surface was 20 m above the ground. Additional small segments of the guideway were positioned at the ends of the guideway to simulate the shadowing provided by the adjacent guideway and prevent the direct solar radiation at the diaphragms near the end support locations as shown in Figure 5.10. The initial temperature of the guideway was set to the air temperature at 04:00 in the morning. For example, the air temperature of 10°C at 04:00 on March 26 was used as the initial temperature of the guideway in the simulation for the day and the air temperature of 25.6°C at 04:00 on June 25 was used as the initial temperature of the guideway for the simulation under the thermal environment on June 25. The time increment was set to 3600 seconds. Temperature distributions were studied, and deformations of the Type I and the Type IV guideways were compared.

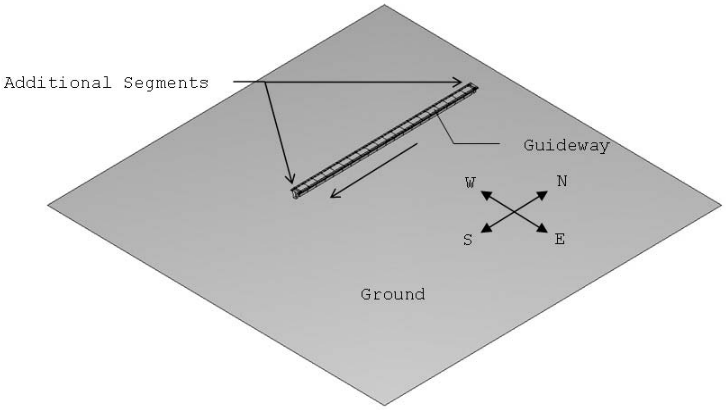

Figure 5.10 Single Track Guideway Configuration

### 5.3.1 Temperatures of Type I Guideways

The Type I guideway temperature profile in the morning of a summer day along the center line of the slide surface in the length direction is shown in Figure 5.11. The guideway is oriented in the north-south direction. The position at 0 mm is on the north end and the position at 61920 mm is on the south end of the guideway. The position at 30960 mm is at the mid-support. The pattern of the temperature profile in Figure 5.11 repeats with a 3096 mm interval. The interval represents the distance between the cross beams that are connected below the slide surface. The cross beam works as a heat sink and lowers the temperature of the slide surface at the 3096 mm interval. The maximum temperature occurs between the cross beams and reaches 68°C at noon on a typical summer day.

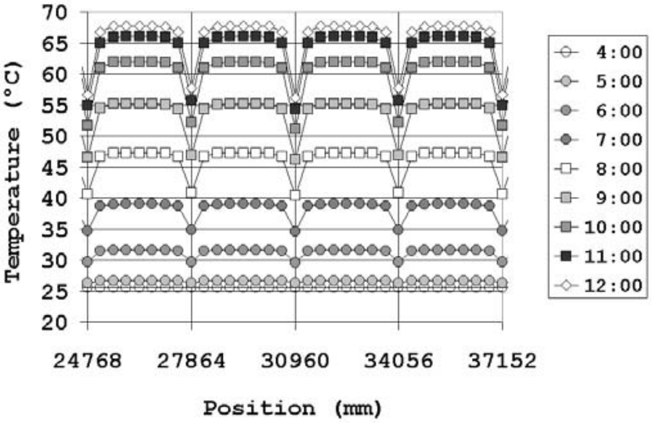

Figure 5.11 Temperature at Slide Surface on June 25: Type I

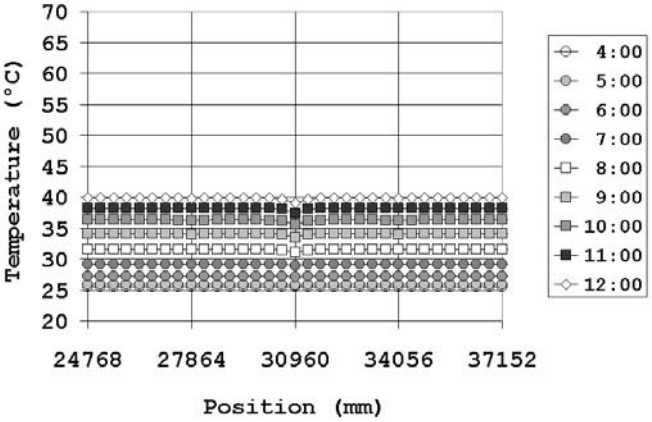

Figure 5.12 Temperature at Bottom Flange on June 25: Type I

In Figure 5.12, the temperature profile along the center line of the bottom flange is shown. Compared to the temperature in the slide surface shown in Figure 5.11, the temperature is lower since the bottom flange is shaded all the time and receives only the reflected radiation from the ground. The temperature differential between the slide surface and the bottom flange causes vertical displacement of the guideway. The temperature is close to the air temperature and reaches 40°C at noon. The position at 30960 mm is where a diaphragm is located. The temperature is a little lower at the location of a diaphragm since the temperature increase in the diaphragm is lagging behind that of other parts.

The temperature profile along the center line of the stator flange is shown in Figure 5.13. The profile is similar to that of the bottom flange since the stator flange is located in the shade under the slide surface. However, the temperature in the stator flange is relatively higher at the cross beam locations because heat is transferred from the slide surface to the stator flanges through the cross beams. The temperature in the stator flange on the west side is not much different from that on the east side.

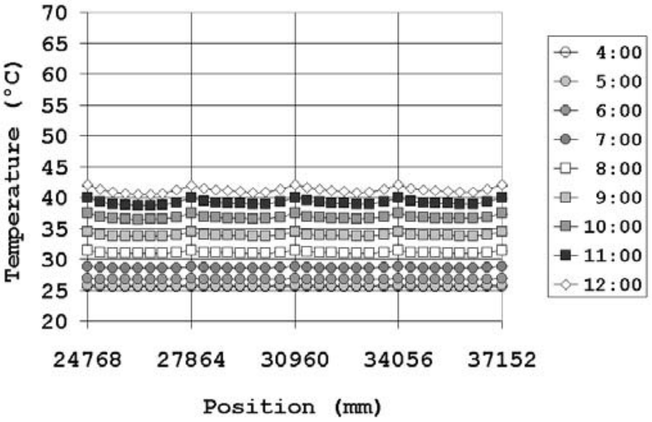

Figure 5.13 Temperature at Stator Flange on East Side on June 25: Type I

The temperature distribution across this section of the slide surface is shown in Figure 5.14. The section is located 51084 mm from the north end of the guideway and is one of those with a maximum temperature occurring between the cross beams. The temperature is not uniform along the width of the slide surface and is not symmetric. The temperature on the right side is higher than that on the left side in the morning, and this tendency is reversed in the afternoon due to the position of the sun. In Figure 5.14, the left end is facing west while the right end is facing east. In the summer, the sun rises from the northeast and sets in the northwest position. The east facing surface is exposed to the morning sun while the west facing surface is exposed to the afternoon sun.

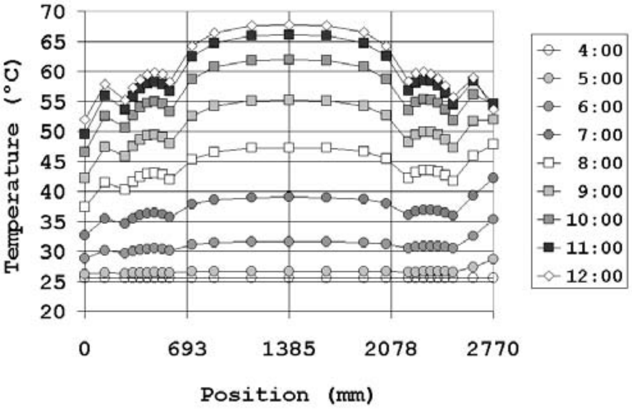

(a) Temperature in the Morning

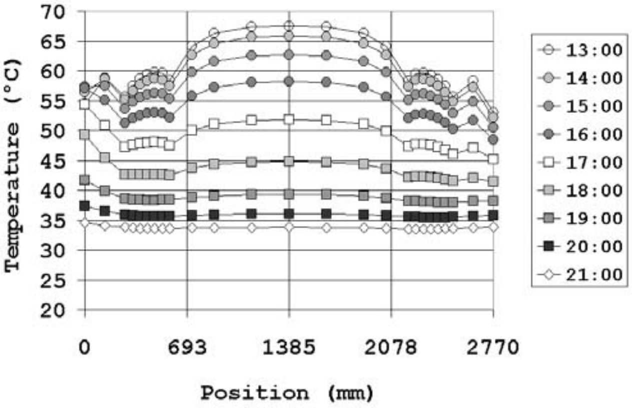

(b) Temperature in the Afternoon

Figure 5.14 Temperature at Slide Surface Section on June 25: Type I, N-S

This unsymmetrical temperature profile is more pronounced during the winter when the position of the sun is more inclined. As a result, more radiation is on the side surfaces of the guideways. This effect is shown by the temperature distribution in Figure 5.15 for a guideway oriented in the northeast to southwest direction. In the figure, the left end is facing northwest and the right end is facing southeast. The temperature on the right end is higher than that on the left end in the morning as well as in the afternoon due to the path of the sun during the winter and the orientation of the guideway. Even though the temperature is not as high as the temperature during the summer in Figure 5.14, the temperature difference between the left and the right ends of the slide surface is more pronounced.

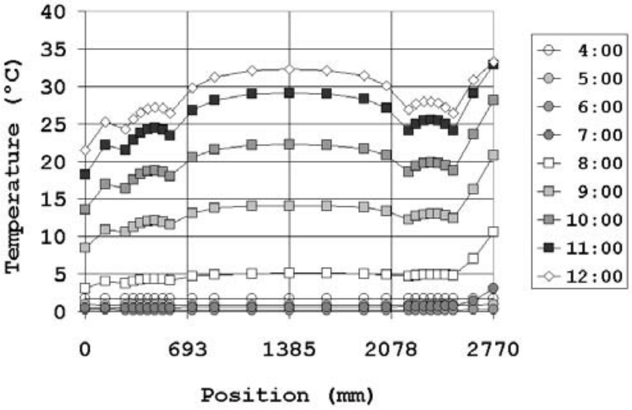

(a) Temperature in the Morning

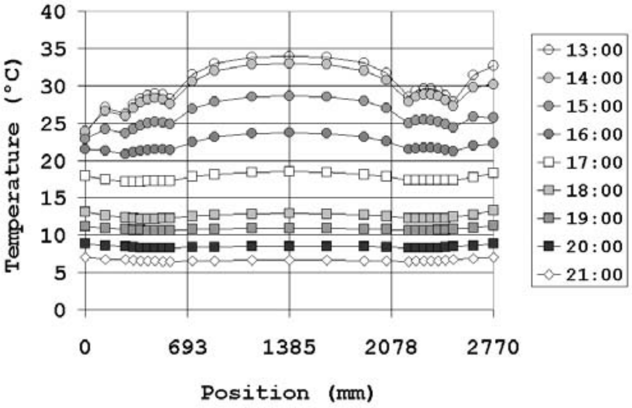

(b) Temperature in the Afternoon

Figure 5.15 Temperature at Slide Surface Section on Dec. 17: Type I, NE-SW

### 5.3.2 Deformations of Type I Guideways

Typical patterns of the deformation during the summer are shown in Figure 5.16 and Figure 5.17 for the Type I guideway oriented in the north-south direction. The initial configuration and the deformed configuration are superimposed, and the lateral and vertical displacements are magnified by 1000 to make the deformed shape more visible. At 06:00 in the morning, heat flux on the east side increases temperature on the east web and bends the guideway in the lateral direction as shown in Figure 5.16. The vertical displacement of the guideway at noon is shown in Figure 5.17, in which the lateral displacements are small compared to the vertical displacements.

Figure 5.16 Deformation at 06:00 on June 25: Type I

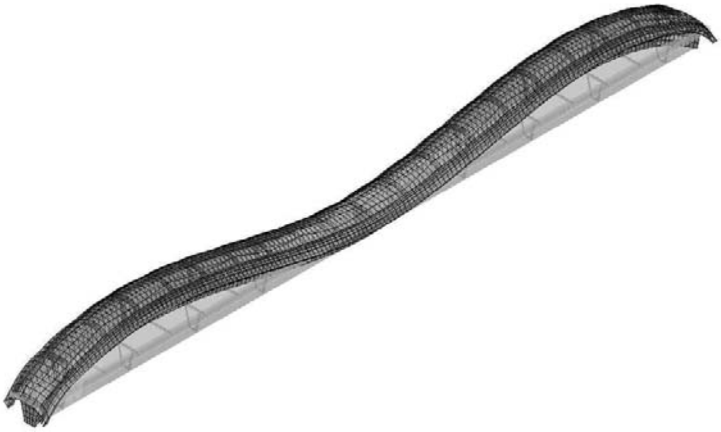

Figure 5.17 Deformation at 12:00 on June 25: Type I

The effect of the orientation of the guideway along with the effect of the season on the behavior of the guideway is summarized in the following figures. The figure labels represent the angles between the guideway and the east direction with clockwise being positive. '000' means that the guideway is oriented in the west to east direction. '045' means that the guideway is oriented in the northwest to southeast direction. '090' is for the guideway running in the north to south direction. '135' is used if the guideway lies in the northeast to southwest direction. As shown in Figure 5.18, these configurations cover the guideways oriented at a 45° increment.

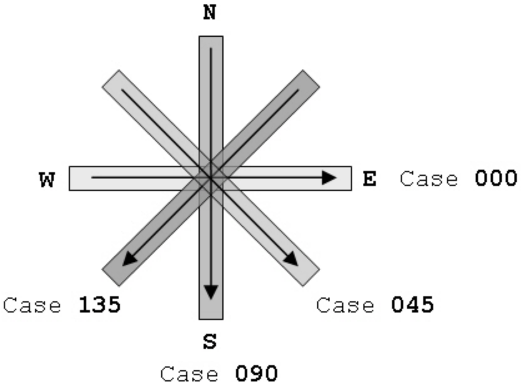

Figure 5.18 Guideway Orientation

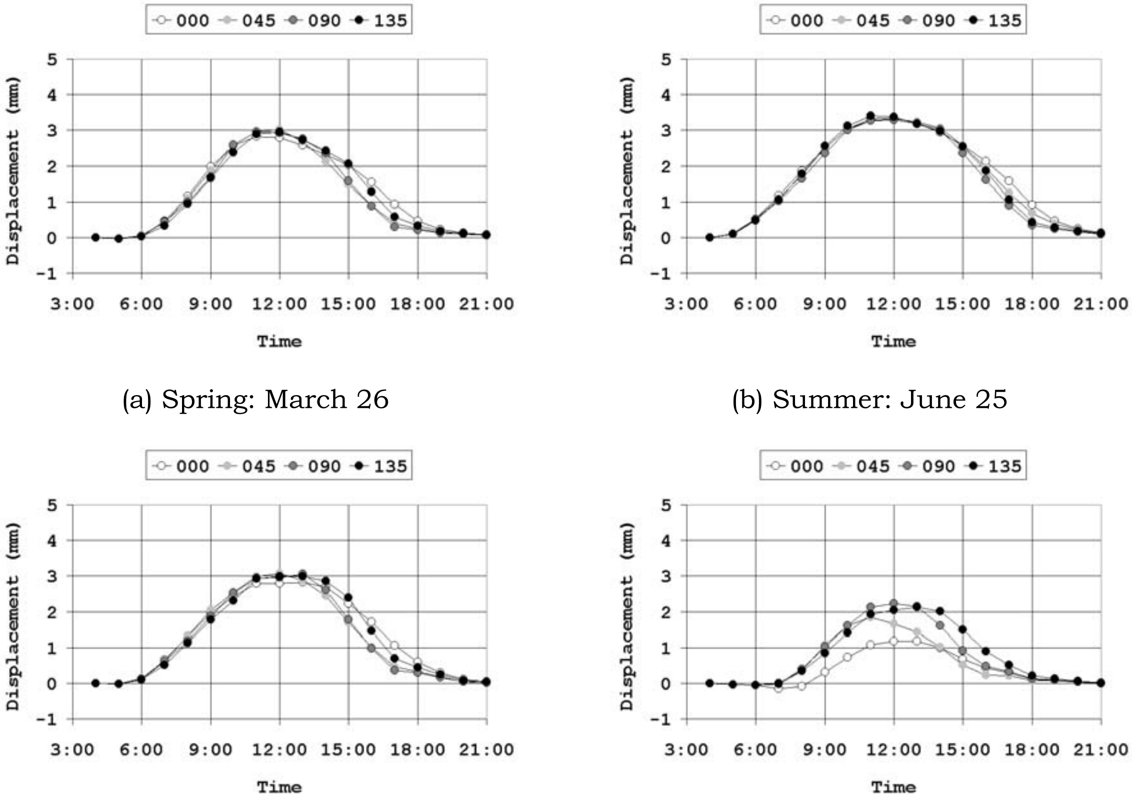

(a) Spring: March 26

(b) Summer: June 25

(c) Fall: September 17

(d) Winter: December 17

Figure 5.19 Vertical Displacements at Stator Flange: Type I

#### 5.3.2.1 Lateral and Vertical Displacements on the Stator Flange

Since the vehicle interacts with stator packs that are installed on the stator flanges, the deformation of the stator flange is important. Vertical displacements at the right stator flange of the guideway in Figure 5.05 are plotted in Figure 5.19. The location is 10.8 m away from the end of the guideway, and this is where the maximum vertical displacement occurred in the stator flange. The orientation of the guideway on the horizontal plane does not seem to have much influence on the vertical displacement. During the summer, the vertical displacement is the largest due to the high intensity of solar radiation on the slide surface at noon. Typical summer condition causes up to 3.5 mm vertical displacement in the stator flange.

The orientation of the guideway significantly influences the lateral displacement. The lateral displacements at the same location where the vertical displacements were evaluated are shown in Figure 5.20. During the spring, the lateral displacement is at its maximum at around noon for the guideway in the east-west direction (000). Since the south surface of the guideway is under direct solar radiation while the north surface of the guideway is under shade most of the time, the lateral displacement is to the south direction. The magnitude of the lateral displacement is smaller than other orientations because the incidence angle between the solar rays and the guideway's south surface is relatively small at noon. When the guideway is in the northwest to southeast direction (045), surfaces on the west side get exposed to solar radiation longer than the surfaces on the east side. Therefore, more lateral displacement occurs in the afternoon than in the morning. When the guideway is in the north-south direction (090), the lateral displacement is at a maximum. This displacement occurs both in the morning and in the afternoon. The displacement in the afternoon is slightly lower than in the morning due to the higher wind speed shown in Figure 5.09. The displacement pattern during the fall is similar to that during the spring.

Under summer conditions, lateral displacements show a slightly different pattern when the guideway is oriented in the east-west direction (000). The displacement around noon is opposite to the displacement in the early morning and in the late afternoon. This difference appears because the sun rises from the northeast, moves to the south, and sets in the northwest. Therefore, surfaces on the north side heat up in the early morning and in the later afternoon.

The effect of the guideway's orientation is more pronounced during the winter due to the lower solar position which increases the angle of incidence along the sides of the guideway. Guideways running in the northwest to southeast direction (045) and the northeast to southwest direction (135) experience the solar radiation mostly on surfaces facing south since the sun rises from the southeast and sets in the southwest. The largest lateral displacements occur during the winter.

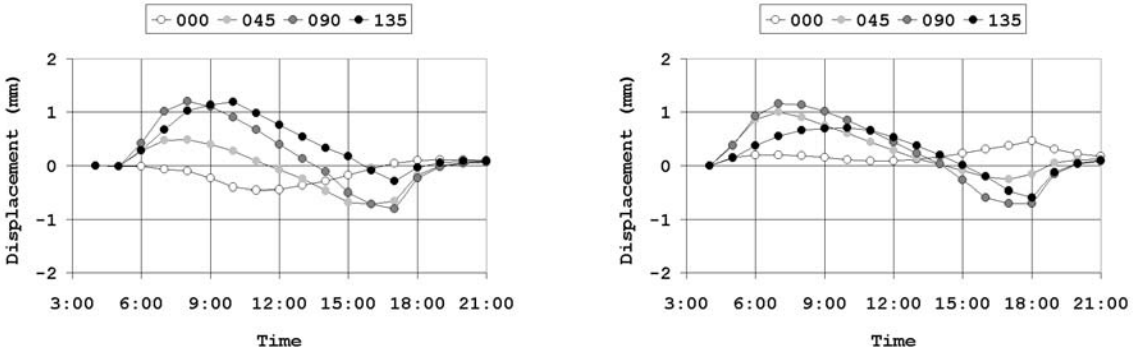

(a) Spring: March 26

(b) Summer: June 25

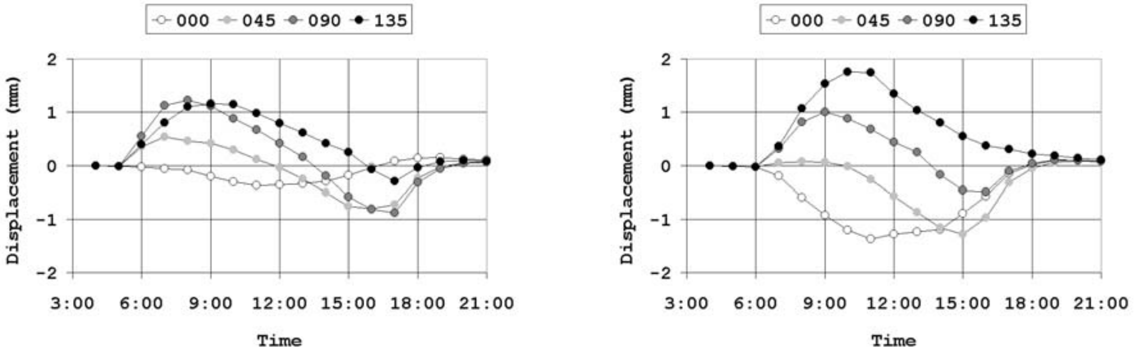

(c) Fall: September 17

(d) Winter: December 17

Figure 5.20 Lateral Displacements at Slide Surface: Type I

The vertical displacements and the lateral displacements are summarized in the plots of lateral-vertical displacements in Figure 5.21. Points on the stator flange move more in the vertical direction than in the lateral direction. The lateral-vertical displacement pattern of the guideway oriented in the east-west direction is different from those that occur in other orientations. The lateral displacement pattern is more influenced by the guideway orientation while the maximum vertical displacement is not influenced much by it. The lateral-vertical displacements that occur during the spring are very similar to those during the fall.

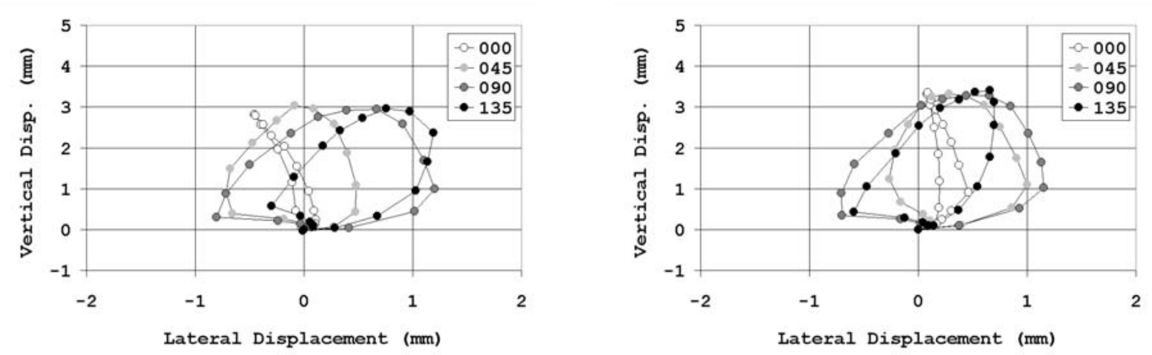

(a) Spring: March 26

(b) Summer: June 25

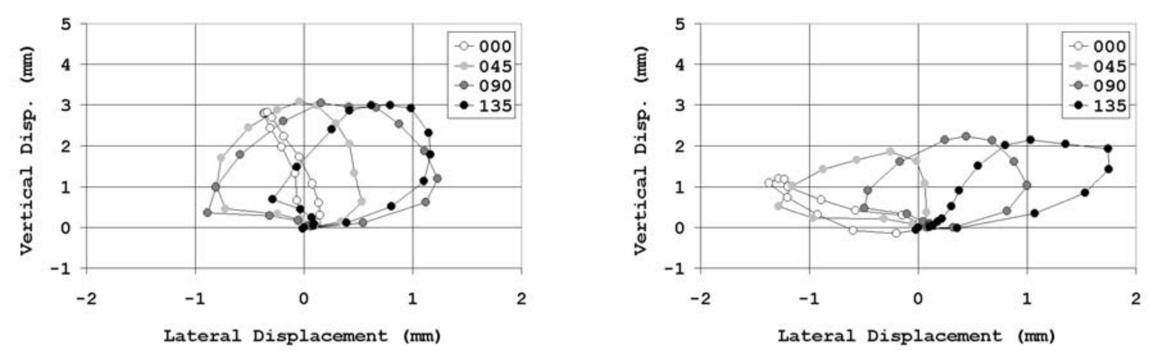

(c) Fall: September 17

(d) Winter: December 17

Figure 5.21 Lateral-Vertical Disps. at Stator Flange: Type I

### 5.3.2.2 Seasonal Displacements on the Stator Flange

The seasonal displacements are plotted for guideways in the north-south direction in Figure 5.22. The difference between the vertical displacement during the summer and that during the winter is associated with the incidence angle of solar rays on the top surface. The maximum vertical displacement generally occurs around noon. For the lateral displacement, as the sun rises in the morning, it heats up the east side, and when the sun sets, it heats up the west side. This difference causes the displacement pattern to be asymmetrical. Since the displacements are at a location 10.8 m away from the end of the guideway, the longitudinal displacement at the end is expected to be about 50% more. The lateral-vertical displacement envelope reveals an oval shape with a larger shape during the summer and a smaller shape during the winter.

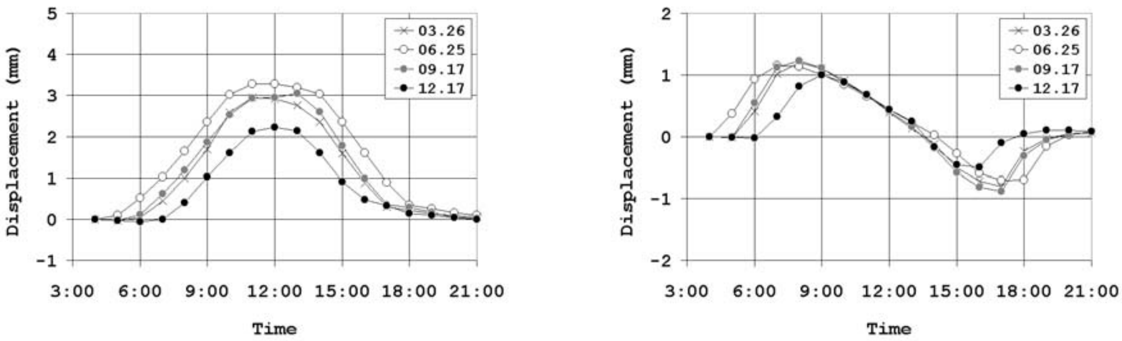

(a) Vertical Displacement (b) Lateral Displacement

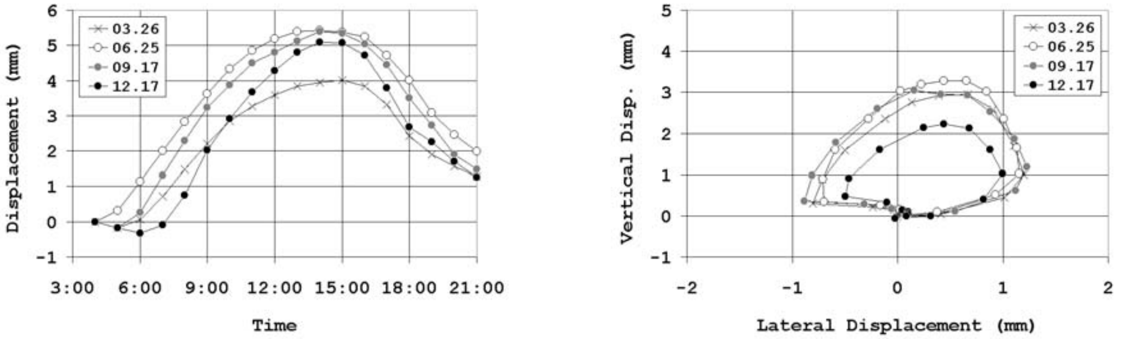

(c) Longitudinal Displacement (d) Lateral-Vertical Displacement

Figure 5.22 Seasonal Displacements at Stator Flange: Type I

5.3.2.3 Displacements on the Stator Flange at the End of Guideways

The lateral-vertical displacements at the end of the stator flange are shown in Figure 5.23. The displacements are small due to the proximity of the end support. The displacements for other times of the year show similar behavior.

The longitudinal displacements for the guideway in the north-south direction are shown in Figure 5.24. The position is at the end of the stator flange, and the longitudinal displacement of 8.4 mm at 14:00 is the maximum displacement on a typical summer day. However, the longitudinal displacement in the figure is only the differential displacement under the assumption that there is no displacement at 4:00. The actual displacement is dependent on the guideway’s installation temperature and can be calculated by considering the installation temperature and the difference between it and the initial temperature. The air temperature of 25.6°C at 04:00 on June 25 was used as the initial temperature of the guideway for the simulation on June 25.

Assuming the installation temperature of the guideway is 25.6°C, the maximum longitudinal expansion is about 8.4 mm on a typical summer day. If the temperature of the guideway is 15.0°C during installation, additional expansion due to the uniform temperature increase of 10.6°C is estimated to be 3.8 mm. Therefore, the total thermal expansion would be 12.2 mm.

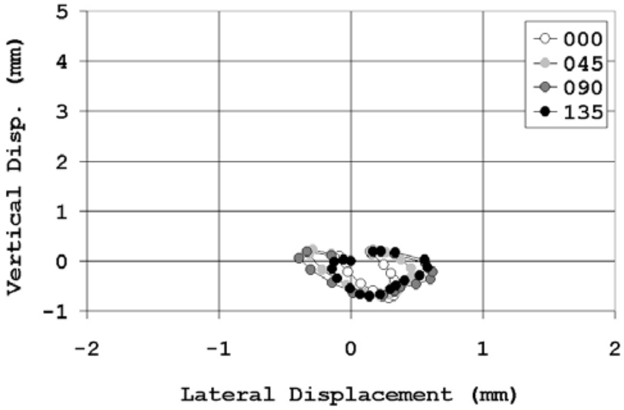

Figure 5.23 Lateral-Vertical Disps. at Stator Flange End on June 25: Type I

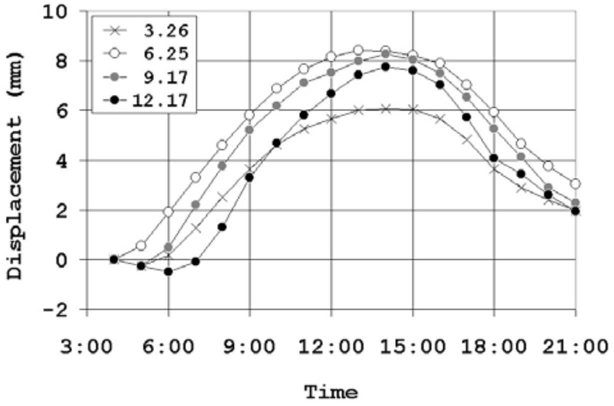

Figure 5.24 Longitudinal Displacements at Stator Flange End: Type I, N-S

The longitudinal displacement is not influenced much by the orientation of the guideway as shown in Figure 5.25. The maximum displacement is reached around 14:00. The pattern of the longitudinal displacement is similar to that of the air temperature. The longitudinal displacements on December 17 are pronounced because the change in the air temperature was more than on other days.

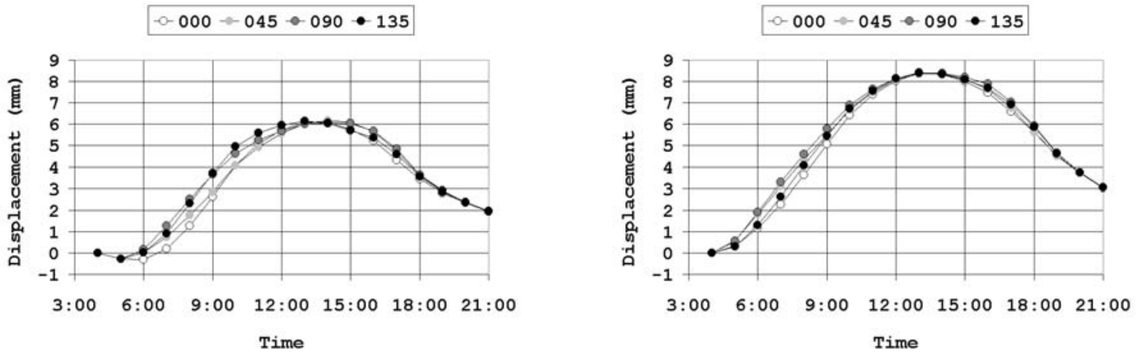

(a) Spring: March 26

(b) Summer: June 25

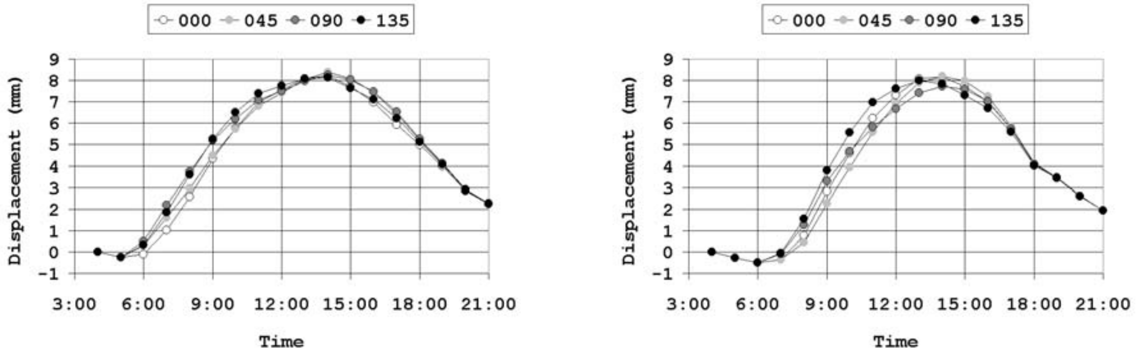

(c) Fall: September 17

(d) Winter: December 17

Figure 5.25 Longitudinal Displacements at Stator Flange End: Type I

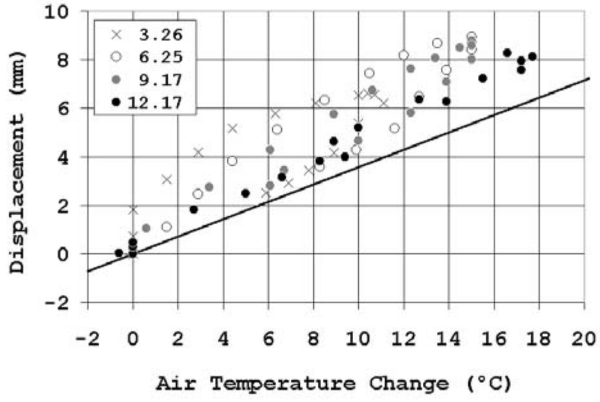

Figure 5.26 Expansion Estimates at Stator Flange End: Type I

In Figure 5.26, the differential air temperature, which is the difference between the initial air temperature and the current air temperature, is plotted against the longitudinal displacement. The longitudinal displacements were calculated in reference to the initial configuration of the guideway, where the initial temperature was assumed to be 1.5°C lower than the air temperature at 4:00. The solid line represents the displacements based on the formula for thermal expansion, which is $\alpha\Delta TL$. The actual temperature in the guideway is higher than the air temperature. This difference results in higher thermal expansion than the expansion that is predicted using the formula. The thermal expansion is expected to be more when the effect of the heating in the stator packs, which is due to the interaction with the Maglev vehicle, is considered.

### 5.3.3 Temperatures of Type IV Guideways

The temperature profile shown in Figure 5.27 for the Type IV guideway in the north-south direction is similar to that shown in Figure 5.11 for the Type I guideway. The cross beams transfer heat to other areas and act as a heat sink. There are three cross beams for each track structure, and these are seated on top of the top flange of the support structures. Therefore, some of the heat in the cross beam is also transferred to the top surface of the support structure, and the temperature along the top flange of the support structure is higher in positions where the connection to the track structure is close. This occurrence is reflected in the temperature peak shown in Figure 5.28-(a). The temperature profile on the bottom flange is uniform and similar to that of the Type I guideway.

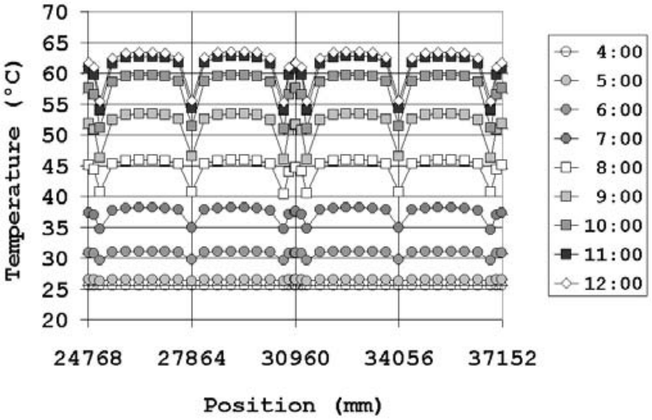

Figure 5.27 Temperature at Slide Surface on June 25: Type IV

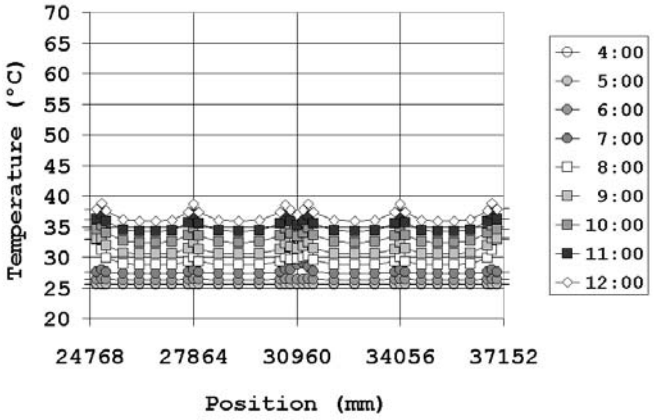

(a) Temperature on Top Flange

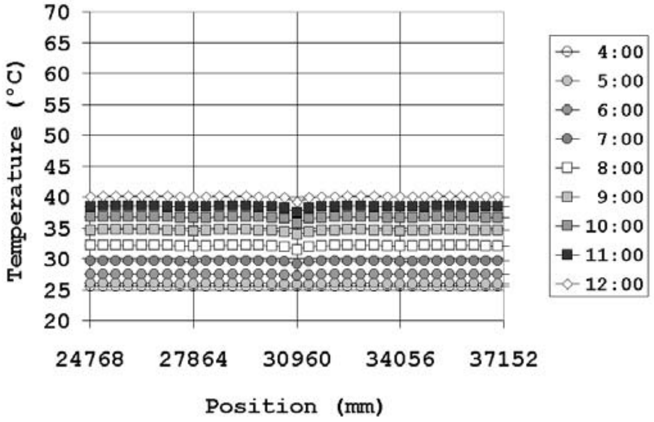

(b) Temperature on Bottom Flange

Figure 5.28 Temperature at Top and Bottom Flanges on June 25: Type IV

The temperature across the slide surface at 51454 mm from the north end of the Type IV guideway is shown in Figure 5.29. The heat flux on the east surface in the morning occurs through the guidance rail. In the Type I guideway, heat is transferred from the slide surface to the web. Since the web is not directly connected to the track structure in the Type IV guideway, the influence of the web on the slide surface as a heat sink is not visible in this plot. The temperature profile is smoother than that of the Type I guideway.

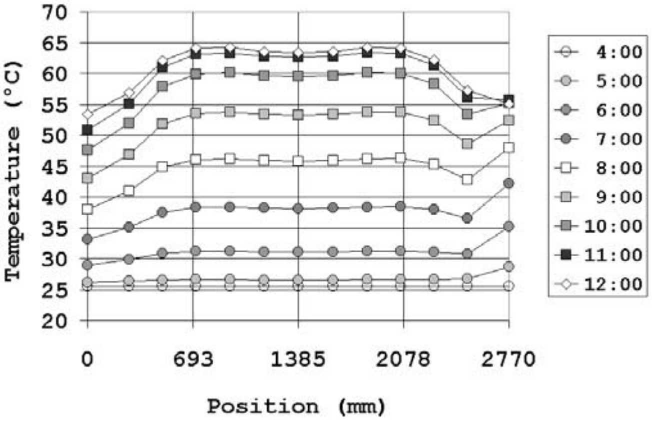

(a) Temperature in the Morning

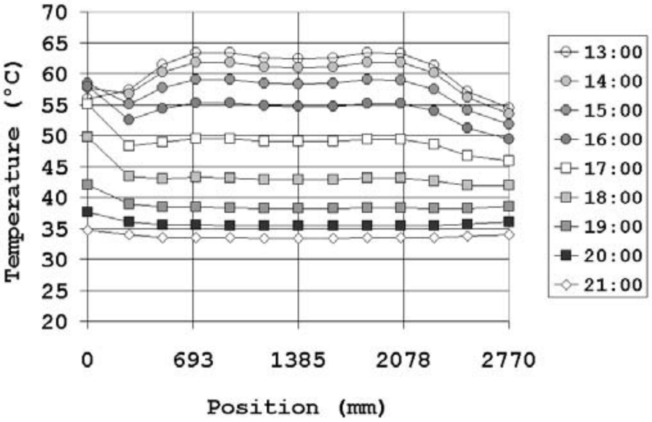

(b) Temperature in the Afternoon

Figure 5.29 Temperature at Slide Surface Section on June 25: Type IV

### 5.3.4 Deformations of Type IV Guideways

The behavior of guideways running in the north-south direction during the summer is shown in Figure 5.30 and Figure 5.31. These figures are comparable to Figure 5.16 and Figure 5.17, respectively. The deformed shape at 06:00 is similar to that of the Type I guideway. However, the deformed shape at 12:00 is significantly different. The displacements in the Type IV guideway are composed of the displacements due to the deformation of the support structure and the displacements due to the deformation of the track structures. The deformed shape of the Type I guideway is not as noticeable in the Type IV guideway since most of thermal deformation occurs in the track structures, while the thermal deformation in the support structure is effectively reduced by the shade under the track structure.

Figure 5.30 Deformation at 06:00 on June 25: Type IV

Figure 5.31 Deformation at 12:00 on June 25: Type IV

The deformation of the cross section of the Type I guideway is shown in Figure 5.32, and that of the Type IV guideway is drawn in Figure 5.33. The Type I guideway moves laterally with a slight rotation at 08:00, and moves vertically to the configuration at 12:00. The lateral expansion on the slide surface results in a slight bending in the web plates. The deformation of the Type IV guideway is different at 08:00. The support structure moved downward while also moving laterally. The distortion in the cross section affects the total displacement, and the distortion on the slide surface of the Type IV guideway appears to be comparable to that of the Type I guideway.

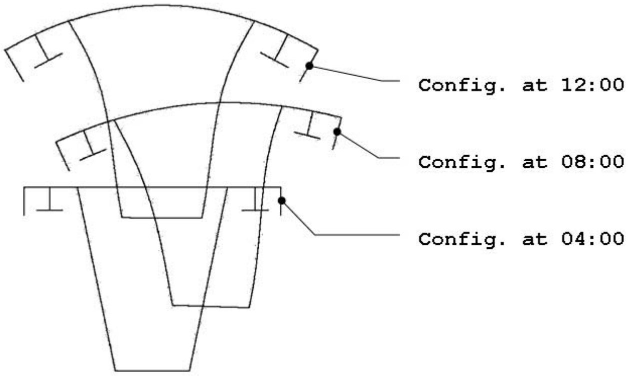

Figure 5.32 Sectional Deformation on June 25: Type I

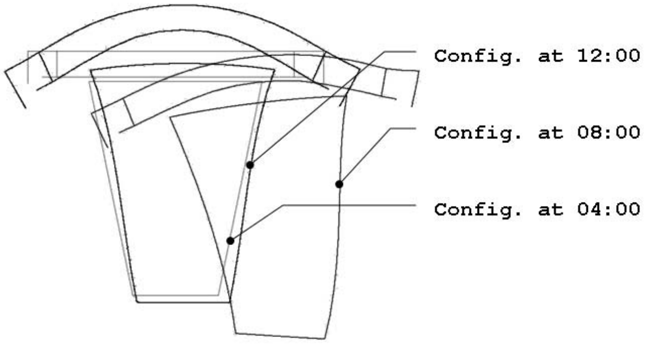

Figure 5.33 Sectional Deformation on June 25: Type IV

The vertical displacement on the slide surface is apparently reduced for the Type IV guideway as shown in Figure 5.34. However, the lateral displacement in Figure 5.35 is greater for the Type IV guideways under the assumed configuration. The position is at the center of the cross section of the slide surface and is at 11.9 m away from the south end for Type I, while the position is at 13.5 m away from the end for the Type IV guideway. The maximum upward displacement on the slide surface generally occurs between cross beam locations, while the maximum downward displacement occurs at the ends of track structures. The slide surface of the Type IV had additional distortion in the cross section in addition to the global displacement, which resulted in more displacement in the vertical direction than the stator flanges. In Figure 5.36, the vertical displacement of the slide surface is significantly reduced, while the lateral displacement is increased.

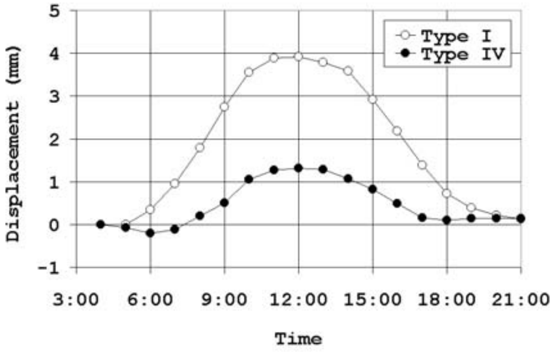

Figure 5.34 Vertical Displacements at Slide Surface on June 25: Type I & IV

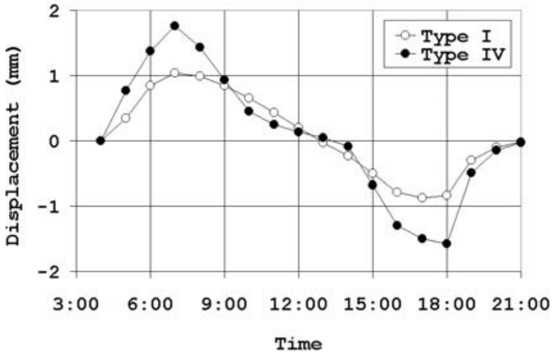

Figure 5.35 Lateral Displacements at Slide Surface on June 25: Type I & IV

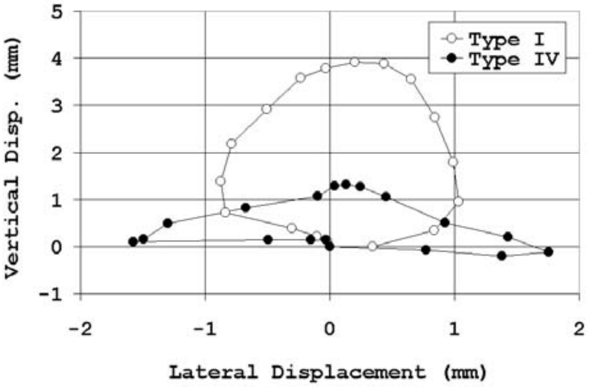

Figure 5.36 Lateral-Vertical Disps. at Slide Surface on June 25: Types I & IV

The effect is more pronounced for the displacement on the stator flanges. In Figure 5.37, the vertical displacements in the stator flanges are compared. The position is at 10.8 m away from the end for the Type I guideway and at 14.2 m away from the end for the Type IV guideway. Compared to the lateral and vertical displacement on the slide surface, the displacement on the stator flange is less in the vertical direction and slightly more in the lateral direction. The maximum and minimum vertical displacement envelopes of the stator flange on the right side of the guideway are plotted as well. As shown in the figure, the stator flange in the Type IV guideways can deflect downward. This outcome is somewhat contrary to the initial thought that the overall structure would move upward. The support structure is under the reflected radiation on the bottom surfaces while the radiation on the top surfaces is blocked by the track structure. The heat transfer through the connection is smaller than the heat flux on the bottom flange. The top flange of the support structure is shaded by the track structure, but some of the heat is transferred from the track structure. The bottom flange of the support structure is not exposed to any direct solar radiation, but is instead under reflected radiation from the ground. If the reflected radiation source is stronger than the heat transferred from the track structure, the temperature on the bottom flange is greater than the temperature on the top. As a result, the support structure bows down. In addition to the movement of the support structure, the track structure undergoes deformation due to the heat flux on the slide surface and the guidance plates. This flux causes additional movement of the stator flange upward or downward. Therefore, in the Type IV guideway, the vertical displacement on the track structure can be reduced by the vertical displacement on the support structure in the opposite direction. As a result, the vertical displacement of the Type IV guideway is very small as compared to that of the Type I guideway.

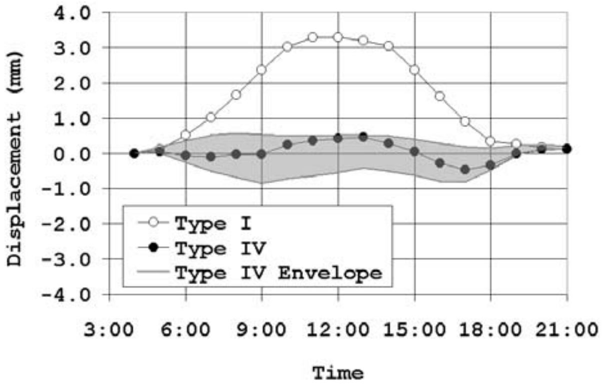

Figure 5.37 Vertical Displacements at Stator Flange on June 25: Type I & IV

The lateral displacement is higher for the Type IV guideways as shown in Figure 5.38 and Figure 5.39. The displacement pattern of a stator flange in these guideways is similar to the displacement pattern of a slide surface. In Figure 5.39, the vertical displacement of the stator flange is significantly reduced while the lateral displacement is increased.

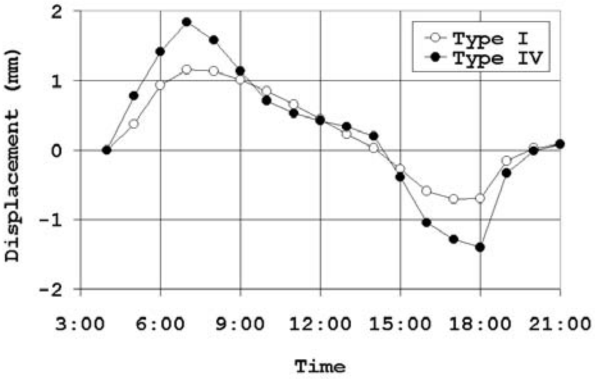

Figure 5.38 Lateral Displacements at Stator Flange on June 25: Type I & IV

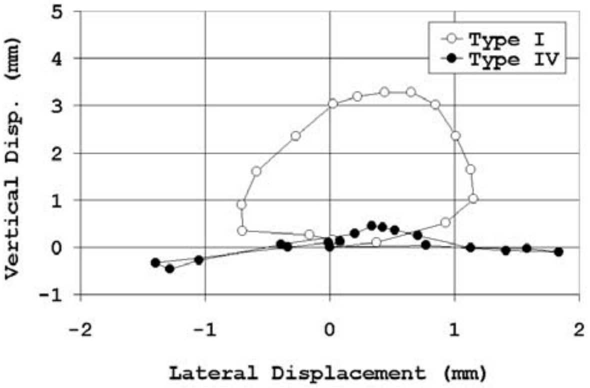

Figure 5.39 Lateral-Vertical Disps. at Stator Flange on June 25: Type I & IV

For the end position, there is not much difference in lateral and vertical displacement between Type I and Type IV guideways as shown in Figure 5.40, and the displacements are small, which is due to the fact that the position is close to the end supports of the guideways. Since the track structure is installed on top of the support structure, the longitudinal displacement in the stator flanges of the Type IV guideway is the sum of the displacement of the support structure and the displacement of the track structure. Thus the Longitudinal movement of the Type IV guideway is reduced as shown in Figure 5.41 because the support structure is in a cooler environment due to the shade from the track structure.

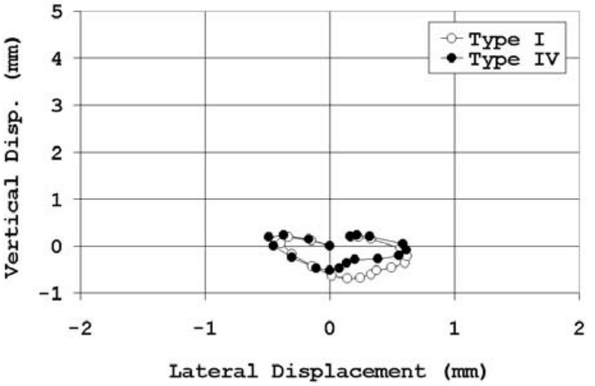

Figure 5.40 Lateral-Vertical Disps. at Stator Flange End on June 25: Type I & IV

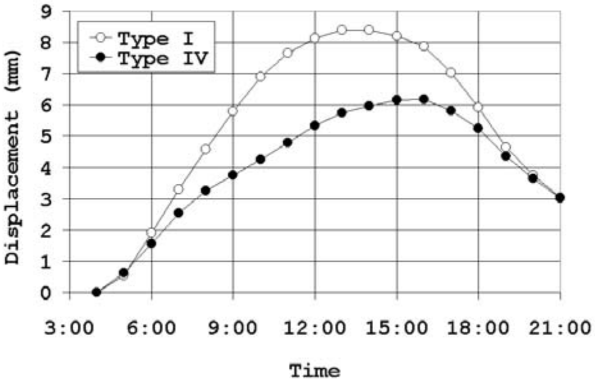

Figure 5.41 Longitudinal Disps. at Stator Flange End on June 25: Type I & IV

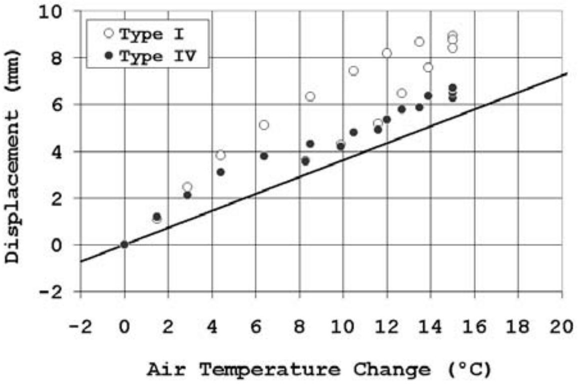

Figure 5.42 Expansion Estimates at Stator Flange End on June 25: Type I & IV

Compared to the Type I guideway, the Type IV guideway's longitudinal displacement is close to the calculated expansion using air temperature differentials as shown in Figure 5.42 since the shade causes the support structure to be influenced less by the solar radiation and more by the air temperature in its longitudinal expansion. The longitudinal displacement of the Type IV guideway is very close to the line that is based on the free expansion predicted by calculations using the air temperature.

The vertical displacements of the stator flanges of Type I and Type IV guideways at 11:00 are plotted along the length of the guideway in Figure 5.43. As noted before, the magnitude of the vertical displacements is very small for Type IV guideways as compared to Type I guideways. The vertical displacement limit recommended for a two-span guideway under thermal loads is 3.9 mm for upward movement [40]. The typical displacements are within these limits. However, the applicability of vertical displacement limits in this specification is not warranted for Type IV guideways since the geometry of the later design deviates from the conventional shape of the guideways, and it is necessary to examine end rotations as stated in Reference 27 .

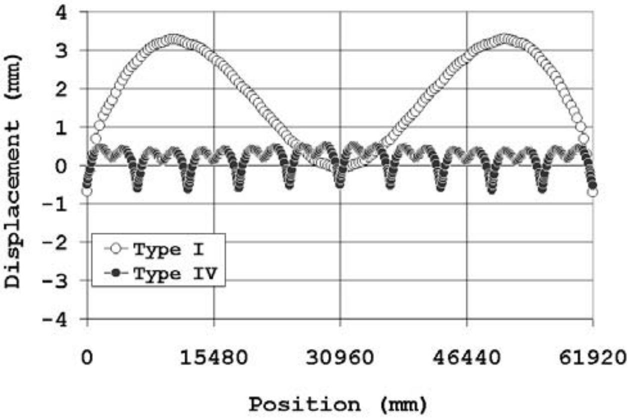

Figure 5.43 Vertical Displacements at Stator Flange at 11:00: Type I & IV

The rotation of the stator flange compares favorably to the rotation predicted by the elastic beam theory except at the end as shown in Figure 5.44. In Figure 5.45, the rotation along the center line of the slide surface and the rotation along the center line of the web on the east side are plotted along with the rotation of the stator flange on the east side. The rotation of the web is similar to the curve that represents the beam theory. The rotation of the stator flange near the end support is significant compared to other rotations.

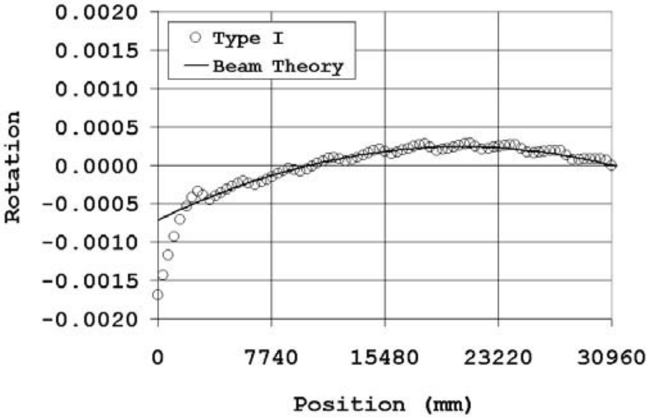

Figure 5.44 End Rotation at Stator Flange at 11:00: Type I

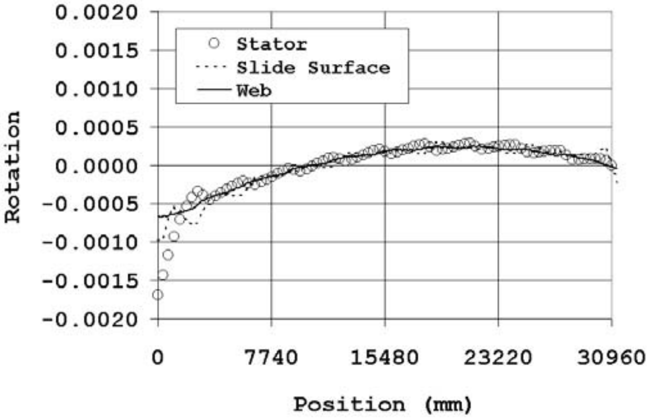

Figure 5.45 End Rotations at 11:00: Type I

As shown in Figure 5.46 and Figure 5.47, the rotations at the ends of stator flanges in the track structure of the Type IV guideway are comparable to that of the Type I. The end rotations are slightly smaller than the end rotations of the Type I. Maximum end rotations on the simulated day are 0.00168 rad for Type I guideways and 0.00135 rad for Type IV guideways. If applying the beam theory on a two-span guideway of a 31m span length, the 3.9 mm upward displacement limit in the specification implies the end rotation limit of 0.00085 rad. The end rotations of both Type I and Type IV guideways are higher than this end rotation limit. This result is due to the distortion of the stator flange at the end for the Type I guideway. Since the criteria in the specifications seem to be based upon the elastic beam theory, it is not clear whether the distortion at the end can be disregarded. Local distortions at the end of the stator flange may not have been properly taken into account in these specifications.

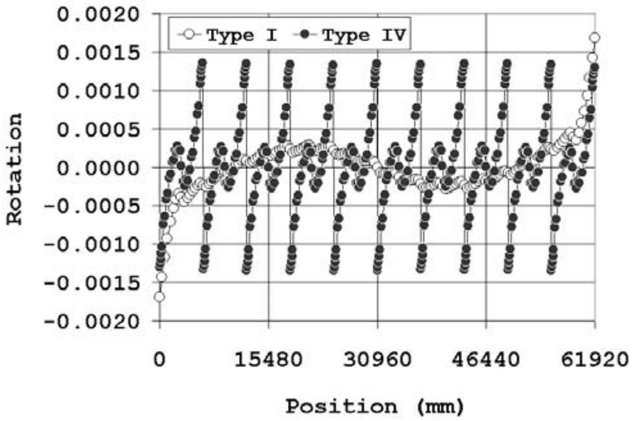

Figure 5.46 Rotations at Stator Flange at 11:00: Type I & IV

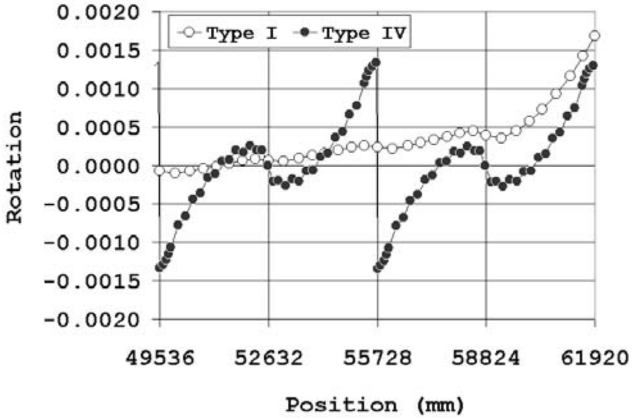

Figure 5.47 End Rotations at Stator Flange at 11:00: Type I & IV

# CHAPTER 6
# GUIDEWAY STUDY: PART II

The studies on the single track guideways are extended to the studies on the double track guideways under the effect of shading due to other parallel guideways and other nearby structures. Even though the use of two-span guideways is better than the use of single-span guideways from the perspective of thermal deformation, this advantage is reduced when partial shade is cast on two-span guideways [27]. This partial shading condition is studied for Type I and IV guideways under the double track guideway configuration.

## 6.1 Effect of Shading due to Another Guideway: Duo

The configuration for the simulation on double track guideways is shown in Figure 6.01. Parallel guideways are represented by surfaces of an equal depth as the original guideway. The surface properties of the parallel guideways are set to the same properties as the surface of the original guideway.

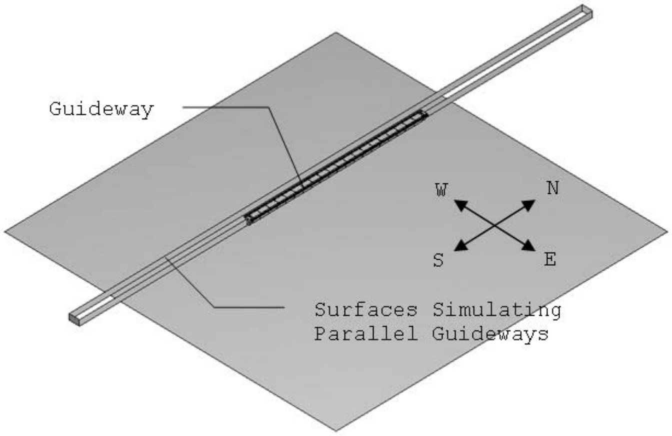

Figure 6.01 Double Track Guideway Configuration

Compared to the single track guideway, guideways in the double track guideway configuration exhibit a similar deformation pattern under similar thermal environments except for the time during which one track shades another. This comparison is made in Figure 6.02 for lateral-vertical displacement on the slide surface during the summer. This Type I guideway is in the north-south direction. When there is no shade due to another guideway, the behavior is the same as a single guideway. The differences only occur in the early morning or in the late afternoon when the solar rays are blocked by the other parallel guideways. The effect on the guideway is minor. The displacements on the stator flange shown in Figure 6.03 also indicate the effect of shading on the sides that face west in the afternoon. The Type IV guideway behaves in a similar way as shown in Figure 6.04.

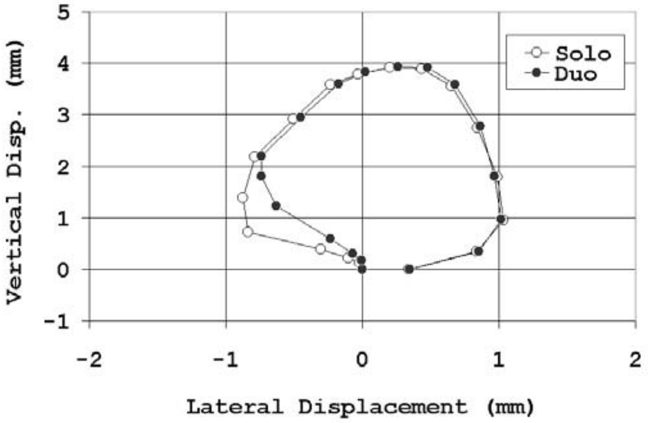

Figure 6.02 Lateral-Vertical Disps. at Slide Surface on June 25: Type I

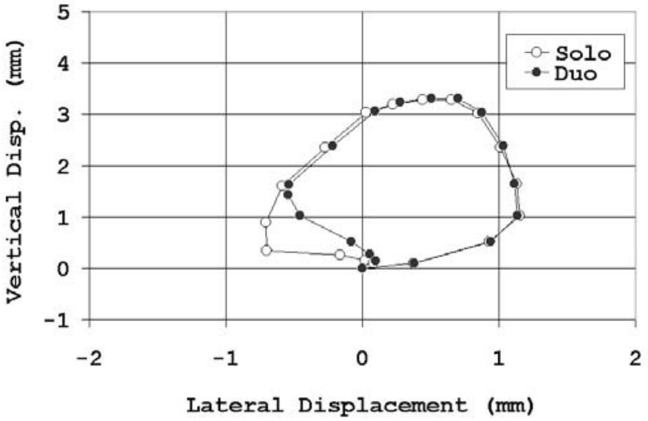

Figure 6.03 Lateral-Vertical Disps. at Stator Flange on June 25: Type I

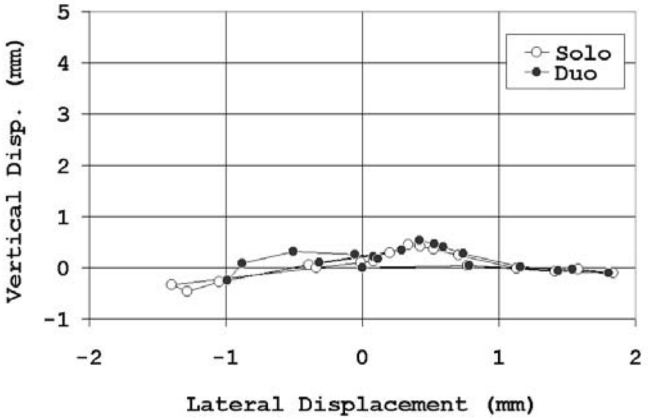

Figure 6.04 Lateral-Vertical Disps. at Stator Flange on June 25: Type IV

The influence of the second guideway is negligible for the guideway in the east-west direction under the summer environment. The lateral and vertical displacements are almost identical as shown in Figure 6.05. This guideway is positioned on the north track within the double track guideway configuration. The change in lateral-vertical displacement on the stator flange is not significant.

In the double track guideway configuration, the effect of shading due to parallel guideways is beneficial because it reduces lateral displacement. Therefore, the single track guideway configuration will control the design of guideways.

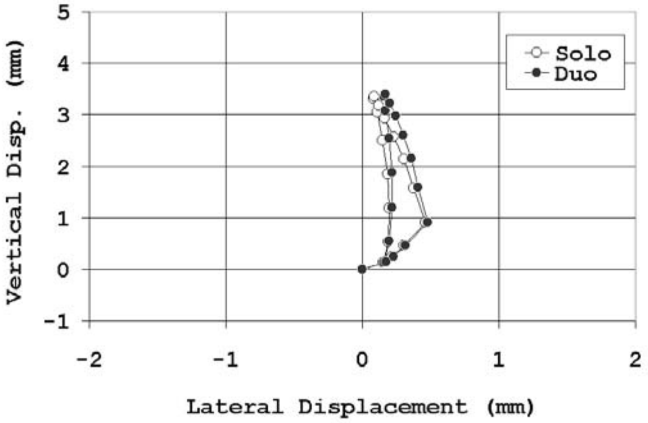

Figure 6.05 Lateral-Vertical Disps. at Stator Flange on June 25: Type I, E-W

## 6.2 Effect of Shading due to Other Structures: Partial Shade

The configuration shown in Figure 6.06 was used to cast a shadow on one span of a two-span guideway. Such conditions have been generally neglected in guideway design. This shaded condition can exist when nearby buildings cast partial shade, when trees cast partial shade, or when other terrain conditions cast a similar shade pattern on the guideways. This configuration is expected to be more severe in terms of displacement criteria than for the double track guideway configuration without partial shading. The guideways that meet the specification criteria may not meet the displacement criteria under such a configuration. For these purposes, a surface that simulated a nearby building in the configuration was located on the east side of the guideway. The surface properties were set to the same properties as the surface of the guideway. The width was the same as the span length of the guideway, and the height was 50 m. Since the slide surface of the guideway is located at 20 m above the ground, the top of the building is about 30 m above the slide surface. The surface is located on the north span of the guideway and is 10 m away from the center of the guideway to the east.

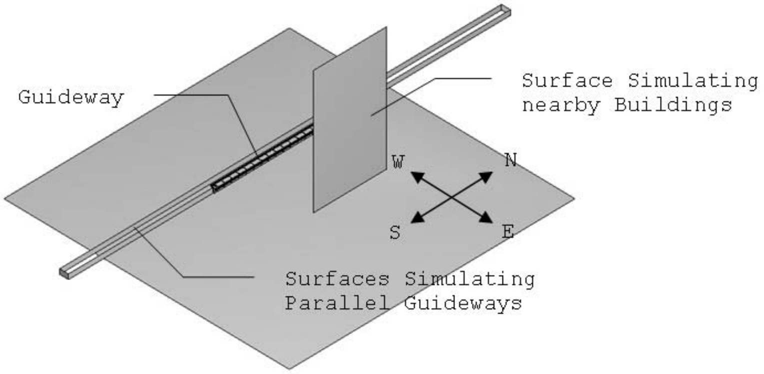

Figure 6.06 Double Track Guideway Configuration under Partial Shading

### 6.2.1 Temperatures of Guideways under Partial Shading

The guideway runs from north to south. In the early morning, the span near the building is under shade. As the sun moves to the west in the afternoon, the guideway is not shaded, and the thermal environment is similar to that on the double track guideway configuration without any other object blocking the solar rays except for some slight reflection from the surface of the building. As shown in Figure 6.07, the north span of the guideway is shaded while the south span experiences solar radiation in the morning.

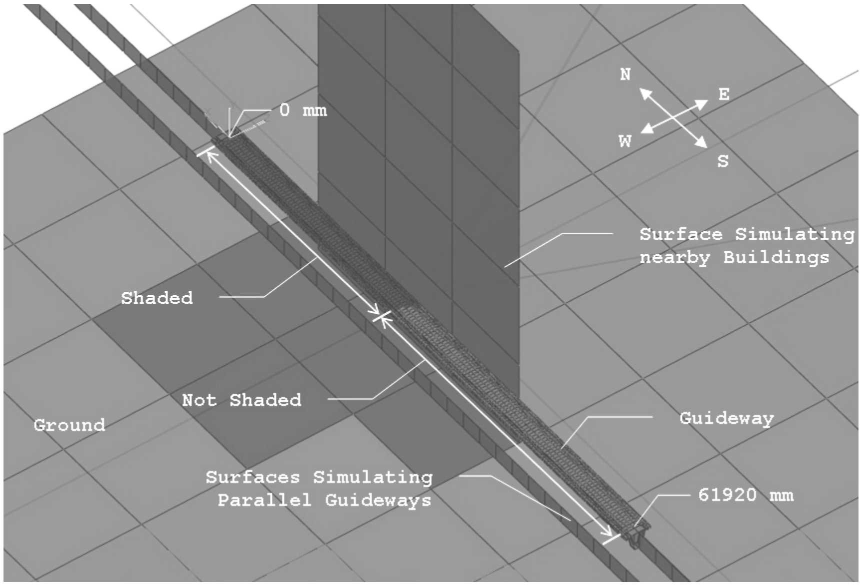

Figure 6.07 Partial Shading at 10:00 on June 25: Type I

In Figure 6.08, the temperature profile at the center of the slide surface along the length of the Type I guideway as the day progresses is shown. The position of 0 mm is at the north end of the guideway. The plot only contains the temperature profile in the morning since the temperature profile in the afternoon is close to the profile of the double track guideway configuration without any other object blocking the solar rays. The slightly higher temperature near 0 mm is due to the solar radiation that was not blocked by the building. The effect of partial shading is revealed by a lower temperature at the north end of the guideway, while the temperature at the south span is high. The temperature at the south span is very similar to that which is present when there is no object that casts shade. The transition between the north end and the south end is shown in the temperature variation in the mid-support of the guideway. The temperature on the bottom flange shown in Figure 6.09 is slightly influenced by partial shade since it is under shade all the time.

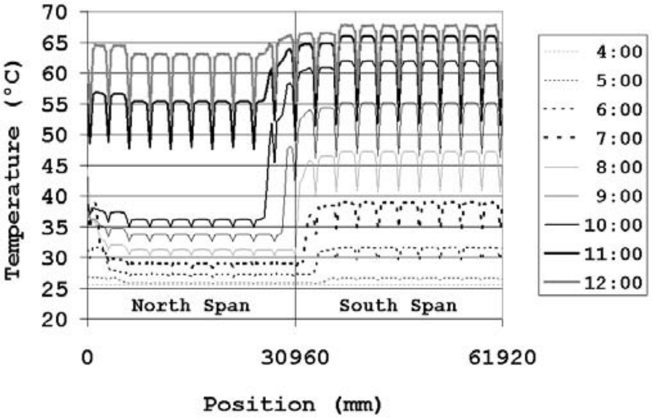

Figure 6.08 Temperature at Slide Surface on June 25: Type I, P/Shade

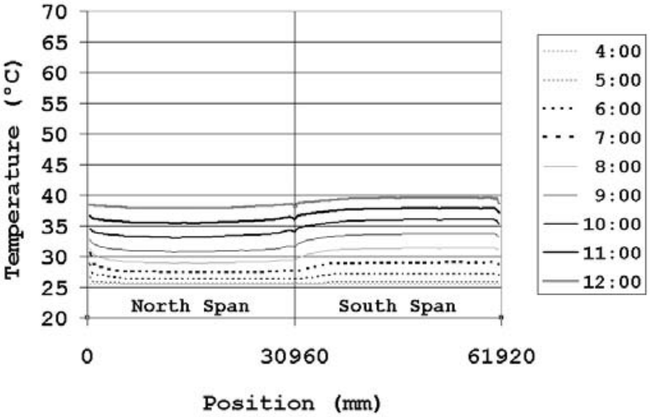

Figure 6.09 Temperature at Bottom Flange on June 25: Type I, P/Shade

The temperature profile on the slide surface of the Type IV guideways in Figure 6.10 shows similar patterns as that of the Type I guideways. Temperatures at the top flange of the support structure along the length shown in Figure 6.11 are relatively uniform compared to the temperature on the slide surface itself. Fluctuations occur at the points where the cross beams are connected. The magnitudes of the peaks are dependent upon the heat flux transferred from the track structure to the support structure. The position where the building structure casts shade is under uniform temperature without any peaks until the slide surface receives solar radiation.

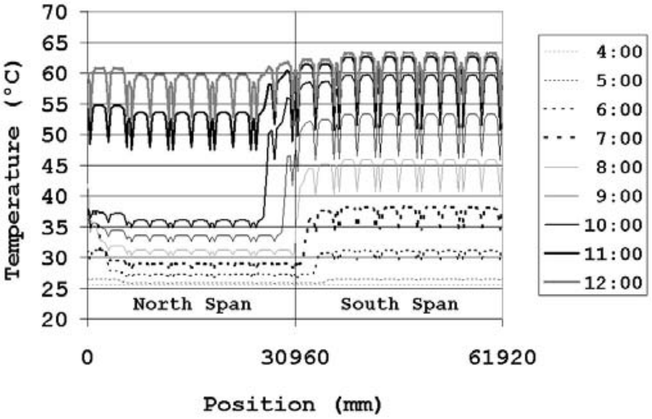

Figure 6.10 Temperature at Slide Surface on June 25: Type IV, P/Shade

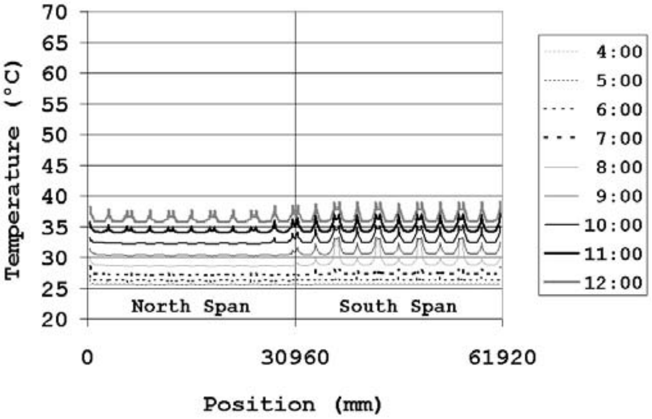

Figure 6.11 Temperature at Top Flange on June 25: Type IV, P/Shade

### 6.2.2 Deformations of Guideways under Partial Shading

The effect of partial shading on the vertical displacement for the Type I guideway in the north-south direction under the configuration shown in Figure 6.07 is plotted in Figure 6.12, in which the original configuration and the deformed configuration at 10:00 on June 25 are displayed. As the south span deflects upward due to the temperature gradient, the north span deflects downward. The north span acts as a restraint on the deformation of the south span and reduces the vertical displacement of the south span. However, if the north span were not shaded, it would deflect upward and impose downward displacement upon the south span. This occurrence would reduce the vertical displacement on the south span to a greater degree as compared to what happens when the north span is shaded. In the case that only one span is under the solar radiation, a more severe condition results. It is possible to violate the displacement criteria specified in the design specifications if one span is shaded, which is also found in Reference 27.

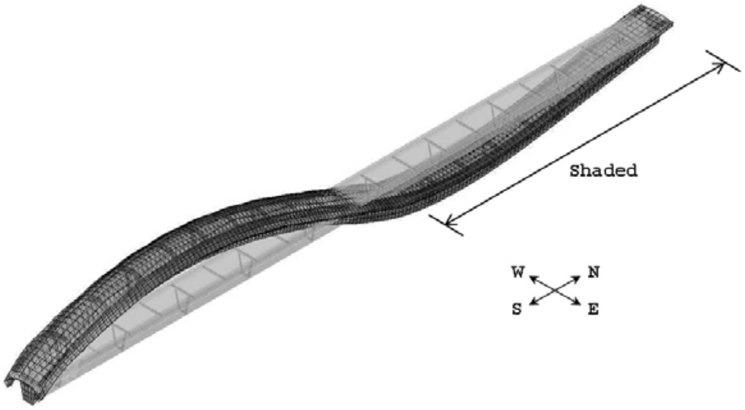

Figure 6.12 Deformation at 10:00 on June 25: Type I, P/Shade

The deformation of the Type IV guideway under partial shading is shown in Figure 6.13 through Figure 6.15. The deformation pattern of Type IV guideways under partial shading is similar to that displayed by Type I guideways except for the fact that the vertical deformation is absorbed by the deformation in the track structure itself. The effect of the partial shading on the lateral displacement, shown in Figure 6.13, would be applicable to the Type I guideway. However, the effect of partial shading on the vertical displacement in the Type IV guideway is not as significant as that in the Type I guideway since the vertical temperature gradient in the support structure is smaller due to the separate track structure.

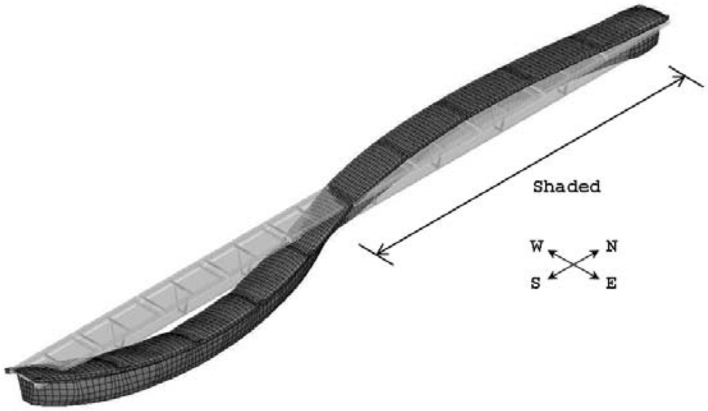

Figure 6.13 Deformation at 06:00 on June 25: Type IV, P/Shade

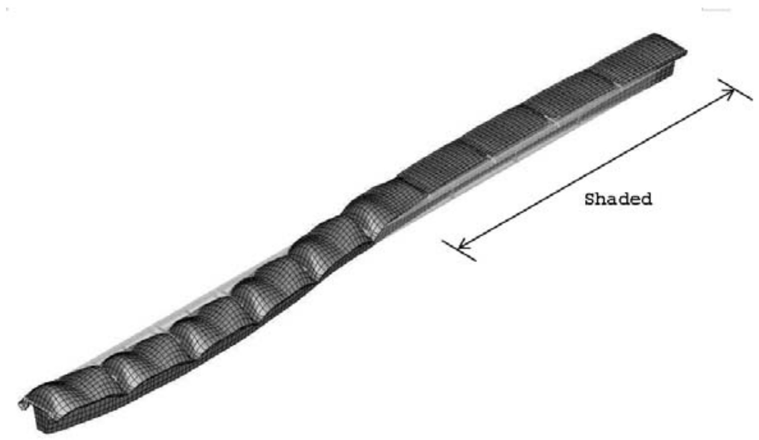

Figure 6.14 Deformation at 10:00 on June 25: Type IV, P/Shade

Figure 6.15 Deformation at 12:00 on June 25: Type IV, P/Shade

The displacements at the stator flange are shown in Figure 6.16 through Figure 6.18. The positions of these displacements are at 10.8 m away from the end along the length for Type I and at 14.2 m away from the end for Type IV. The lateral and vertical displacements under partial shading conditions are more significant, and the prediction of the displacement using the constant temperature gradient is very unconservative. The partial shading effect disappears in the afternoon, and the resulting temperatures in the guideways slowly converge to the temperature profiles of the unshaded guideways. In the afternoon, the guideway receives radiation reflected from the surface of the building. Since nearby buildings are likely to be away from the guideway, the reflected radiation can be considered to be minor unless the building structure has reflective surfaces such as glass. Note that the lateral displacement is close to two times greater, and the vertical displacement is about 1.8 times the displacement of the unshaded guideway.

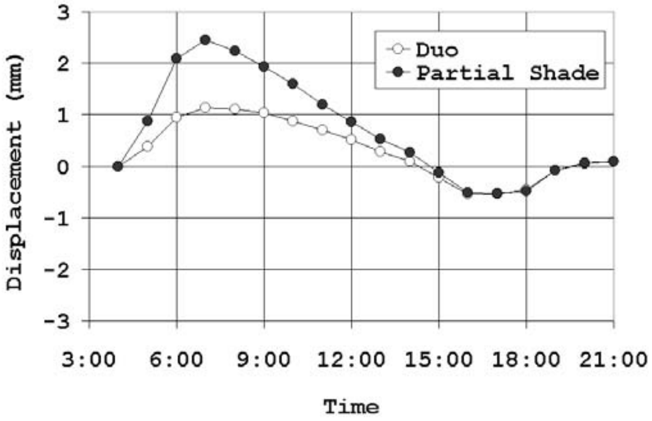

Figure 6.16 Lateral Displacements at Stator Flange: Type I, P/Shade, South Span

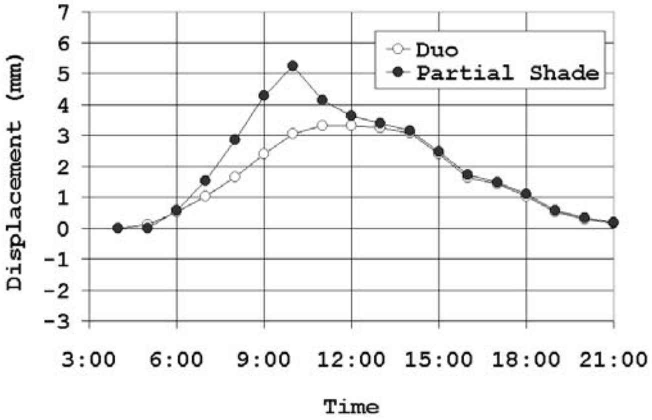

Figure 6.17 Vertical Displacements at Stator Flange: Type I, P/Shade, South Span

As can be seen in Figure 6.18 and Figure 6.19, the lateral and vertical displacements under partial shading conditions can exceed the displacement predicted without considering the partial shading effects, and such displacements may significantly affect the safe operation of the vehicle.

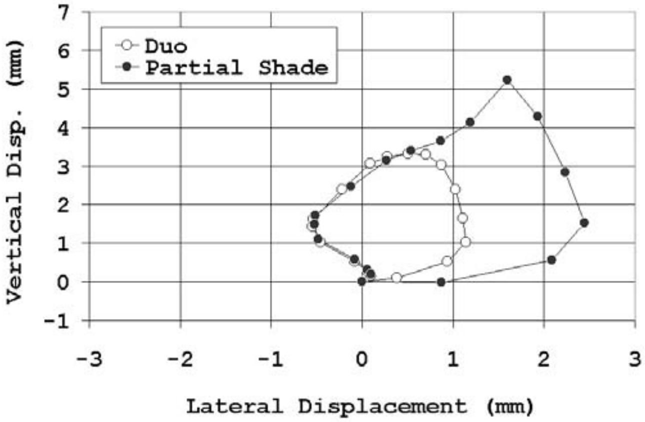

Figure 6.18 Lateral-Vertical Disps. at Stator Flange: Type I, P/Shade, South Span

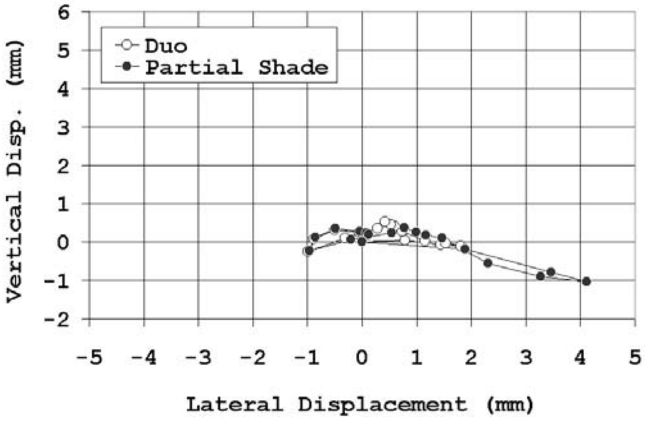

Figure 6.19 Lateral-Vertical Disps. at Stator Flange: Type IV, P/Shade, South Span

The displacements in the north span, shown in Figure 6.20 and Figure 6.21, are generally governed by the compatibility condition imposed by the unshaded south span. In the afternoon, due to the position of the sun, the effect of partial shading diminishes for the guideways running in the north-south direction with the nearby building on the east side. The effect of partial shading would occur in the afternoon if the nearby building was located on the west side of the guideways. The displacement patterns in Figure 6.22 and Figure 6.23 are complex and have generally not been considered in the behavior of guideways or bridges.

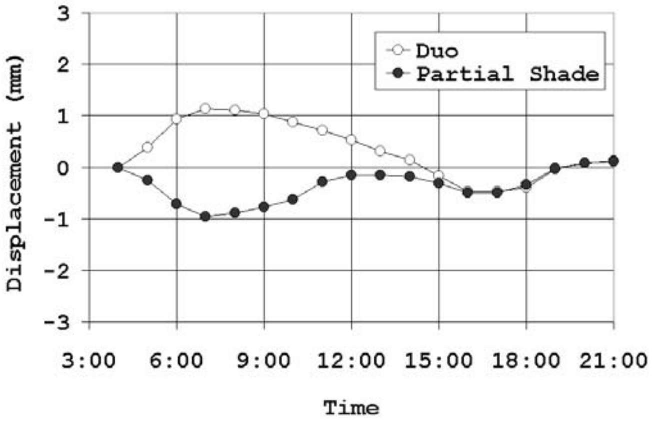

Figure 6.20 Lateral Displacements at Stator Flange: Type I, P/Shade, North Span

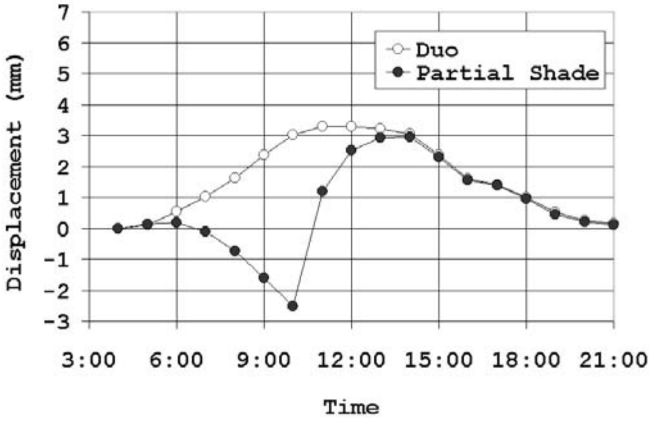

Figure 6.21 Vertical Displacements at Stator Flange: Type I, P/Shade, North Span

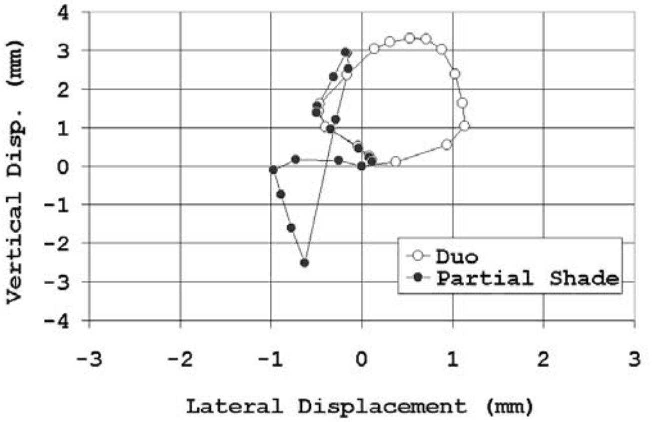

Figure 6.22 Lateral-Vertical Disps. at Stator Flange: Type I, P/Shade, North Span

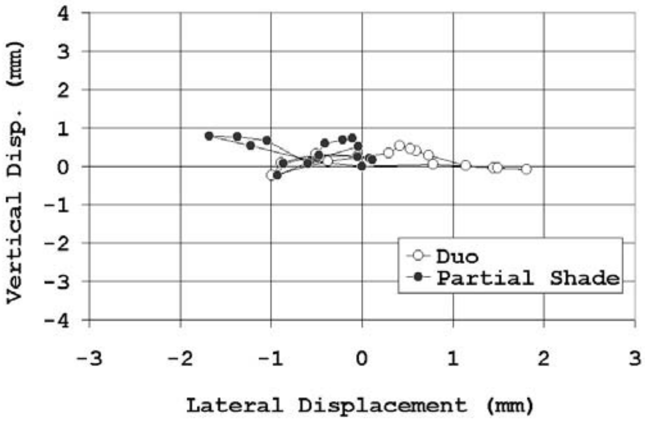

Figure 6.23 Lateral-Vertical Disps. at Stator Flange: Type IV, P/Shade, North Span

Vertical displacement on the stator flange is shown in Figure 6.24. Since the track structure at the north end is shaded, vertical displacements occur on the south end of the guideway. This displacement is also reflected in the rotation that is shown in Figure 6.25. Compared to the cases when no partial shading exists, the maximum rotation has also been increased by 10 percent under the partial shading from 0.00168 to 0.00185 rad for Type I guideways. The effect of partial shading on the vertical displacement of the Type IV guideway is less pronounced. This result is due to the fact that the condition that causes the partial shading does not persist for a long length on each track structure since the length of the track structure is small and the shading pattern changes quickly from the perspective of each track structure.

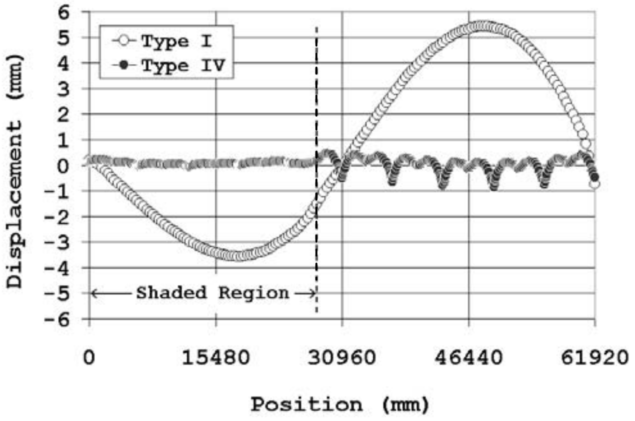

Figure 6.24 Vertical Displacements at Stator Flange at 10:00: Type I & IV, P/Shade

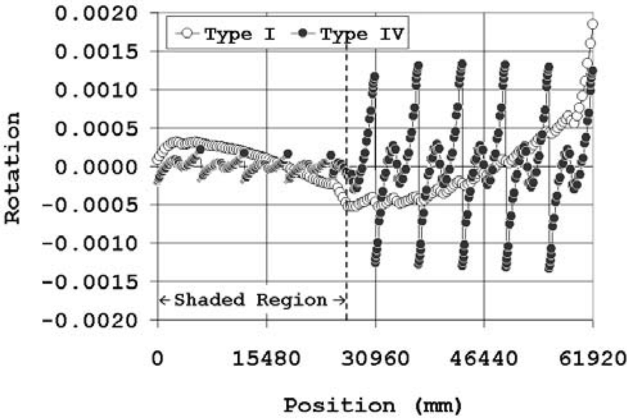

Figure 6.25 Rotations at Stator Flange at 10:00: Type I & IV, P/Shade

The shade pattern itself as well as its duration significantly influences the displacement of the two-span guideways. Since these depend on the proximity and size of nearby structures, it is considered that numerical simulation needs to be performed to determine the shade pattern and its duration that affect the thermal deformation of the guideways

### 6.2.3 Comments on the Effect of Partial Shading

Applying a temperature gradient on a single-span beam or a two-span beam is like applying curvature to a beam. Considering the case when a uniform curvature is applied upon a single girder due to the temperature difference between the top and bottom (case S.1), the vertical displacement is about 3 times that of a two-span beam with the same temperature gradient, and the end rotation is 2 times that of a two-span beam as in case D.1. This effect has been noted previously in Reference 26. Note that in the plots of the displacements, the displacements are normalized with respect to the maximum displacement of the two-span beam under uniform temperature differences (case D.1).

When the two-span beam is under partial shading, the maximum vertical displacement for case D.2 and case D.3 is 1.35 times and more than 2 times than that of the two-span beam in case D.1, and the end rotations are 1.13 times and 1.5 times than that of the two-span beam in case D.1. When the temperature difference exists on 84 percent of the left span (case D.4), the maximum displacement can reach 2.33 times the vertical displacement of the two-span beam in case D.1. For the end rotations, the displacement would be 1.6 times than the end rotation in case D.1. If a transition zone with a length of 0.4L is considered and if the transition is assumed to be linear (case D.5), the displacement and the end rotation are 2.1 and 1.5 times the values given by the beam in case D.1. The effect of partial shading also depends on the duration of its pattern on the guideway. When the shade pattern changes quickly, which happens when the building that cast shadows is located far away from the guideway, the effect of partial shading is not as significant. However, as shown in Figure 6.16 and Figure 6.17, the effect of partial shading can be significant when the building is close to the guideway, and the maximum displacement using conventional specifications would not predict the probable maximum displacements if the guideway was near a building or terrain condition that cast partial shading on the guideways.

| Case | Span and Applied Curvature | Displacement |
|---|---|---|
| S.1 | 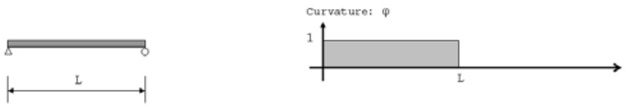 | 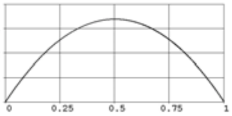 |
| D.1 | 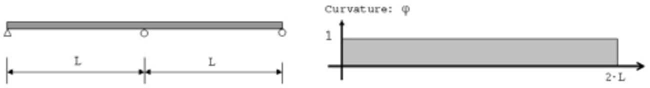 | 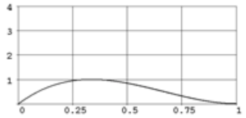 |
| D.2 | 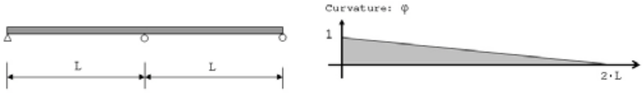 | 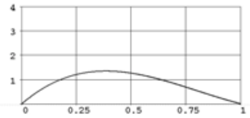 |
| D.3 | 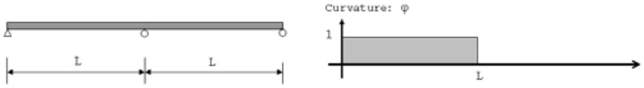 | 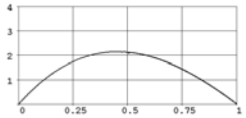 |
| D.4 | 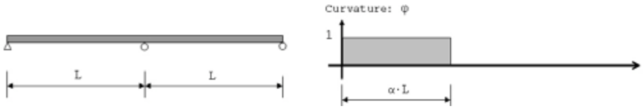 | Max: 2.33<br>(α=0.84) |
| D.5 | 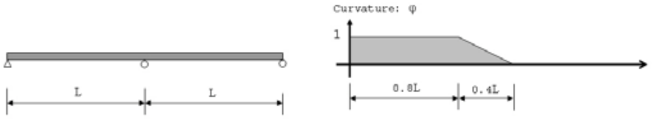 | Max: 2.1 |

Figure 6.26 Normalized Vertical Displacements under Partial Shading

# CHAPTER 7
# CONCLUSIONS

A three-dimensional model of guideways and thermal environments was used to study the behavior of guideways in high-speed transportation. The numerical model of thermal environment was calibrated to the experimental results on a trapezoidal girder under the thermal environment of Austin, Texas. The numerical model effectively describes the temperature distributions of the girder under partial shading conditions imposed by a nearby building.

The behavior of a modular steel guideway under the thermal environment of Las Vegas, Nevada was studied to evaluate the performance of the guideway and to identify the characteristic behaviors of the guideway under various conditions. Using the numerical model, it was discovered that the modular guideway is effective in mitigating vertical displacements and thermal expansion. The vertical displacements in the modular guideway are composed of the displacements due to the deformation of the support structure and the displacements due to the deformation of the track structures. Since the track structures in the guideway effectively cast shade on the support structure, the upward deformation around noon occurs mainly in the track structures and the overall vertical upward displacement is significantly reduced in the modular guideways. The vertical downward displacement, which is not observed in the behavior of Type I guideways, is possible due to the reflected radiation on the bottom flanges of the support structure as well as the downward movement of the stator flanges in the modular guideways. In addition to the role of expansion gaps between track structures, which accommodate the local expansions in the track structures, the longitudinal expansion of the support structure is reduced due to the lower temperature caused by the shade of the track structure on the support structure.

The effect of partial shading can be significant when shade is cast partially on a two-span continuous guideway. However, if the duration of the shade pattern on the guideway is short, it may be somewhat conservative to have one span of the guideway under complete shade while the other span experiences solar radiation. Since the effect of partial shading conditions is dependent on the guideway's geometry and configuration, it is recommended to perform numerical simulation that can determine the duration of the shade pattern on the guideway to determine whether serviceability requirements are satisfied.

# Appendix A
# GIRDER TEMPERATURES

## A.1 Girder Temperatures on November 25, 2004

The temperature of a trapezoidal girder under thermal environment at Austin, Texas is summarized in the following figures. Dotted lines in the figures represent the reference temperature of 25°C.

The temperature is uniform until around 09:00. From 10:00, the variation of the temperature profile becomes visible. The solar radiation starts from the left side and is partially blocked along the length of the girder by a nearby building in the morning. The exterior surface of the left web is facing to the east. The left web heats up quickly due to exposure to solar radiation. Therefore, the temperature of the left side of the web is higher than that of the others. Soon, the direct solar radiation is completely blocked by the building while some of the diffuse radiation is on the girder. Then, the solar radiation is cast again from above. The temperature then increases on the parts such as the top flanges, where the surface normal is facing upward. Before the sun sets, the radiation flux is primary on the interior surface of the left web and the exterior surface of the right web. These surfaces are facing to the west. The temperature on the sides increases to a level greater than the air temperature. The temperature returns to a uniform level as the girder cools down after the sun sets.

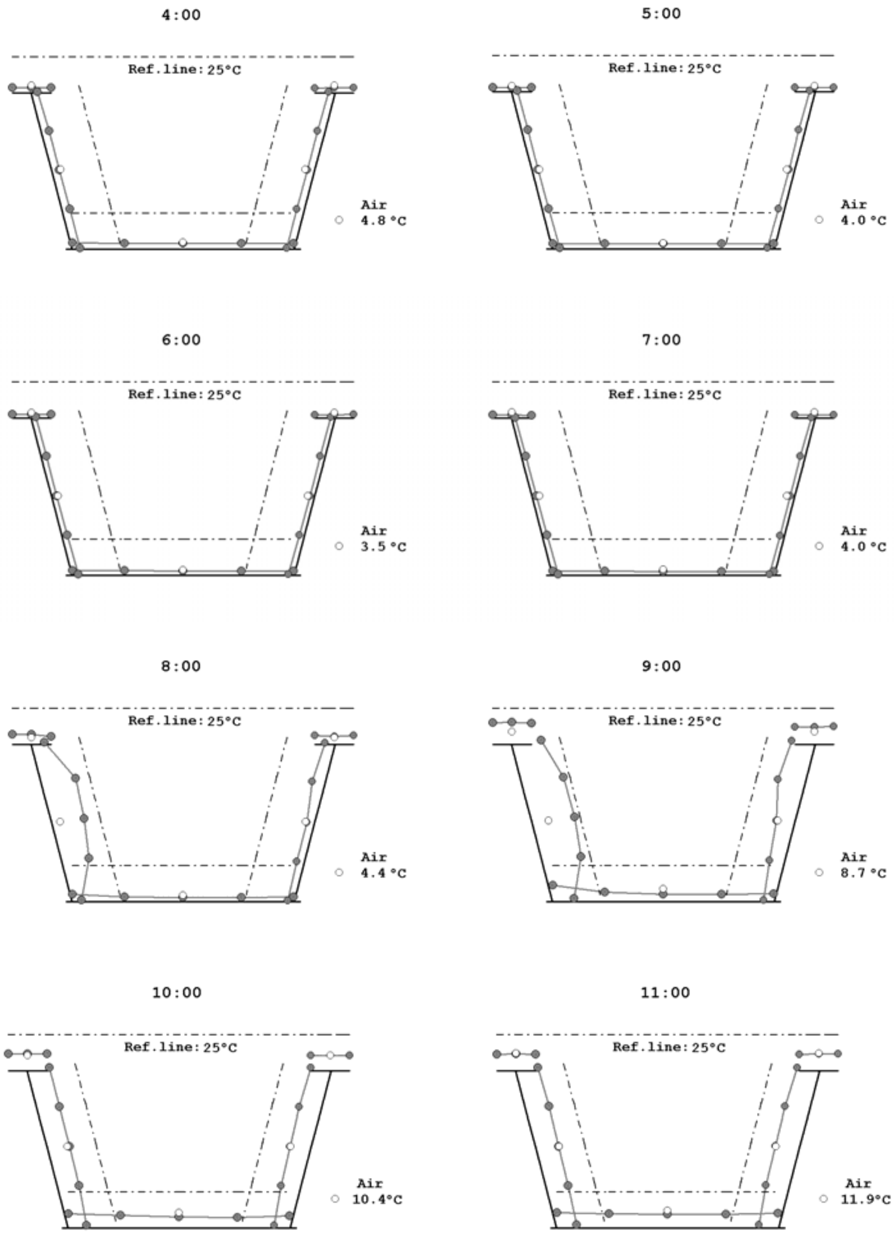

Figure A.01 Temperature Distributions in the Morning on November 25

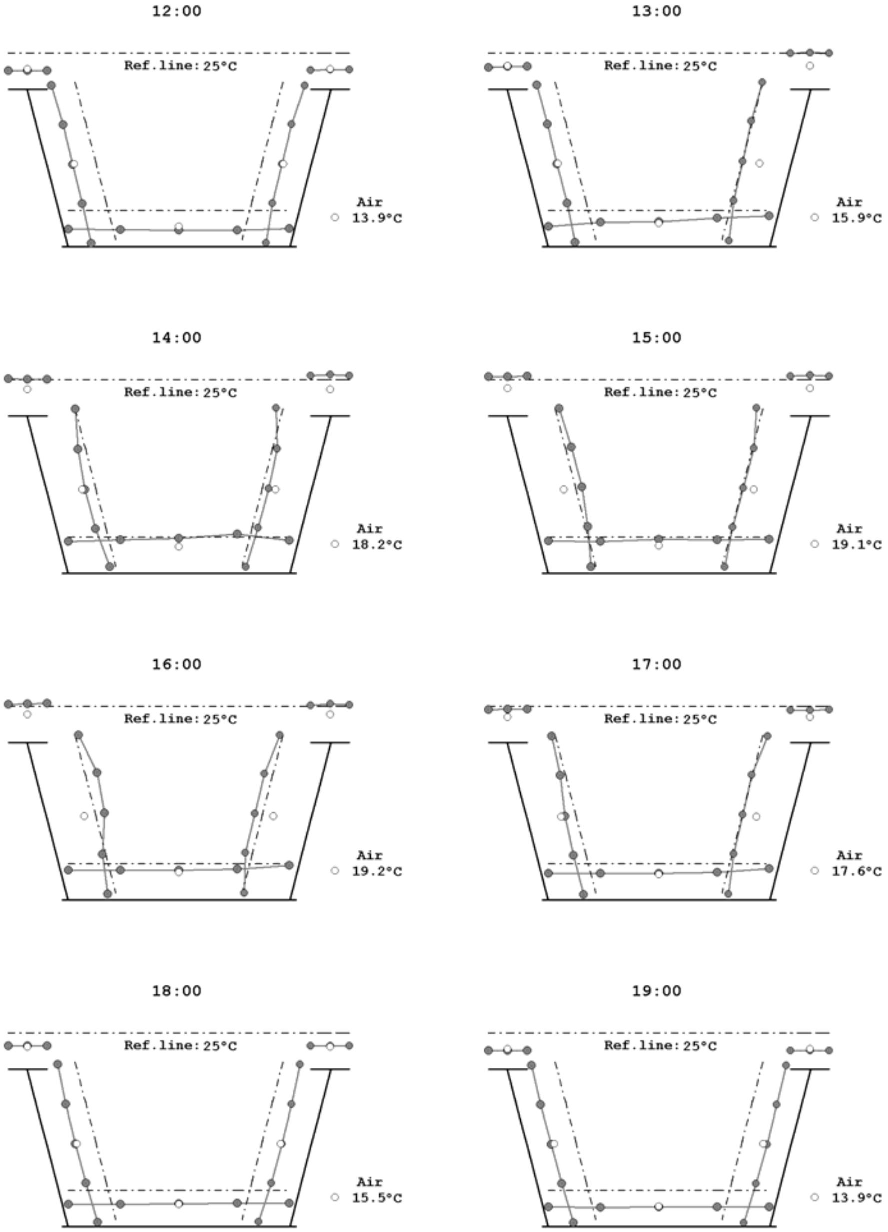

Figure A.02 Temperature Distributions in the Afternoon on November 25

## A.2 Calibration Results on November 25, 2004

The following figures show the calibration results for each measured point on November 25, 2004.

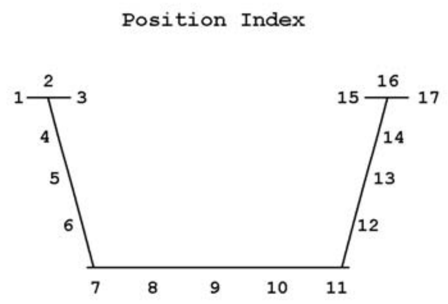

Figure A.03 Position Index

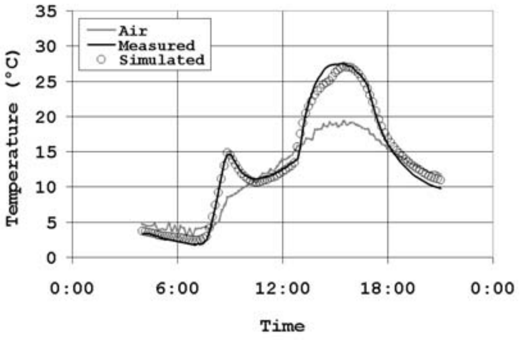

Figure A.06 Temperature at Position 3

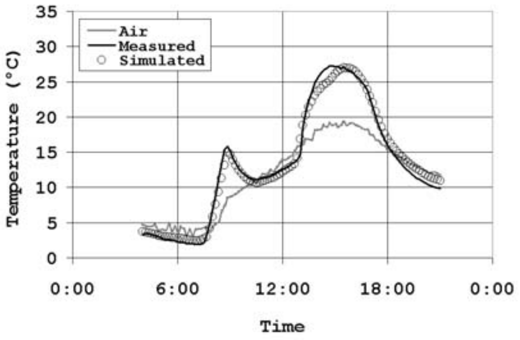

Figure A.04 Temperature at Position 1

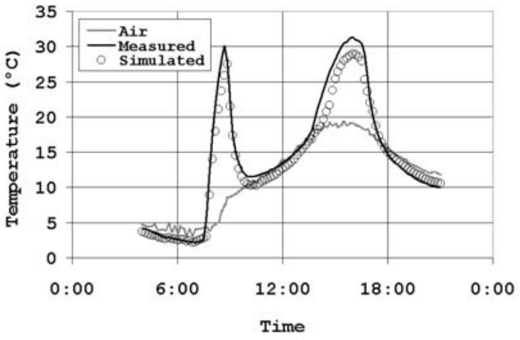

Figure A.07 Temperature at Position 4

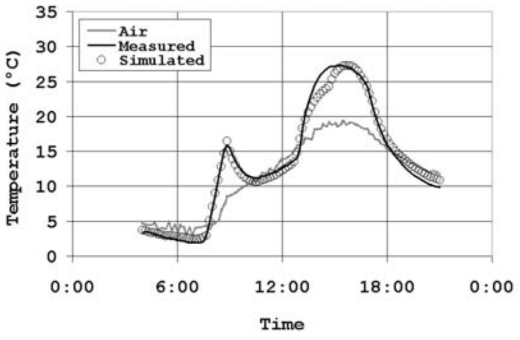

Figure A.05 Temperature at Position 2

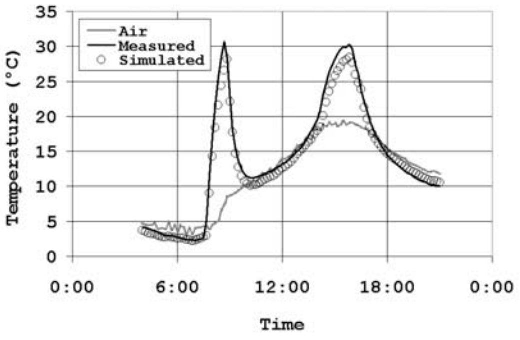

Figure A.08 Temperature at Position 5

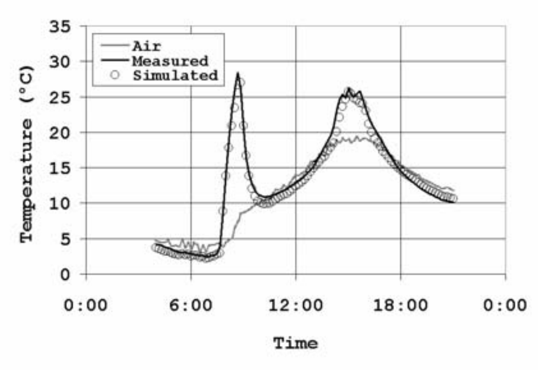

Figure A.09 Temperature at Position 6

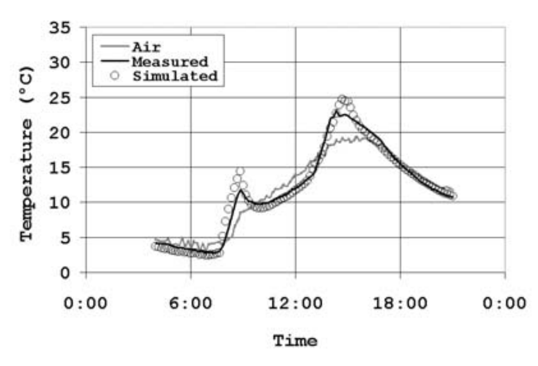

Figure A.10 Temperature at Position 7

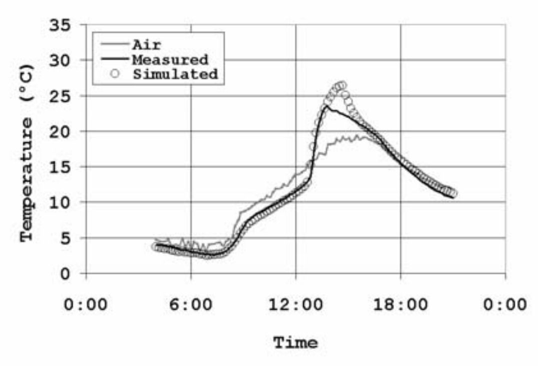

Figure A.11 Temperature at Position 8

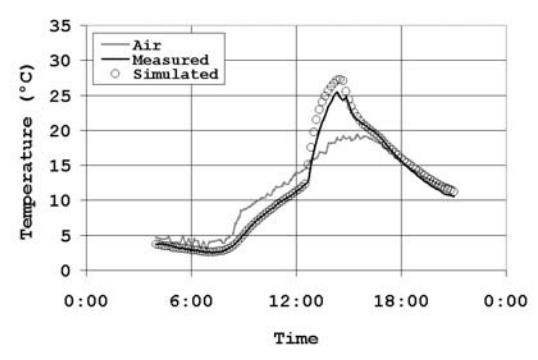

Figure A.12 Temperature at Position 9

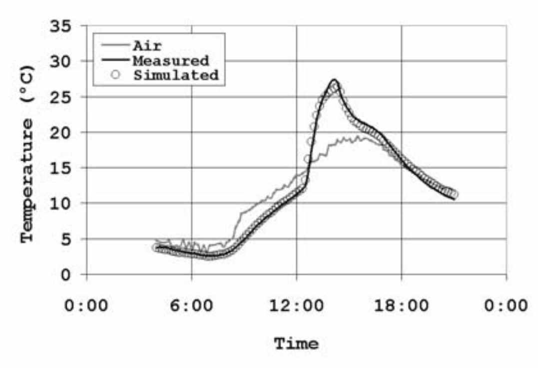

Figure A.13 Temperature at Position 10

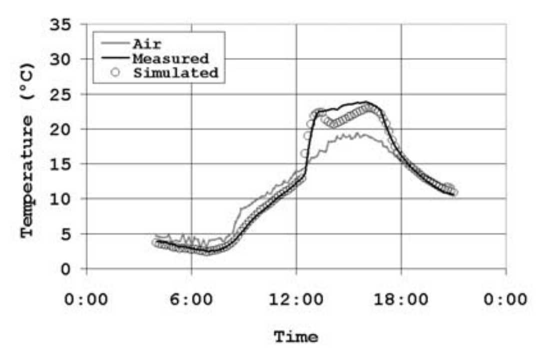

Figure A.14 Temperature at Position 11

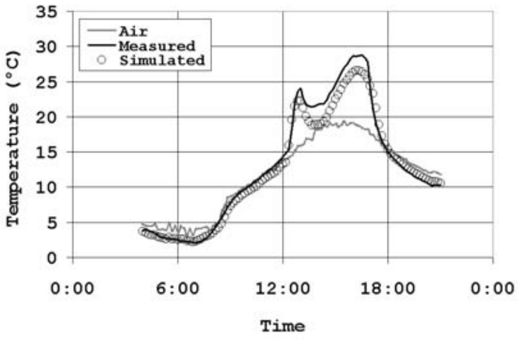

Figure A.15 Temperature at Position 12

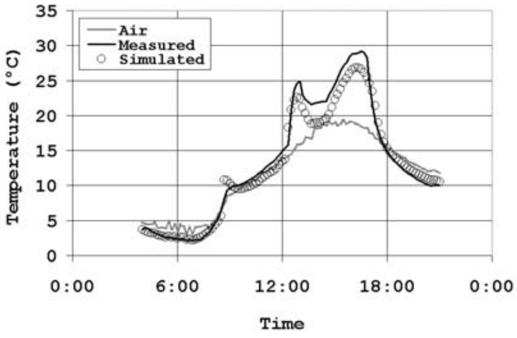

Figure A.16 Temperature at Position 13

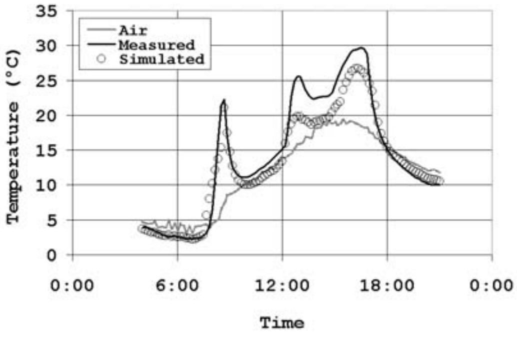

Figure A.17 Temperature at Position 14

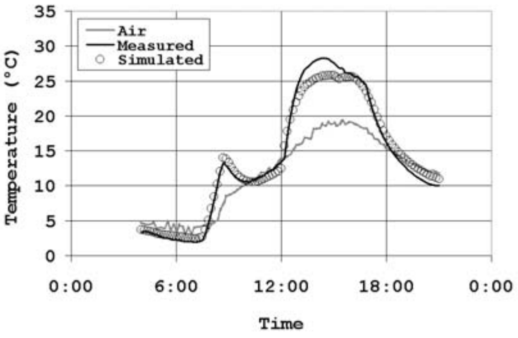

Figure A.18 Temperature at Position 15

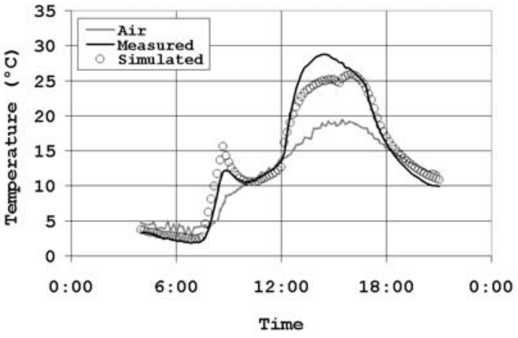

Figure A.19 Temperature at Position 16

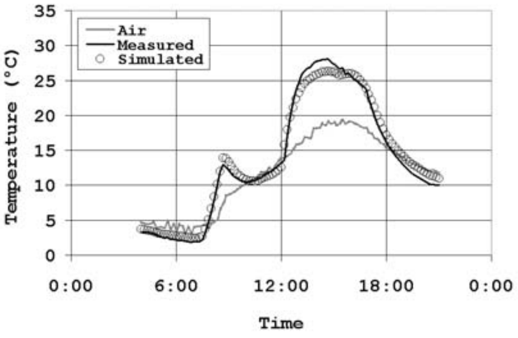

Figure A.20 Temperature at Position 17

# Appendix B
# NUMERICAL ALGORITHM

## B.1 Space Partitioning

To determine the amount of radiation flux on a surface of a structure, the calculation of shading and radiation blocking should be performed. This procedure requires ray-to-object hit testing. If the ray-to-object hit testing is done for each object, it would take a large amount of time. To speed up the calculation, the space that contains a numerical model of a structure is partitioned into small subspaces. There are many algorithms that implement this functionality [34]. The method that is implemented in the numerical model is an adaptation of commonly used algorithms such as the spherical bounding box so that this adaptation could be used with finite element mesh. As shown in Figure B.01, space is initially discretized by a grid, and a sphere with a zero radius is assigned to each grid point. As each element in the mesh information is read into the program, the grid point closest to the element is selected and the radius of the sphere corresponding to the grid point is increased to accommodate the element. Therefore, the relationship between spheres and elements is one-to-many. That is, each element is associated with one sphere, and each sphere contains none-to-many elements. Hit testing is performed using a ray and spheres first, which speeds up the calculation. After selecting the spheres with which the ray intersects, the elements inside the selected spheres are chosen and are sequentially tested one by one to check if the ray intersects with them.

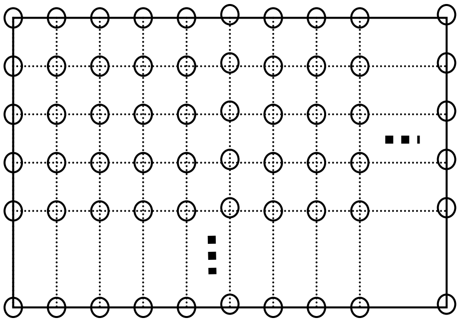

(a) Grid point and Sphere Setup

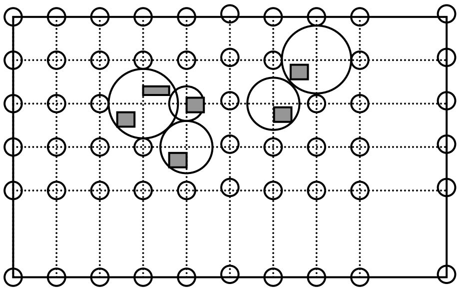

(b) Partitioning

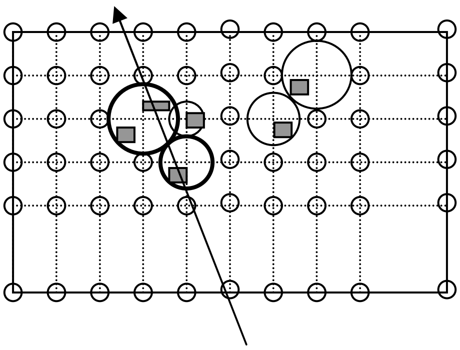

(c) Ray & Sphere Hit Testing

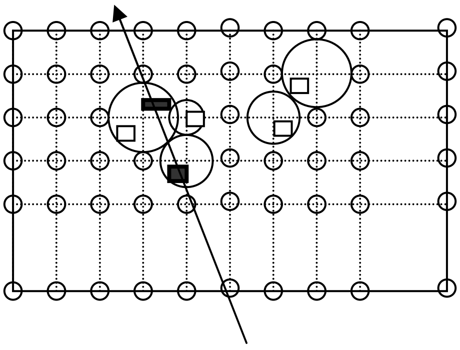

(d) Ray and Object Hit Testing

Figure B.01 Space Partitioning and Hit Testing

# List of References

1. Rhodes, R. G., Magnetic Levitation and Its Future Prospects in Transportation, International Conference on Maglev Transport Now and for the Future, Solihull, England, October, 1984, pp. 1–8
2. Zicha, J. H., Civil Aspects of Maglev Design, International Conference on Maglev and Linear Drives, Vancouver, B.C., Canada, May, 1986, pp. 69–87
3. Stöckl, R., and Schwindt, G., Manufacturing Process and Assembling Line of Guideway and Its Components of the Transrapid Maglev System, International Conference on Maglev and Linear Drives, Las Vegas, May, 1987, pp. 163–169
4. Hartman, J. P., High Speed Ground Transportation: Some Historical Perspectives, Proceedings of the First International Conference on High Speed Ground Transportation Systems, Orlando, Florida, October, 1992, pp. 15–24
5. Gieras, J. F., and Piech, Z. J., Linear Synchronous Motors, CRC Press, Boca Raton, Florida, 2000, pp. 177–209
6. Blomerius, J., Safety of High Speed Maglev Trains of the "Transrapid" Type, Structural Integrity and Passenger Safety, WIT Press, Southampton, UK, 2000, pp. 49–71
7. Heller, A., Maglev on the Development Track for Urban Transportation, Science and Technology Review, Lawrence Livermore National Laboratory, November, 2003, pp. 14–17
8. Priestley, M. J. N., Thermal Gradients in Bridges–Some Design Considerations, New Zealand Engineering, V. 27, No. 7, July, 1972, pp. 228–233
9. Priestley, M. J. N., Design Thermal Gradients for Concrete Bridges, New Zealand Engineering, V. 31, No. 9, September, 1976, pp. 213–219
10. Priestley, M. J. N., Design of Concrete Bridges for Temperature Gradients, ACI Journal, V. 75, No. 5, May, 1978, pp. 209–217
11. Hunt, B., and Cooke, N., Thermal Calculations for Bridge Design, Journal of The Structural Division, ST9, September, 1975, pp. 1763–1781
12. Thepchatri, T., Johnson, C. P., and Matlock, H., Prediction of Temperature and Stresses in Highway Bridges by a Numerical Procedure Using Daily Weather Reports, Research Report 23-1, Center for Highway Research, University of Texas at Austin, February 1977.
13. Will, K. M., Johnson, C. P., and Matlock, H., Analytical and Experimental Investigation of the Thermal Response of Highway Bridges, Research Report 23-2, Center for Highway Research, University of Texas at Austin, Austin, Texas, 1977
14. Yargicoglu, A., and Johnson, C. P., Temperature Induced Stresses in Highway Bridges by Finite Element Analysis and Field Tests, Research Report 23-3F, Center for Highway Research, University of Texas at Austin, Austin, Texas, 1978
15. Potgieter, I. C., Response of Highway Bridges to Nonlinear Temperature Distributions, Ph.D. Dissertation, University of Illinois at Urbana-Champaign, Urbana, Illinois, 1983

16. Imbsen, R. A., Vandershaf, D. E., Schamber, R. A., and Nutt, R. V., Thermal Effects in Concrete Bridge Superstructures, NCHRP Report 276, Transportation Research Board, Washington, D.C., September, 1985

17. Moorty, S., and Roeder, C. W., Temperature Dependent Bridge Movements, Journal of Structural Engineering, V. 118, No. 4, 1992, pp. 1090–1105

18. Roeder, C. W., Proposed Design Method for Thermal Bridge Movements, Journal of Bridge Engineering, V. 8, No. 1, January, 2003, pp. 12–19

19. Elbadry, M. M., and Ghali, A., Temperature Variations in Concrete Bridges, Journal of Structural Engineering, V. 109, N. 10, 1983, pp. 2355–2374

20. Fu, H. C., Ng, S. F., and Cheung, M. S., Thermal Behavior of Composite Bridges, Journal of Structural Engineering, V. 116, No. 12, 1989, pp. 3302–3323

21. Tong, M., Tham, L. G., Au. F. T. K., and Lee, P. K. K., Numerical Modeling for Temperature Distribution in Steel Bridges, Computers & Structures, 79, 2001, pp. 583–593

22. Ho, D., and Liu, C. H., Extreme Thermal Loadings in Highway Bridges, Journal of Structural Engineering, V. 115, No. 7, July, 1989, pp. 1681–1696

23. Tong, M., Tham, L. G., and Au, F. T. K., Extreme Thermal Loading on Steel Bridges in Tropical Region, Journal of Bridge Engineering, V. 7, No. 6, November, 2002, pp. 357–366

24. Campbell, T. I., and Siu, S. W., Thermal Deformations in Typical Maglev Guideway Structures, Journal of Advanced Transportation, V. 21, Winter, 1988, pp. 215–226

25. Samavedam, G., and Purple, A., Thermal Effects and Mitigation Methods for Continuous Sheet Guideways, DOT/FRA/NMI-92/1, January, 1992

26. Kokkins, S. J., Purple, A., and Samavedam, G., Safety of High Speed Magnetic Levitation Transportation Systems, DOT/FRA/ORD-94/10, September, 1994

27. Mangerig, I., Zapfe, C., Lichte, U., and Zapfe, O., Thermal Effects on Guideways for High Speed Magnetic Levitation Transportation Systems, Structures for High-Speed Railway Transportation, IABSE Symposium, Antwerp, Belgium, 2003

28. American Association of State Highway and Transportation Officials, AASHTO LRFD Bridge Design Specifications, 3rd edition, Washington, D.C., 2004

29. Richards, T. B., Weathering Steel for Maglev Guideway Construction: Preliminary Temperature Analysis, M.S. Thesis, The University of Texas at Austin, Austin, Texas, May, 2005

30. Marion, M., and Urban, K., User's Manual for TMY2s, National Renewable Energy Laboratory, June, 1995

31. Lunde, P. J., Solar Thermal Engineering, John Wiley & Sons, New York, 1980

32. Hiller, M. D. E, Beckman, W. A., and Mitchell, J. W., TRNSHD–a Program for Shading and Insolation Calculations, Building and Environment, 35, 2000, pp. 633–644

33. Reda, I., and Andreas, A., Solar Position Algorithm for Solar Radiation Applications, NREL Report No. TP-560-34302, National Renewable Energy Laboratory, June, 2004

34. Foley, J. D., et al., Computer Graphics: Principles & Practice, 2nd edition, Addison-Wesley Publishing Company, 1996

35. Hagen, K. D., Heat Transfer with Applications, Prentice-Hall, New Jersey, 1999

36. Johnson, D., Surface to Surface Radiation in the Program TAU, Taking Account of Multiple Reflection, United Kingdom Atomic Energy Authority Report ND-R-1444(R), 1987

37. ABAQUS Theory Manual, Version 6.4, ABAQUS, Inc., Rhode Island, 2003

38. Transrapid International, Design Loads for Preliminary Girders Type I and Type II in Steel Construction and Guideway Plates Type III in Steel or Concrete Construction, California Nevada Interstate Maglev Project, Technical Report, February, 2000

39. Transrapid International, Transrapid Guideway System: Overview of Styles and Types, Deflection Limits, Tolerances, Offsets, California Nevada Interstate Maglev Project, Technical Description, January, 2002

40. Transrapid International, U. S. M. C. Guideway Development Program: Transrapid Guideway System Document, Transrapid International-USA, August, 2004

# Vita

Hyeong Jun Kim was born in Seoul, Korea on September 15, 1971. He graduated from Jamsil High School in 1990. He studied at Yonsei University where he received a Bachelor of Science degree in Civil Engineering in 1994. During his undergraduate study, he spent his junior year at the University of California at Los Angeles as part of a student exchange program. He studied at the University of Texas at Austin and received a Masters of Science Degree in 1996 with a thesis entitled “Bearing Strength of Bolted Connections.”

Permanent Address: 3-901 Plaza Apt., Gil-dong, Seoul, Korea

This dissertation was typed by the author.